

Harnessing shaped light for enhanced manufacturing using ultrafast
laser inscription

Sam Robert McArthur

Submitted for the degree of Doctor of Philosophy

Heriot-Watt University

School of Engineering and Physical Sciences

September 2023

The copyright in this thesis is owned by the author. Any quotation from the thesis or use of any of the information contained in it must acknowledge this thesis as the source of the quotation or information.

Abstract

The following thesis details the experimental process for the implementation of light beam shaping into the current standard of ultrafast laser fabrication systems, allowing for the development of a monolithic microspectrometer device. The implementation of beam shaping aided in the correction of two limitations in the current writing system: long manufacturing times and depth-related spherical aberration. Firstly, the addition of a pseudo-Bessel beam allowed for a 12-fold reduction in manufacturing timescales, demonstrated by chemical etching dicing of a fused silica sample. Moreover, it was shown that polarisation-insensitive selective etching was achieved by tuning the writing laser's pulse duration. Secondly, it was shown that with the use of a magnitude-scaled Zernike polynomial phase mask, the effects of depth related aberration could be counteracted. These experiments showed that a volume Bragg grating written at a depth of 900 μm produced a low diffraction efficiency, however, this was increased by 36% when the appropriate phase mask was applied. This was supported by an electron plasma imaging study which provided further data without the need for an inscribed object. The knowledge and skills gained during these two projects produced two published papers and the first steps toward the Czerny-Turner base monolithic microspectrometer device.

Acknowledgments

Firstly I'd like to thank the EPSRC and Renishaw for funding this project.

Secondly, I'd like to thank everyone at the Photonic Instrumentation Group who offered advice and support over the four years of the project. It was integral to the project's success. Particular thanks go to Prof. Robert Thomson, my academic supervisor, for technical and academic mentoring. Further, thanks go to Dr. Ross, Dr. MacLachlan, Dr. Benoît, and Mr Siliprandi for their substantial contribution both to the project and the subsequent journal publications.

Special thanks go to Debbie Cannon. Without her feedback on the thesis, it would never have made it to submission.

My warmest gratitude to my family: mum, dad, and my siblings Elliot and Nuala.

Finally, thanks to my partner Leyla. Without whom, I would not have made it through the Ph.D. process.

Inclusion of Published Works Form

Declaration

This thesis contains one or more multi-author published works. I hereby declare that the contributions of each author to these publications is as follows:

| | |
|------------------|--|
| Citation details | S. R. McArthur, R. R. Thomson, and C. A. Ross, "Investigating focus elongation using a spatial light modulator for high-throughput ultrafast-laser-induced selective etching in fused silica," <i>Opt. Express</i> 30 (11), 18903 (2022). |
| S. R. McArthur | Conducted the majority of experimental work. |
| R. R. Thomson | Academic supervisor and contributed experimental advice and edited the final publication. |
| C. A. Ross | Lead researcher, offered advice and guidance to the experiment and took the lead in the writing of the final publication. |

| | |
|------------------|---|
| Citation details | S. R. McArthur, J. Siliprandi, D. G. MacLachlan, A. Benoît, R. R. Thomson, and C. A. Ross, "Ultrafast laser inscription of efficient volume Bragg gratings deep in fused silica using active wavefront shaping," <i>Opt. Mater. Express</i> 12 (9), 3589 (2022). |
| S. R. McArthur | Conducted the majority of experimental work and took the lead on the writing of the publication. |
| J. Siliprandi | Aided in the initial set up of the SLM assisted ULI system. Produced the method of generating Zernike polynomials and offered feedback on the final publication. |
| D. G. MacLachlan | Used his knowledge to assist in the VBG development and characterization. |
| A. Benoît | Helped develop the plasma imaging process. Offered feedback on figures and diagrams in the final publication. |
| R. R. Thomson | Academic supervisor, gave revisions to the final publication. |
| C. A. Ross | Lead researcher assisted in the final version of the publication alongside regular experimental advice. |

Contents

| | |
|---|----|
| List of tables and figures | 8 |
| 1. Introduction | 12 |
| 1.1 Spectroscopy – techniques and applications..... | 12 |
| 1.2 How is spectroscopy from the UV to mid-IR conventionally performed?..... | 14 |
| 1.2.1 Introduction | 14 |
| 1.2.2 Dispersive spectrometer | 14 |
| 1.2.3 Fourier spectrometer | 16 |
| 1.2.4 Homodyne and heterodyne spectrometers | 17 |
| 1.2.5 Fabry-perot interferometer | 18 |
| 1.3 Applications of optical spectroscopy from the UV to the mid-IR | 19 |
| 1.3.1 Biological, medical, and chemical applications..... | 19 |
| 1.3.2 Temporal measurements..... | 20 |
| 1.3.3 Astronomical and spatial applications | 21 |
| 1.3.4 Standoff detection of hazards..... | 22 |
| 1.4 Integrated spectrometers | 22 |
| 1.4.1 What do we mean by an integrated spectrometer? | 22 |
| 1.4.2 Integrated spectrometers – state-of-the-art | 23 |
| 1.5 The Aim and Motivation behind this project..... | 26 |
| 1.5.1 Proposed design..... | 26 |
| 2. In-volume modification of dielectrics using ultrafast laser pulses | 30 |
| 2.1. A history of in-volume modification | 30 |
| 2.1.1. Introduction | 30 |
| 2.1.2. UV base material modification | 30 |
| 2.1.2. Development of high peak power pulsed laser sources..... | 32 |
| 2.1.3. In volume ultrafast laser modification..... | 34 |
| 2.2 The basic experimental setup | 36 |
| 2.3 The physics of ultrafast laser inscription (ULI)..... | 38 |
| 2.3.1 Light-matter interactions | 38 |
| 2.3.2 Key material modifications in silica glass and their manifestations | 39 |
| 2.3.3 The ULI parameters and the roles they play | 40 |
| 2.4 Applications of ultrafast laser inscription (ULI)..... | 44 |
| 2.4.1 Refractive index modification | 44 |
| 2.4.2 Selective chemical etching..... | 48 |
| 3. SLM-enabled focal elongation for reduced manufacturing times..... | 54 |
| 3.1. Introduction to ULI manufacturing times. | 54 |

| | |
|---|-----|
| 3.2 SLM-assisted beam shaping for enhanced ULI | 57 |
| 3.2.1. The experimental approach | 57 |
| 3.2.2. Spatial-light-modulator | 60 |
| 3.2.3. Fourier optics and filtering..... | 63 |
| 3.2.4. Vortex beam-assisted ultrafast laser inscription | 65 |
| 3.3. Author contributions..... | 75 |
| 3.4. Review and future studies | 76 |
| 3.5. Conclusion..... | 76 |
| 4. SLM-assisted aberration compensation during ULI | 78 |
| 4.1. Introduction | 78 |
| 4.1.1. Ultrafast laser microfabrication at depth | 78 |
| 4.1.2. SLM-assisted Zernike polynomial generation | 82 |
| 4.1.3. Preliminary volume Bragg grating studies | 85 |
| 4.1.4. Introduction to free electron plasma imaging..... | 93 |
| 4.2. Author contributions..... | 99 |
| 4.3. Review and further study..... | 100 |
| 4.4. Conclusion..... | 101 |
| 5. Prototype integrated spectrometer device | 102 |
| 5.1. Development of a microspectrometer device via beam shaping-assisted ultrafast laser inscription | 102 |
| 5.1.1. Review of current capabilities..... | 102 |
| 5.1.2. Review of the current idea from the spectrometer device | 102 |
| 5.1.3. Revisions to the spectrometer device | 105 |
| 5.1.4. Device inscription and etching..... | 106 |
| 5.1.5. Device testing..... | 107 |
| 5.2. Discussion..... | 109 |
| 5.2.1. Further development | 109 |
| 6. Conclusion..... | 112 |
| 6.1. Vortex beam elongation | 112 |
| 6.2. Aberration compensation | 113 |
| 6.3. Prototype spectrometer | 115 |
| 6.4. Looking forward | 116 |
| 7. References | 117 |
| 8. Appendix | 120 |
| 8.1. "Investigating focus elongation using a spatial light modulator for high-throughput ultrafast-laser-induced selective etching in fused silica" | 121 |

8.2. "Ultrafast laser inscription of efficient volume Bragg grating deep in fused silica using active wavefront shaping" 134

8.3. Internal Examiners declaration form 142

List of tables and figures

| | |
|--|----|
| Fig. 1. A DIAGRAM ILLUSTRATING AN ABSORPTION AND EMISSION PROCESS FOR A SINGLE HYDROGEN ATOM, WITH AN EXAMPLE OF THE PRODUCED SPECTRUM. DETAIL THE ABSORPTION OF 410 NM, 434 NM, 486 NM, AND 656 NM FOR THE FORMER CASE A), AND EMISSION THE SAME WAVELENGTH OF THE EMISSION CASE B). | 14 |
| Fig. 2. A SCHEMATIC DIAGRAM OF THE BASIC SODIUM SPECTRUM EXPERIMENT. DEPICTING: THE SODIUM LAMP, COLLIMATOR, PRISM, ROTATING TABLE, AND EYE PIECE. THE LIGHT PATH IS SHOW PASSING THROUGH THE PRISM AND FORMING THE SODIUM D-LINE. | 15 |
| Fig. 3. A SCHEMATIC OF A BROADBAND LIGHT SOURCE INCIDENT WITH A BINARY DIFFRACTION GRATING. THE DIFFRACTED LIGHT IS SEPARATED OUT BOTH IN WAVELENGTH AND DIFFRACTION ORDER, WITH THE POWER IN EACH ORDER DECREASING FROM THE ZEROth ORDER. | 16 |
| Fig. 4. A SCHEMATIC OF A BASIC INTERFEROMETER SET UP. DEPICTING: A LASER SOURCE, A STATIC MIRROR, AND OSCILLATING MIRROR, A BEAM SPLITTER, AND DETECTOR. | 17 |
| Fig. 5. A SCHEMATIC OF A FABRY-PEROT CAVITY. DETAILING THE INCIDENT LIGHT, THE TWO PARTIALLY TRANSPARENT SURFACE, THE BEAM OSCILLATION WITHIN IT, AND THE TRANSMITTED LIGHT FORMING THE $M + 1$ FRINGE ORDER. THIS ORDER IS ALSO DEPICTED ALONGSIDE THE M ORDER, FORMING A SET OF CONCENTRIC RINGS. | 18 |
| Fig. 6. A MICRORING ARRAY CAPTURED BY AN ELECTRON MICROSCOPE [28]. | 24 |
| Fig. 7. A CAD REPRESENTATION OF AN ECHELLE GRATING BASED COMPACT SPECTROMETER DEVICE [30]. PRIMARY COMPONENTS ARE DETAILED ALONG WITH THE BEAM PATH WHERE 7 IS THE ECHELLE GRATING AND 10 IS THE DETECTOR. | 24 |
| Fig. 8. A BASIC MACH-ZAHNDER INTERFEROMETERS. DETAILED IN THE LASER SOURCE, THE TWO BEAM SPLITTER, MIRRORS AND DETECTORS, ALONG WITH POSITION OF THE SAMPLE BEING STUDIED. | 25 |
| Fig. 9. A SCHEMATIC OF A AWG DEVICE TAKEN FROM A PUBLICATION [32]. SHOWN IS THE ARRAY OF WAVEGUIDES ITSELF, AS WELL AS THE INPUT AND OUTPUT COUPLERS. CONTAINED ALSO AS CLOSE UP IMAGES OF THESE FEATURES. | 26 |
| Fig. 10. THE BASIC LAYOUT OF CZERNY-TURNER SPECTROMETER. KEY COMPONENTS ARE DEPICT INCLUDING: A LIGHT SOURCE, THE COLLIMATING MIRROR, A DIFFRACTION GRATING, THE FOCUSING MIRROR, AND A SENSOR ARRAY. | 27 |
| Fig. 11. A) RAY DIAGRAM OF THE PROPOSED MONOLITHIC CZERNY-TURNER SPECTROMETER PRODUCED IN ZEMAX BY DR. CALUM ROSS. DETAILED FOLLOWING THE SOURCE IS THE COLLIMATING CURVED MIRROR M1, THE GRATING PLANE, THE FOCUSING CURVED MIRROR, AND FINALLY THE IMAGE PLANE. B) SCHEMATIC DIAGRAM OF THE PROPOSED MONOLITHIC SPECTROMETER WITH A MORE DETAILED DESCRIPTION OF THE INDIVIDUAL COMPONENTS. THIS INCLUDED A FIBRE SLOT FOR COUPLING OF SOURCE LIGHT, A VOLUME BRAGG GRATING (VBG) IN THE GRATING PLANE, AND A SENSOR IN THE IMAGE PLANE. | 28 |
| Fig. 12. A SCHEMATIC DIAGRAM OF THE ARGON LASER TESTING SETUP, USED TO MEASURE THE EFFECTIVENESS OF THE REFLECTOR. DETAILING PRIMARY COMPONENTS, TAKEN WITH PERMISSION FROM THE PUBLICATION BY K. O. HILL ET. AL [37]. | 31 |
| Fig. 13. A SCHEMATIC DIAGRAM OF THE PHASE MASK WRITING SYSTEMS, DETAILING THE INCIDENT UV LIGHT, THE GRATING, AND THE DIFFRACTED ORDER. SHOWN ALSO IS THE OPTICAL FIBRE AND THE FRIDGES THAT INTERACT TO FORM THE MATERIAL MODIFICATION[38]. | 32 |
| Fig. 14. A SCHEMATIC DIAGRAM OF THE CYLINDRICAL LENS AND PHASE MASK BASE WRITING SYSTEM USING AN ULTRAFAST LASER SOURCE. THE PRIMARY OPTICAL COMPONENTS HAVE BEEN DETAILED, AND THE POSITION OF MODIFICATION HIGHLIGHTED IN YELLOW. | 34 |
| Fig. 15. A SCHEMATIC DIAGRAM OF THE OBJECTIVE BASED WRITING SYSTEM, DETAILING THE WRITING OBJECTIVE, THE TRANSLATION DIRECTION, AND THE POINT OF MATERIAL MODIFICATION (HIGHLIGHTED IN YELLOW). | 35 |
| Fig. 16. A SCHEMATIC DIAGRAM OF THE CURRENT STANDARD OF ULTRAFAST LASER MICROFABRICATION SYSTEM. THE ULTRAFAST LASER SYSTEM DEPICTED WAS THE LIGHT CONVERSIONS PHAROS. THIS IS FOLLOWED BY POWER CONTROL PROVIDED BY A POLARISING BEAM SPLITTER (PBS) AND A HALF-WAVEPLATE (HWP). FOLLOWING THIS IS POLARIZATION CONTROL PROVIDED BY ANOTHER HWP AND A QUARTER-WAVEPLATE (QWP). FINALLY THERE IS THE FINAL WRITING OBJECTIVE. THE OBJECTIVE LEADS TO A SAMPLE MOUNTED ONTO A 3-AXIS MOTION CONTROL TRANSLATION STAGE. C1 IS A CAMERA ARRANGED SUCH THAT IT CAPTURES LIGHT REFLECTED OFF THE SAMPLE, ALLOWING FOR IT TO BE POSITION APPROPRIATELY. | 37 |
| Fig. 17. DETAILED HERE ARE THE INDIVIDUAL MECHANISM WHICH MAKE UP THE NONLINEAR ABSORPTION PROCESS SEPARATED INTO CARRIER EXCITATION, THERMALISATION, AND THERMAL AND STRUCTURAL EVENTS. THEY ARE DISPLAYED WITH THEIR APPROXIMATE TIMESCALE PLOTTED IN SECONDS WITH THE APPROXIMATE STARTING AND END TIMES OF EACH SUB-PROCESS [45]. | 38 |
| Fig. 18. A PLOT OF PULSE ENERGY VS PULSE DURATION DETAILING THE TRANSITION ZONES BETWEEN DIFFERENT MODIFICATION REGIMES, REGIME 1, 2, AND 3. RESULTS WERE OBTAINED WITH A FUSED SILICA SAMPLE [47]. | 42 |
| Fig. 19. A SKETCH OF THE THREE STANDARDISED WAVEGUIDE TYPES. TYPE I: PURE MODIFICATION, TYPE II: TWO PARALLEL LINES OF DAMAGED MATERIAL WITH THE GUIDING CAVITY IN THE CENTRE, TYPE III: AN ARRAY OF DAMAGED MATERIAL FORMING THE LIGHT GUIDING CAVITY. | 45 |
| Fig. 20. 1: DICING OF A SUBSTRATE USING CHEMICAL ETCHING ASSISTED ULTRAFAST LASER INSCRIPTION. DETAILING STEPS – A) THE INITIAL MODIFIED REGIONS, B) THE MODIFIED REGION BEING REMOVED VIA THE CHEMICAL ETCHANT, AND C) THE FINAL OUTCOME WITH THE SAMPLE DICED INTO SEPARATED SECTION. 2: THE REMOVAL OF MATERIAL FROM A SAMPLE PRODUCING A HOLLOW CHANNEL. DETAILING STEPS – A) THE INITIAL MODIFIED REGIONS, B) THE MODIFIED REGION BEING REMOVED VIA THE CHEMICAL ETCHANT, AND C) THE FINAL OUTCOME WITH A HOLLOW CHANNEL ETCHED INTO THE SUBSTRATE AND THE CYLINDER OF REMOVED MATERIAL. | 48 |
| Fig. 21. PLOT OF THE TEMPERATURE CHANGE IN DEGREES CELSIUS OVER THE COURSE OF 20 HOUR FOR TWO SENSORS IN THE ULI LABORATORY. | 52 |
| Fig. 22. CAD IMAGE OF THE ULI WRITING STAGES PRODUCED IN AUTODESK INVENTOR. | 56 |
| Fig. 23. A SCHEMATIC DIAGRAM OF THE BEAM SHAPING ASSISTED ULTRAFAST LASER INSCRIPTION SETUP. THE NEW ADDITIONS TO THE STANDARD SETUP ARE HIGHLIGHTED IN THE GREEN BOXES, INCLUDING THE BEAM EXPANDER, THE SLM, AND THE 4F SPATIAL FILTERING SYSTEM. NOTED IN THE SPATIAL FILTER SYSTEM ARE THE TWO FOURIER TRANSFORM LENSES Ft1 AND Ft2, THE IRIS USED TO REMOVE UNNEEDED ORDERS, AND THE POSITION 1ST | |

| | |
|---|----|
| DIFFRACTION ORDER. THE GREY DASHED BOXES SEPARATE SECTIONS OF THE SYSTEM WHICH ARE IN DIFFERENT SPATIAL PLANES, THESE ARE THE XY PLANE FOR THE FIRST SECTION AND YZ PLANE FOR THE SECOND. | 58 |
| Fig. 24. A PHOTOGRAPH OF THE WRITING STAGES DETAILING - A) THE GRANITE BASE AND ARCH, B) THE BREADBOARD, C) AIR BEARING TRANSLATION STAGES, AND D) THE SAMPLE MOUNT. | 59 |
| Fig. 25. A PHOTOGRAPH OF THE HAMAMASTU SPATIAL LIGHT MODULATOR, MOUNTED AND POSITIONED WITHIN THE FINAL BEAM SHAPING ASSISTED ULI SYSTEM. | 61 |
| Fig. 26. A SCHEMATIC CROSS-SECTION OF THE ACTIVE AREA OF A LCOS (LIQUID CRYSTAL ON SILICON) SLM OPERATION IN THE REFLECTION MODE. DETAILS INCLUDED ARE THE GLASS SURFACE, FOLLOWED BY A TRANSPARENT ELECTRODE LAYER WHICH IN TANDEM WITH THE PIXELISED ELECTRODE LAYER CONTROLS THE ORIENTATION OF THE LIQUID CRYSTAL LAYER. FINALLY INCLUDED IS THE ALUMINIUM MIRROR. | 61 |
| Fig. 27. A SET OF PHASE MASKS USED TO PRODUCE GAUSSIAN BEAM LASER WRITING WITH AN SLM WHERE: A) IS THE CORRECTION MASK PACKAGED WITH THE SLM AND CALIBRATED FOR 1030 NM, B) IS A BLAZED DIFFRACTION GRATING WITH 16 PIXEL PER LINE FOR A DENSITY OF 6.25 LINES PER MILLIMETRE (L/MM), AND C) IS THE FINAL PHASE MASK OF BOTH A) AND B) CONTRIBUTION COMBINED. | 62 |
| Fig. 28. PAIR OF DIAGRAMS ILLUSTRATING THE FOURIER SPATIAL FILTERING SYSTEM. A) DEPICTS THE SYSTEM, WHERE LIGHT FROM THE OBJECT PLANE IS FOURIER TRANSFORMED IN THE FOURIER PLANE BY THE FOURIER TRANSFORM LENS F_1 . THE IMAGE FORMED IN THIS PLANE IS A SERIES OF DISTINCT ORDERS. THE SECOND FOURIER TRANSFORM LENS F_2 DOES ANOTHER TRANSFORM RESULTING IN A FIELD PRESENT IN THE IMAGE PLANE. B) IS THE SAME SYSTEM BUT WITH A SPATIAL FILTER, DEMONSTRATING THE EFFECT THIS WOULD HAVE ON THE RESULTS PRESENT ON THE IMAGE PLANE. THE ORDERS OF LIGHT ARE SEPARATED OUT INTO THREE COLOURS: YELLOW -1ST, ORANGE 0TH, AND RED +1ST. | 64 |
| Fig. 29. A DIGITAL PHASE MASK CONTAINING: THE BLAZED GRATING, THE FLATNESS CORRECTION MASK PACKAGED WITH THE SLM, AND THE PUPIL CROP. | 65 |
| Fig. 30. A DIAGRAM OF THE BASIC OPERATION OF THE AXICON LENS. DETAILING: THE WAVEFRONT DIAMETER D , THE AXICON GRADIENT A , AND THE POSITION OF THE PSEUDO-BESSEL BEAM. | 66 |
| Fig. 31. (A) A PHASE MASK OF A DIGITAL AXICON WITH A PHASE GRADIENT OF 4.27 MRAD. (B) IS THE FINAL VORTEX BEAM PHASE MASK CONTAINING THE BLAZED GRATING, PUPIL CROP, AND FLATNESS CORRECTION. | 67 |
| Fig. 32. A ZEMAX SIMULATION OF THE OPTICAL SYSTEM SPANNING FROM THE SLM WHILE DISPLAYING THE DIGITAL AXICON TO THE IMAGE PLANE OF THE SECOND FOURIER TRANSFORM LENS. HIGHLIGHTED IS THE WAVEFRONT IMMEDIATELY AFTER THE SLM, SHOWING THE GENERATION OF A GAUSSIAN-BESSEL BEAM. NEXT, THE FOURIER PLANE IS HIGHLIGHTED WHICH SHOWS THE RING-SHAPED FOCUS FORMED 1F AWAY FROM THE FIRST FOURIER TRANSFORM LENS (F_1). FINALLY, THE VORTEX BEAMS FOCUS IS HIGHLIGHTED, FORMED IN THE IMAGE PLANE 1F AWAY FROM THE SECOND FOURIER TRANSFORM LENS (F_2). | 68 |
| Fig. 33. A SERIES OF PHOTOGRAPHS OF THE FOCAL VOLUME ALONG THE OPTICAL AXIS. WHAT IS SHOWN IS THAT AS THE RING WAVEFRONT IS FOCUSED THE FINAL AXIAL VOLUME IS MAINTAINED OVER A DISTANCE OF 200 μ M. THE DISTANCE BETWEEN EACH IMAGE IS 20 μ M, WITH THE IMAGE PLANE MOVING TOWARDS THE WRITING OBJECTIVE. | 69 |
| Fig. 34. (A) AND (B) ARE MICROGRAPHS OF PARTIAL FREE-ELECTRON PLASMA EMISSION FROM THE FOCAL REGION INSIDE FUSED SILICA UNDER IRRADIATION WITH A GAUSSIAN AND VORTEX FOCUS (GENERATED BY IMPARTING A 3.20 MRAD CONICAL PHASE FRONT) RESPECTIVELY. (C) IS A SERIES OF MICROGRAPHS SHOWING ETCHED CHANNEL FACETS WRITTEN WITH A RANGE OF PULSE ENERGIES AND CONICAL PHASE MASKS TO HIGHLIGHT THE DOF ELONGATION. THE REPETITION RATE WAS 50 KHZ, POLARISATION WAS CIRCULAR, TRANSLATION SPEED WAS 4 MM/S AND THE PULSE DURATION WAS 1440 FS WHEN WRITING THE CHANNELS SHOWN. INSET: A CORRESPONDING CHANNEL CROSS-SECTION PRIOR TO ETCHING (AT SAME SCALE)..... | 70 |
| Fig. 35. LINE GRAPHS DISPLAYING ETCHING SELECTIVITY (LEFT) AND DOF (RIGHT) FOR SEVERAL SLM GENERATED CONICAL PHASE MASKS FOR VARYING PULSE ENERGY AND PULSE DURATION. IN EACH CASE, THE LASER POLARISATION WAS CIRCULAR AND THE TRANSLATION SPEED WAS 4 MM/S. THE UNCERTAINTY IN THE SELECTIVITY IS APPROXIMATELY 5.2%. | 71 |
| Fig. 36. LINE GRAPHS DISPLAYING ETCHING SELECTIVITY (LEFT) AND DOF (RIGHT) FOR SEVERAL PULSE DURATIONS WITH VARYING PULSE ENERGY AND WRITING SPEED. IN THIS CASE, THE LASER POLARISATION WAS CIRCULAR AND THE AXICON BASE-ANGLE WAS FIXED AT 3.20 MRAD. THE UNCERTAINTY IN THE SELECTIVITY IS APPROXIMATELY 5.2%. | 72 |
| Fig. 37. HEAT MAPS DISPLAYING THE RESULTS OF THE FINAL PARAMETER SPACE INVESTIGATION. THE SELECTIVITY (TOP) AND DOF (BOTTOM) WERE MEASURED FOR CHANNELS WRITTEN WITH SEVERAL PULSE ENERGIES, WRITING SPEEDS, CONICAL PHASE BASE-ANGLES AND PULSE REPETITION RATES. THE MINOR TICK MARKS ALONG THE PULSE ENERGY AXIS REPRESENT DOUBLING SAMPLE TRANSLATION SPEEDS FROM 1 TO 128 MM/S, WHILE THE MINOR TICK MARKS ALONG THE REPETITION RATE AXIS DENOTE BASE-ANGLES FROM 0 TO 4.27 MRAD. CIRCULARLY POLARISED LIGHT WAS USED THROUGHOUT. THE UNCERTAINTY IN THE SELECTIVITY IS APPROXIMATELY 5.2%. | 73 |
| Fig. 38. (A) AND (B) SHOW CHEMICALLY ETCHED TRACKS WRITTEN WITH A VORTEX BEAM TO DETERMINE THE MAXIMUM Z-SPACING FOR CONTINUOUS MODIFICATION THROUGH SILICA GLASS. THE SURFACES WERE FORMED BY RASTER SCANNING 2 MM LONG TRACKS IN 2 MM THICK GLASS. NOTE THE MICROGRAPHS WERE TAKEN WITH THE SURFACES TILTED. (C) SHOWS A STAR, TRIANGLE AND CIRCLE WITHIN AN ELLIPSE, EACH INSCRIBED INTO A 1 MM THICK FUSED SILICA SUBSTRATE. THE SEPARATED COMPONENTS, WRITTEN WITH A VORTEX BEAM IN 72 S, AND SUBSEQUENTLY ETCHED FOR TWO HOURS, ARE SHOWN IN (D). (E) AND (F) ARE SURFACE PROFILES OF THE 1 MM THICK ETCHED SURFACES INSCRIBED WITH A GAUSSIAN AND VORTEX FOCUS RESPECTIVELY. | 75 |
| Fig. 39. A SCHEMATIC OF TWO BICONVEX LENSES WHERE - A) PRODUCES A FOCAL VOLUME AND B) RESULTS IN A FOCAL POINT THAT IS DISTORTED DUE TO THE MATERIAL INTERFACE. | 78 |

| | |
|---|-----|
| Fig. 40. A WRITING OBJECTIVE FOCUSING A LASER SOURCE INTO A TRANSPARENT MEDIUM. THIS SHOWS THAT AS THE DEPTH OF THE FOCUS INSIDE THE SUBSTRATES INCREASES FROM D_1 TO D_2 TO D_3 THE PLASMA GENERATION DEPICTED IN YELLOW DECREASES. THE MATERIAL IS DENOTED AS INDEX n_2 , WHILE AIR IS DENOTED AS INDEX n_1 . | 79 |
| Fig. 41. A VOLUME BRAGG GRATING: DEPICTING THE PERIOD STRUCTURE AXIS MARKED AS GRATING PERIOD AND THE DISTANCE THE STRUCTURE SPANS ALONG THE AXIS MARKED AS GRATING THICKNESS. ALSO DEPICTED IS AN INPUT LIGHT SOURCE AND THE SUBSEQUENT DIFFRACTION ORDERS, DEMONSTRATING THE PRIMARY ORIENTATION THE VBG OPERATES IN THIS CASE. | 80 |
| Fig. 42. A DEPICTION OF THE PROCESS OF MANUFACTURING A VOLUME BRAGG GRATING. SHOWN IS THE DIRECTION OF THE WRITING BEAM RELATIVE TO THE GRATING. THE TRANSLATION DIRECTION IS DEPICTED ALONG WITH THE COMPLETED FIRST LAYER, AND THE SECOND LAYER. | 81 |
| Fig. 43. DEPICTION OF THE NORMALIZED Z_{40} POLYNOMIAL IN GREYSCALE, ALONGSIDE THE EQUATION SHOWING THE POLYNOMIAL THE EXPANSION COEFFICIENT X , AND THE FINAL NOTATION USED. | 84 |
| Fig. 44. (A) ANNOTATED DIGITAL PHOTOGRAPH OF CHARACTERIZATION SET-UP, SHOWING THE HeNe BEAM PATH (RED ARROWS), AND THE SC BEAM PATH (WHITE ARROWS). THE BEAM PATHS ARE FOLLOWED BY A HALF-WAVE PLATE (HWP) AND POLARIZER (POL) FOR THE HeNe AND SC RESPECTIVELY. THE BANDPASS FILTERS (BPF) (FKB-VIS-10, THORLABS) IN A ROTATING TURRET IS DEPICTED ON THE SC LINE. (B) SCHEMATIC OF THE GRATING SHOWING THE GRATING ROTATION AXIS, THE FIRST AND THE ZERO TH ORDERS AND THE POSITION OF THE POWER METER (PM). THE TWO POLARISATION STATES P (P-POLARIZATION) AND S (S-POLARIZATION) ARE ALSO DEPICTED. THIS IS PICTURED WITH: (C) A DIGITAL PHOTOGRAPH OF A SAMPLE IN THE FOREGROUND, AND THE INTEGRATING SPHERE AND A DIFFRACTION PATTERN IN THE BACKGROUND. | 86 |
| Fig. 45. RELATIVE DIFFRACTION EFFICIENCY FOR P- (SQUARE MARKERS, BLUE LINE) AND S- (CIRCLE MARKERS, RED LINE) POLARIZATIONS IN PERCENTAGE WITH RESPECT TO: A) WRITING LASER PULSE ENERGY, SHOWING A PEAK EFFICIENCY FOR HORIZONTAL LIGHT FOR A WRITING PULSE ENERGY OF 400 NJ CHARACTERIZED USING THE HeNe LASER, B) WAVELENGTH MEASUREMENTS USING THE SC ASSISTED BY A SET OF BANDPASS FILTERS WITH A FWHM OF 10 NM AND SHOWING A PEAK AT 633 NM. INSERT: A) DIFFRACTION PATTERN OF THE GRATING WRITTEN WITH A PULSE ENERGY OF 400 NJ, B) DIFFRACTION PATTERN OF THE GRATING WRITTEN WITH A PULSE ENERGY OF 400 NJ WITH THE SC SOURCE WITHOUT THE BANDPASS FILTERS. | 88 |
| Fig. 46. RELATIVE DIFFRACTION EFFICIENCY FOR P- (SQUARE MARKERS, BLUE LINE) AND S- (CIRCLE MARKERS, RED LINE) POLARIZATIONS WITH RESPECT TO NUMBER OF INSCRIBED GRATING LAYERS, FABRICATED WITH A LASER PULSE ENERGY OF 400 NJ. EXPERIMENTAL RESULT MEASURED FOR 60-LAYER GRATING POINTS IS PRESENTED IN A GREY DASHED CIRCLE DUE TO THE RELATIVE DIFFRACTION EFFICIENCY RESULT SIGNIFICANTLY DEVIATING FROM THE GLOBAL TREND PRESENTED. | 89 |
| Fig. 47. MEASURED DIFFRACTION EFFICIENCIES FOR P- (SQUARE MARKERS, BLUE LINE) AND S- (CIRCLE MARKERS, RED LINE) POLARIZED LIGHT. A) FIRST-ORDER DIFFRACTION EFFICIENCIES FOR VBGs FABRICATED USING A RANGE OF PULSE ENERGIES. IT IS OBSERVED THAT DIFFRACTION EFFICIENCIES >40% ARE REALIZED USING A PULSE ENERGY OF 225 NJ. HERE, THE DIFFRACTION EFFICIENCY WAS MEASURED USING A HeNe LASER AT 633 NM. B) MEASURED DIFFRACTION EFFICIENCY VS WAVELENGTH FOR THE VBG FABRICATED WITH 225 NJ PULSES, SHOWING THAT DIFFRACTION EFFICIENCIES ABOVE 40% RELATIVE DIFFRACTION EFFICIENCY COULD BE OBTAINED FOR WAVELENGTHS BETWEEN ~600 NM AND ~1000 NM. | 90 |
| Fig. 48. (A) RELATIVE DIFFRACTION EFFICIENCY VERSUS ABERRATION COEFFICIENT FOR A SET OF VBGs WRITTEN AT MEAN DEPTH OF 900 MM FOR A RANGE OF SLM PROFILES RANGING FROM $Z(0)$ TO $Z(-5)$, MEASURED WITH BOTH P- (SQUARE MARKERS, BLUE LINE) AND S- (CIRCLE MARKERS, RED LINE) INTERROGATION BEAM POLARIZATIONS. A BLUE DASHED ARROW HIGHLIGHTS THE BEST PERFORMANCE IMPROVEMENT WHEN USING THE $Z(-4.5)$ ABERRATION COEFFICIENT MASK. (B) RELATIVE DIFFRACTION EFFICIENCY VERSUS WAVELENGTH FOR A VBG WRITTEN AT A MEAN DEPTH OF 900 MM, FOR CORRECTED (SOLID CURVES) AND UNCORRECTED (DASHED DOT CURVES), FOR BOTH P- (SQUARE BLUE) AND S- (CIRCLE RED) POLARIZATIONS. INSET: THE ZERNIKE POLYNOMIAL COMPONENT OF THE MASK PROJECTED ONTO THE SLM, FOR $Z(-4.5)$ IN GREY SCALE FROM 0 TO 2π . | 91 |
| Fig. 49. A) PLOT OF RELATIVE DIFFRACTION EFFICIENCY VS ANGLE FOR THE REFERENCE ANGLES (DASHED CURVE, LIGHT BLUE), AND CORRECTED VBG WRITTEN AT A MEAN DEPTH OF 900 μ M (SOLID CURVE, DARK BLUE), SHOWING PEAK EFFICIENCIES AT -4.5° AND -2.5° RESPECTIVELY. B) PLOT OF RELATIVE DIFFRACTION EFFICIENCY VS WAVELENGTH FOR THE REFERENCE GRATING AND THE CORRECTED GRATING AT 900 μ M, AT -4.5° AND -2.5° RESPECTIVELY. | 92 |
| Fig. 50. SCHEMATICS OF THE PLASMA IMAGE CAMERA SETUP. DETAILS THE CAMERA, THE ZOOM LENS, THE SHORT PASS FILTER, THE NEUTRAL DENSITY FILTER, AND THE POSITION OF THE FUSED SILICA SAMPLE. | 94 |
| Fig. 51. THE NORMALIZED AVERAGE PEAK PIXEL INTENSITY RECORDED WHEN IMAGING PLASMA PRODUCED WITH A RANGE OF ABERRATION COEFFICIENTS AT SHALLOW AND DEEP DEPTHS, NAMELY: 200 MM (SHALLOW REFERENCE, BLACK POINT), 850 MM (DARK-GREEN UPWARD TRIANGLE), 900 MM (GREEN DIAMOND), AND 950 MM (LIGHT-GREEN DOWNWARD TRIANGLE). EACH POINT IS THE NORMALIZED AVERAGE OF FIVE MEASUREMENTS AND THE ERROR BARS REPRESENT THE MINIMUM AND MAXIMUM MEASURED VALUES. THE BLUE LINE REPRESENTS THE RELATIVE DIFFRACTION EFFICIENCY OF A VBG WRITTEN AT 900 MM (INTERROGATED WITH HORIZONTALLY POLARIZED 633 NM LIGHT). | 96 |
| Fig. 52. A SERIES OF UNNORMALIZED PLASMA IMAGES SPLIT BY DEPTH. FIRST SHOWN IS THE 200 MM REFERENCE VALUE WHERE A) IS THE COLOURISED AND SCALED IMAGE, AND B) IS THE ORIGINAL PLASMA IMAGE. SECOND ARE THE 900 MM DEPTH PLASMA IMAGES FOR $Z(0)$ TO $Z(-7)$. IMAGES WERE TAKEN WITH A MONOCHROMATIC CMOS CAMERA, COLOURISED, AND SCALED IN ORIGIN. SHOWN IS THE PEAK PIXEL INTENSITY IN DARK RED FOR ITS RESPECTIVE PLOT. | 98 |
| Fig. 53. SCHEMATIC DIAGRAM OF THE PROPOSED MONOLITHIC SPECTROMETER WITH A MORE DETAILED DESCRIPTION OF THE INDIVIDUAL COMPONENTS. THIS INCLUDED A FIBRE SLOT FOR COUPLING OF SOURCE LIGHT, A VOLUME BRAGG GRATING (VBG) IN THE GRATING PLANE, AND A SENSOR IN THE IMAGE PLANE. | 103 |
| Fig. 54. SCHEMATIC DIAGRAM OF THE REVISED MONOLITHIC SPECTROMETER. THIS INCLUDED A FIBRE SLOT FOR COUPLING OF SOURCE LIGHT, AN EXTERIOR BLAZED GRATING, THE TWO CURVED REFLECTIVE SURFACES, AND A SENSOR IN THE IMAGE PLANE. | 105 |

Fig. 55. SCHEMATIC DIAGRAM OF THE REVISED MONOLITHIC SPECTROMETER WITH THE MAIN COMPONENTS LABELLED AND THE OPTICAL SURFACES HIGHLIGHTED IN RED 106

Fig. 56. SCHEMATIC DIAGRAM OF THE SETUP USED TO TEST THE PROTOTYPE SPECTROMETER. DETAILED ARE THE OPTICAL FIBRE USED TO COUPLE LIGHT INTO THE SPECTROMETER, THE BLAZED GRATING, THE OBJECTIVE LENS, TUBE LENS, AND CAMERA C1. ALONG WITH THIS ARE THE DIRECTIONS OF TRAVEL AVAILABLE TO THE SPECTROMETER AND IMAGING COMPONENTS. 108

Fig. 57. PHOTOGRAPHS OF A) THE PROTOTYPE SPECTROMETER MOUNTED IN THE ANALYSIS SYSTEMS, DEPICTING THE PROTOTYPE, THE GRATING, THE FIBRE SLOT, AND THE OBJECTIVE LENS. B) THE SPECTROMETER AS THE SUPER-CONTINUUM LIGHT IS COUPLED INTO IT, HIGHLIGHTED IS THE IMAGE PLANE ILLUMINATED VIA THE INPUT LIGHT. 108

1. Introduction

1.1 Spectroscopy – techniques and applications

The characterisation of light and optical phenomena is a foundational topic in physics, with definitions changing depending upon the context or field which is being discussed. Despite this one thing is always true: it behaves both as a particle and as a wave [1]. This wave behaviour can be used in the fields of photonics and optics.

In the wave interpretation, light is said to be an electromagnetic (EM) wave - a transversely traveling propagation of electromagnetic radiant energy. The spectrum of EM waves spans from ionizing gamma rays to low-frequency radio waves, crucially containing the typical 'light' wavelengths: ultraviolet, visible, and infrared. Regardless of the area of the spectrum, an EM wave contains a perpendicular oscillating pair of electrical and magnetic fields, with amplitude, wavelength, and frequency components, always moving at the speed of light when in a vacuum. These variables importantly dictate the energy of the traveling wave. There are many demonstrations that can be carried out to show light's wave nature. Overlapping propagating waves interact with each other, producing an interference pattern, this occurs when two or more waves of different phases interact [2]. This can result in greater (constructive) or lower (destructing) amplitude changes. This effect can be produced via double slits, diffraction optics, or prisms [3]. The use of diffraction gratings is ideal for this goal, especially when considering the other important properties of EM waves. Waves at their simplest are monochromatic, an EM wave containing a single wavelength or frequency; this is what is produced by a single frequency light source such as many laser systems. However, they can also be polychromatic, a composite of waves of different frequencies. This polychromatic wave will have a complex wavefront, which can be separated into its individual component wavelengths using diffraction gratings. The ability to take a light source and either measure its wavelength or decompose a complex spectrum into its component parts is an incredibly powerful analytical tool. Studying this decomposition can give insight into a chemical or biological process and any other form of light-matter interaction. The specific tools used to capture and interpret this information are called spectrometers.

These devices are ubiquitous across all fields of science, with a large range of spectrometer architectures, designed and constructed for a specific type of spectroscopic measurement.

To make full use of a spectrometer as a measurement tool it is necessary to first understand the emission and absorption phenomena that can occur during light-matter interactions. The particular absorption and emission characteristics are generally related to the atomic or molecular structure of the studied sample, and as such has an impact on the light they are interacting with [4]. At the simplest level, an atom at equilibrium will have its electron clouds positioned at stable energy levels. Electrons can be moved up energy levels with the addition of energy. However, an electron can only move to discrete well-defined energy levels, therefore the excitation source must have the correct wavelength such that individual photons match the energy transitions. In most cases discussed in this thesis, the source of photons will be a laser. If the energy is insufficient the electron will return to a stable state, emitting the absorbed energy. The emission is typically in the form of a photon of related energy. In the case of a molecule, a bound collection of several atoms, it will then have absorption and emission characteristics dictated by the interaction between the totality of atoms within the system. Again, this includes higher and lower energy levels, but rovibrational states also contribute to the absorption effects. The specific molecular structure results in a unique absorption and emission spectrum, which when captured, can give insights into the underlying processes related to the molecule. In the case of absorption: if a polychromatic source is incident on a sample only the wavelengths of appropriate energy will be absorbed. If the light is not energetic enough for a level change it will be transmitted without absorption. If the spectrum of light that has interacted with a sample is studied, it will be observed that the spectrum will have darker regions compared to the incident spectrum, denoting absorption at those wavelengths. For a solely emission case, a molecule's electrons can be elevated to higher energy levels via many methods: interrogation with EM waves, X-rays, protons are common, but energy can also be injected into a sample electrical using an external power source. The spectrograph of the light produced here will exhibit bright regions but will otherwise be dark. If the sample produces light when probed with light, this is called fluorescence: will

be discussed in section [1.3.1](#). For an illustrative example Fig. 1 depicts a sketch of the absorption and emission process of a hydrogen atom.

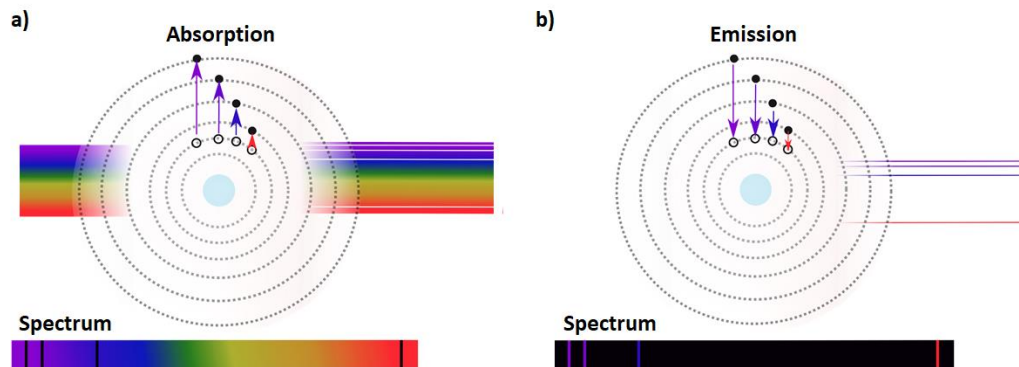


Fig. 1. A diagram illustrating an absorption and emission process for a single hydrogen atom, with an example of the produced spectrum. Detail the absorption of 410 nm, 434 nm, 486 nm, and 656 nm for the former case a), and emission the same wavelength of the emission case b).

To take advantage of these emission and absorption processes specialized spectrometer devices need to be manufactured. The method of collecting a light signal, and how that light is analysed is dependent on the application and can take a range of different forms. Applications are wide-reaching and varied, ranging from biomedical science to astrophysics with different wavelength ranges, and different mechanical requirements. Even within disciplines, there is a huge range of “architectures” - the way a device is spatially laid out.

1.2 How is spectroscopy from the UV to mid-IR conventionally performed?

1.2.1 Introduction

Despite the differences between all architectures of spectrometers, they all require similar processes: a way of collecting the light, a way of transforming the light into a form that can be studied, and a means of detection. The form each of approach, as well as any other components present in the spectrometer, are all tailored to the specific application.

1.2.2 Dispersive spectrometer

One of the more straightforward spectrometer architectures uses some form of dispersive component. This component spatially separates the individual spectral components from the optical beam. This is commonly known as a dispersive spectrometer and the dispersive component can take the form of a range of different diffraction gratings or a prism. Once the source light has been

separated out, each order can then be individually measured using a detector. An early but important example of this dispersive type spectrometer, used a prism to measure the spectrum of a sodium lamp [5].

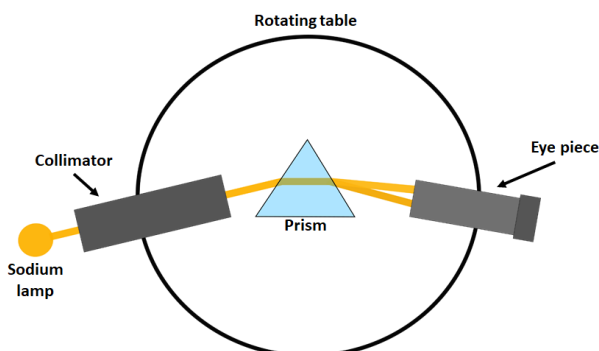


Fig. 2. A schematic diagram of the basic sodium spectrum experiment. Depicting: the sodium lamp, collimator, prism, rotating table, and eye piece. The light path is shown passing through the prism and forming the sodium d-line.

While a relatively straightforward experiment, its use of minimal components (sodium lamp, collimating lens, glass prism, a rotating optical table, and an eyepiece for viewing) has made it a staple of undergraduate teaching. The typical setup depicted for undergraduate teaching is depicted in Fig. 2. The produced spectrum shows spectral lines specific to the sodium atom, showing an early example of a spectroscopic method for identifying an elemental or molecular compound. The prism in this case separated the light from the lamp into two wavelengths which is called the sodium d-lines after their Fraunhofer spectral line designation. As the field developed, photographic film was added, aiding in the recording of the spectral data. This was of course then replaced with digital methods of data capture in modern spectrometers while the prism is often replaced with a diffraction grating.

A diffraction grating produces similar results to a prism but physically they are totally different. A diffraction grating is typically a surface with some kind of periodic structure. This periodic structure can take the form of mechanically scored marks on a metal surface or regions of differing refractive index in either two or three dimensions. The final separated-out spectrum is also slightly different where different wavelengths of light are diffracted at a set specific angles into specific diffraction orders [6]. The separation of the orders as well as the efficiency of the diffraction is related to the dimensions of the grating. This includes: the spatial frequency of the repeating elements, the ratio of the material between periodic sections, the shape or extent of index change of the material, the axial

thickness of the grating, the angle relative to incident light, and the material the grating itself is made from. The fundamental equation is shown in equation (1), where d is the grating period, λ is the wavelength, n is the diffraction order, and θ is the angle of diffraction.

$$d \sin \theta = n\lambda \quad (1)$$

The schematic in Fig. 3 shows the basic operation of a binary grating when illuminated with white light (broadband source).

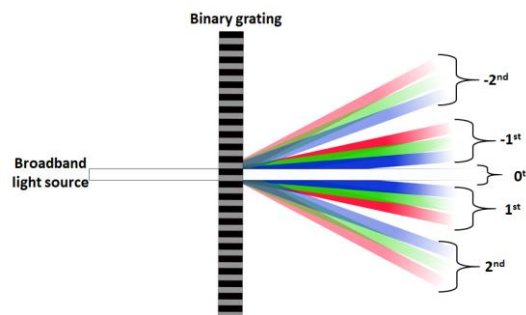


Fig. 3. A schematic of a broadband light source incident with a binary diffraction grating. The diffracted light is separated out both in wavelength and diffraction order, with the power in each order decreasing from the zeroth order.

A binary grating has a simple repeating pattern of elements of the same amplitude, which in this case are equally sized and spaced. The light, when it is polychromatic, will be split into individual diffraction orders as well being separated out as a factor of wavelength. With the central order being the zeroth, and the power distribution reducing with each subsequent order. Of course, this diffraction pattern spans some distance tangential to the grating depending up the size of the input beam, which can be limiting depending on the application, but it is by no means the only way of gaining useful data from a light signal.

1.2.3 Fourier spectrometer

Modern dispersive spectrometers use detector arrays to detect the spatially dispersed signal. There are applications, however, where large format detector arrays are either not available, or they are expensive e.g., the mid-IR. For such applications, it is possible to use Fourier transform spectroscopy. In this case, the optical signal analysed with an interferometer and the signal can be analysed using a single pixel detector. Fig. 4 shows an interferometer, one arm of which contains a mirror or retroreflectors whose position along the optical axis is modulated, while the other arm contains a static reflecting surface.

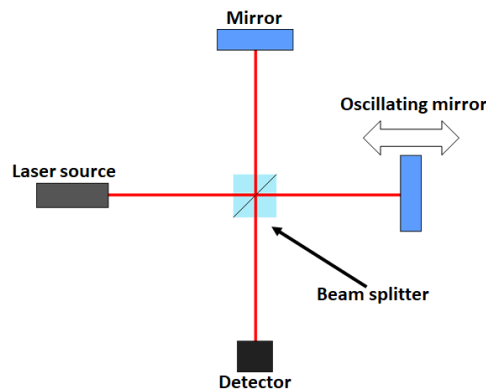


Fig. 4. A schematic of a basic interferometer set up. Depicting: A laser source, a static mirror, and oscillating mirror, a beam splitter, and detector.

The modulated beam is overlapped with the reflection from the static arm via a beam splitter which produces an oscillating interferogram, a plot of light intensity in time / distance. This data set contains all the wavelength information, which can be extracted using a Fourier transform. This takes the data and in effect changes its dimensionality resulting in a plot of optical power density as a function of wavelength. It has the advantage of digitally recorded data, ready for post-processing and signal filtering for noise reduction, but it is still limited in that it cannot provide phase-related information. This technique is implemented in many scenarios but a particularly interesting one is FTIR (Fourier transform infrared) spectroscopy [7].

1.2.4 Homodyne and heterodyne spectrometers

To gather phase-related information along with frequency information a homodyne or heterodyne spectrometer can be used. Both systems make use of a single input signal and share a similar concept: the light being studied is compared to a reference signal. In the homodyne configuration, a single signal is split into two, where one is then modulated. This modulated source acts as a reference called the local oscillator. The unmodulated beam is used as the systems probe. Both signals are then combined before detection. This is in effect removing the unaltered components from the light, leaving behind only the results of the preceding interaction. This system is insensitive to fluctuations of the laser and is ideal for the measurement of weak or low-intensity signals from the probe source, with the local oscillator source providing a level of compensation for the reduced signal. An adaptation of this is the heterodyne spectrometer architecture, which uses two separate signals: a probe signal and a local oscillator. The resulting combination of these two signals is then either the sum or

difference of the two frequencies, with an increased intensity compared to the probe signal in isolation. It is ideal for weak signals and frequency instability in the light source. An interesting example include: frequency modulation (FM) which has been demonstrated to effectively measure weak absorption and emission signal with nano scale resolution [8].

1.2.5 Fabry-perot interferometer

There are other spectrometer devices which an interferometer architectures: for example the Fabry-Perot interferometers based spectrometer. This architecture uses a cavity formed with two partially reflective surfaces. This allows for the introduction of light into the cavity when it meets the cavity's resonance condition. As the light circulates a portion of the light exits from the second surface. After a series of other such transmissions, the total transmission of light is capture. Fig. 5 is a schematic of its operation, detailing the two surfaces of separation d , the light oscillation in the cavity, and the transmission of the $m+1$ order. This is alongside a representation of the interference fringes m and $m+1$ as it would appear after the focusing lens.

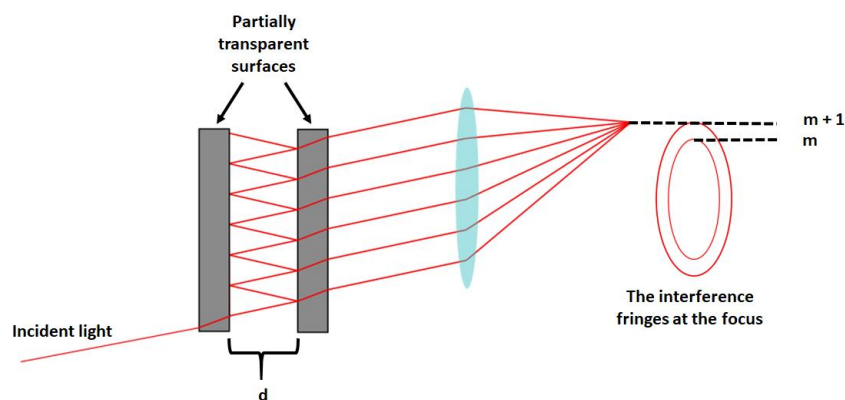


Fig. 5. A schematic of a Fabry-Perot cavity. Detailing the incident light, the two partially transparent surface, the beam oscillation within it, and the transmitted light forming the $m + 1$ fringe order. This order is also depicted alongside the m order, forming a set of concentric rings.

The complete interference pattern is a series of concentric circles the separation of which can give insight to the wavelength of the incident light source. Due to this, this architecture is well suited to spectral analysis. The high reflectance gives the cavity a high finesse, with the wavelength being adjustable via the cavity spacing [9]. The resulting compact size and use of stable components make it useful for satellite based spectrometer for atmospheric measurements [10].

This is by no means a comprehensive list of ways spectroscopy can be performed, and as we go forward to application specific designs many new architectures and spectrometer components will be introduced. These are, however, a foundation of knowledge by which alterations are made to fit a project's specifications. What follows are more examples of spectroscopic techniques but with a primary focus on the application and how that changes the spectrometer's architecture and design considerations.

1.3 Applications of optical spectroscopy from the UV to the mid-IR

1.3.1 Biological, medical, and chemical applications

As stated before, context is everything when it comes to the final decision on how a spectrometer is to be designed for a particular application. Raman spectroscopy is a spectroscopic technique that is widely used in materials science. It can be non-destructive, meaning no permanent damage to the sample is incurred, making it ideal for fragile samples. However, it is a difficult process to achieve the non-destructive regime due to high power requirements needed to compensate for the weakness of the Raman scattering signal. Raman spectroscopy relies on inelastic scattering where incident photons excite to a vibrationally excited state via an elevated virtual state. Since energy must be conserved in this inelastic scattering process, the Raman scattered light provides information about the chemical bond structure in the material [11]. This has its own limitations as the Raman signal is typically very weak either requiring long acquisition times or specialised optics. However, this has been compensated for by using different forms of analysis of the captured light, using an interferometer or through the Fourier spectrometer detailed above. This particular method has been put to use with both in-vitro and ex-vitro measurements of cancer cells in soft tissue areas, such as the brain and lung, as well as protein identification [12,13]. These Raman spectrometer types are often paired with some form of flexible probe or articulated viewer and have become more common in clinical scenarios.

Vibrational spectroscopy, the study of the vibrational state, is not just used in Raman, but also for mid-IR spectroscopy. As the name suggests it is a form of spectroscopy which exclusively uses wavelengths within the infrared regime. This wavelength range only excites or vibrates electrons in

covalent bonds, which have a range of different motions or modes that absorb different wavelengths present in the infrared regime. The absorption is dictated by the chemical or molecular structure of a sample, and thus are unique for each chemical compound. When a sample is exposed to a range of frequencies (typically separated into bands of near-, mid-, and far-infrared) the re-emitted spectrum will have a distinct fingerprint with missing frequencies, due to the absorption of vibrational modes. This spectrum is typically measured via Fourier transform techniques [14]. With its low energy it is ideal for non-destructive and non-invasive medical imaging with examples including detection of infant cerebral palsy [15]. It is also used in the agriculture industry for large scale quality insurance of materials such as soil [16].

A further and versatile spectroscopy technique is fluorescence lifetime spectroscopy. This comes in many different forms depending upon the application, but all revolve around a physical process. Fluorescence lifetime (FLT) is a measurement of the time a fluorophore spends in the excited state before reducing energy and emitting a photon. A fluorophore itself is a fluorescent chemical or molecule which will emit a photon once excited. The FLT of any particular chromophore can range from pico- to nano-seconds depending upon the molecules being studied [17]. One example of a techniques used to perform FLT analysis is time-correlated single photon counting (TCSPC). This common technique uses both a reference and a probe signal. Data is captured via timing electronics which are started with the detection of a reference light, then stopped by the detection of the probe source fluorescence. A histogram of fluorescence intensity vs time will be produced by the electronics [18].

1.3.2 Temporal measurements

Related to FLT are time-correlated measurements in general, which is enabled by the advent of readily available ultrafast laser sources. Such time-resolved measurements have many applications in different fields but all work on the basic principle of measuring the time between processes with an accuracy from second to femtoseconds, and even attoseconds. Such time-resolved measurement can come in many forms: for example, transient absorption spectroscopy where a sample undergoes initial

excitation via a pump, which is then followed by a probe pulse via an optical delay line [19]. In general, this method is limited primarily by the pulse duration of the laser: the shorter the pulse duration the higher the achievable temporal resolution. This technique has recently been revolutionised by the development single photon avalanche diodes (SPAD) and other precision counting technologies [20].

1.3.3 Astronomical and spatial applications

Spectroscopy can be used to measure a range of physical phenomena, both temporal and spatial, as well as chemical and molecular interaction. For example, there are several ways to perform distance measurement using spectroscopy. A method for very long distances would be spectroscopic parallax, which is used in astronomy for measuring the distance of stars. To perform this method the star's apparent brightness must be measured and compared against the spectral type of the star. This is in effect a ratio of apparent brightness vs absolute brightness. This has provided distance measurement up to a limit of around a thousand parsecs, however this won't be the true distance as this method does not include the extinction of the source light due to its propagation through interstellar space [21].

For shorter distance, from micron to meters, a frequency comb has been used. In general, a frequency comb is a series of equally spaced frequency lines, often generated by overlapping two separate waves. One way this can be used for distance measurement is by separating one frequency comb signal into three channels - one channel acting as a reference, one which propagates some distance, and one which monitors the repetition-rate. By comparing these channels the distance can be found from the phase difference [22].

Such a wide and diverse field as astronomy has many more specialized spectrometer devices for specialised applications. A large amount of knowledge can be gained from studying a star's light, in addition to its distance from an observer or its chemical makeup. Another use is for the discovery of extrasolar planets through a method called Doppler spectroscopy. A star is said to 'wobble', to move away or toward an observer as a planet or significantly large celestial body orbits. This causes the light spectrum to shift, blue as it moves towards the observer and red as it moves away. From this periodic

Doppler shift it is possible to infer the radial velocity of the star and therefore the mass of its companion. This has proven to be a highly effective detection method allowing ground-based telescopes to identify hundreds of exoplanets [23]. The system struggles with the non-uniform light output of stars, misidentifying them as planets. It also orientation depended, struggling to make accurate measurement when the celestial bodies move perpendicular to the observer. A similar method can be used to garner insight into other celestial bodies, by observing the red or blue shift in their spectrum as they move through space. The same process has been applied on a planetary scale as well, by taking wind speed measurements of the atmosphere of Venus and other planets in the solar system [24].

1.3.4 Standoff detection of hazards

An application which encompasses many of the spectroscopic techniques covered so far is the standoff detection of hazards. One of the major benefits of optical spectrometers is the ability to probe an area or object using a laser source. With the appropriate optics, light can be sent and then collected over very long distances, allowing detection of an area which may be hazardous. Spectrographic techniques such as IR spectroscopy, FLT, and terahertz spectroscopy have been tested in their use for standoff detection of explosive devices. This typically requires direct line of sight with the sample, but work has been conducted on detection of hazards behind opaque objects, such as explosives within cars [25]. Size is also an important factor - Raman based spectroscopes in particular have been reducing in size, making them ideal candidates for hand held hazard detectors in a forensic situation, allowing for the identification of chemical compounds on sight and without requiring the manual collection of samples [26].

1.4 Integrated spectrometers

1.4.1 What do we mean by an integrated spectrometer?

With the growing ubiquity of spectrometer devices and the development of new fabrication techniques, it was inevitable that attempts would be made to shrink devices and improve their resistance to environmental strains. As has been clear in the preceding section, there is a large market

for compact spectrometers for mounting on handheld devices, satellites, and drones - all situations where space may be at a premium and correction to misalignment may be impossible. Due to this constraint typically, these integrated spectrometers need to be passively aligned, in which the device in its totality had no moving components. These integrated systems can contain light capture and detection systems, or they can be outboard of the spectrometer. In this scenario the spectrometer acts as a static component to a larger diagnostic platform.

1.4.2 Integrated spectrometers – state-of-the-art

A spectrometer device can be manufactured out of a single piece of substrate. This has the advantage of allowing a small-scale, passively aligned device that can be produced, where the only additions are an input light source and a detector. These integrated devices are often made with lithographic techniques, where integrated versions of mirrors, lenses, and diffractive elements can be made to design, such that they are passively aligned. While not allowing for any post-manufacturing adjustments, but with the added stability, this makes it ideal for small-scale spectrometer devices with a reduced chance of misalignment in adverse conditions. With the current state of bulk material manufacturing centimetre scaled versions of Fourier transform spectrometer, dispersive spectrometers and others have been developed [27].

A microring resonator is a type of optical cavity. In isolation, an optical cavity or resonator is a circuit where the light is continually propagated. A microring resonator specifically works as a wavelength filter. Cascading ring arrays can be used for wavelength division multiplexing (WDM), which in essence can be used to take polychromatic light and separates it out into discrete frequency bands, resulting in higher-order filter characteristics. This has many uses with compact integrated spectrometer devices. The sensitivity they can add to a system is also an advantage in particular for chip based bio and chemical spectrograph, an electron microscope image of such a device is show in Fig. 6 [28].

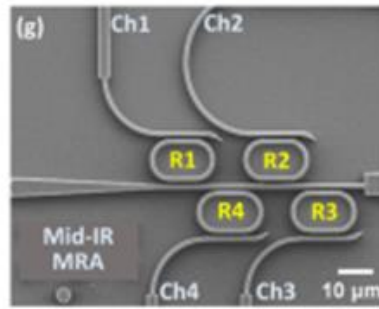


Fig. 6. A microring array captured by an electron microscope [28].

Their compact size means they can be used in other spectrometer devices such as a Fourier transform base system. This allows for an increase in the spectral resolution while maintaining a compact size [29].

An echelle grating is a low groove density grating optimized such that it can be used at high diffractive orders. The benefit of this grating for spectroscopy is that it keeps distinct wavebands widely separated. This, however, comes at an increased possibility of desired wavelengths overlapping when diffracted at such high angles. To counteract this, when being integrated into a spectrometer, they are typically paired with a prism to separate the orders and/or a mechanical slit to filter out orders which may be unnecessary. This ensures the desired operating potential of the device. Despite these requirements spectrometers of this type can be compact, with high resolution and high data acquisition speeds. They have been put to the test in the design and manufacturing of spaceborne probes for the analysis of the planet Venus. This was combined with an acousto-optic tuneable filter and aimed primarily at the infrared wavelength band [30]. A CAD representation of this system is depicted below in Fig. 7.

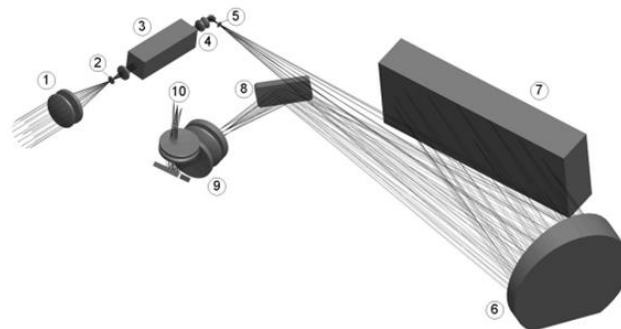


Fig. 7. A CAD representation of an echelle grating based compact spectrometer device [30]. Primary components are detailed along with the beam path where 7 is the echelle grating and 10 is the detector.

There are further interferometer designs that can be used in integrated spectrometers such as the Mach-Zehnder interferometer. This is used to find a shift in the phase of two collimated light paths, both originating from the same source, but where one is modulated by the sample being studied and the other acts as a reference. A basic Mach-Zehnder is depicted in Fig. 8.

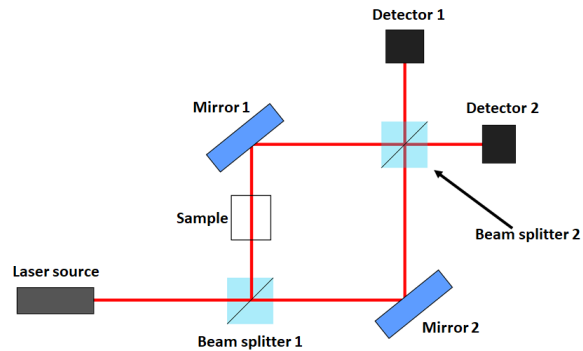


Fig. 8. A basic Mach-Zehnder interferometer. Detailed in the laser source, the two beam splitters, mirrors and detectors, along with position of the sample being studied.

The beam paths, one modulated via the studied sample and the other unaffected, are propagated through opposing sides of a partially reflecting surface (in Fig. 8 this takes the form of a beam splitter). Both beams interact forming an interference pattern at the two surfaces, leaving two signals and thus two detection points. When two detectors are placed on either side of the partially reflecting surface - one detector will detect the constructive interference, while the other receives destructive. In the latter case, in a scenario with no sample there will be a zero signal. This relatively simple layout is ideal for integrated spectrometer designs, with its limited number of components, requiring two mirrors and two beam splitters. Mach-Zehnder interferometers have also been manufactured using waveguide arrays. This is a highly space efficient method of manufacturing this spectrometer, making it ideal for lab-on-chip applications requiring arrays of interferometers on a single device. This has been put to use in the manufacture of a spectrometer array with resolutions of 0.025 nm as well as increased optical throughput [31]. This was shown for water vapour mid-IR spectroscopy, with Fourier transform analytical methods.

Arrays of waveguides can also be used to create an integrated form of an Echelle grating. Typically called arrayed waveguide gratings (AWGs) these devices operate by coupling a broadband light source into a set of single mode optical waveguides. Each of the optical waveguides have a

different length and therefore applies a wavelength-dependent phase shift that acts as a higher-order diffraction grating. Individual wavelength can then be imaged directly or coupled into further optical waveguides. It has the advantage of low cross talk between the fibres and has many application fields such as astronomical spectroscopy [32]. Fig. 9 is an image such a device taken from a 2017 publication.

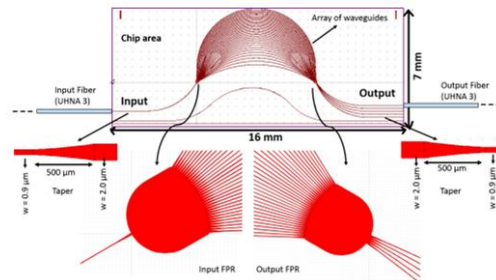


Fig. 9. A schematic of a AWG device taken from a publication [32]. Shown is the array of waveguides itself, as well as the input and output couplers. Contained also as close up images of these features.

AWGs have been combined with photonic lanterns, a photonic device which can couple light between single-mode and multi-mode optical fibres. These device in combination have been used to make the PIMM device – photonic integrated multimode spectrograph [33]. This proposed device acts as a small-scale spectrometer whose function is independent of the telescope used to source the input light. The design also open avenues for situation specific modification and allows for complex astronomical measurements with lower cost and space restrictions.

1.5 The Aim and Motivation behind this project

1.5.1 Proposed design

This project proposes to develop a Czerny-Turner type spectrometer manufactured from a single monolithic fused silica glass sample. The Czerny-Turner is a monochromator architecture and is commonly used in spectrographs as a way of dispersing polychromatic light. This design typically includes two curved reflecting surfaces and a diffraction grating [34]. The basic form of such a spectrometer is depicted in Fig. 10.

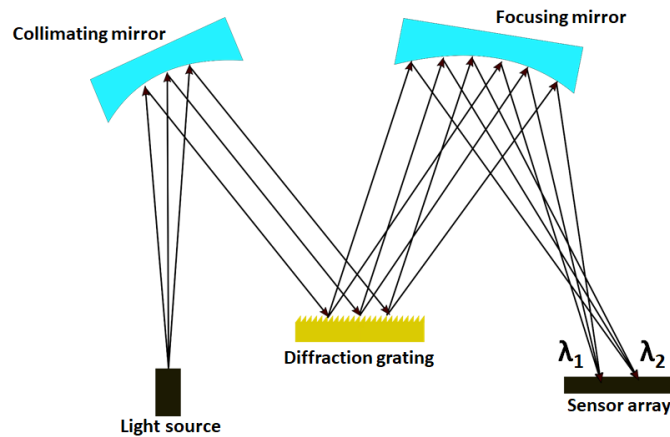


Fig. 10. The basic layout of Czerny-Turner spectrometer. Key components are depicted including: a light source, the collimating mirror, a diffraction grating, the focusing mirror, and a sensor array.

The layout is very versatile, the use of two mirrors allowing a second set of x , y , z , and tip-tilt steering as well as beam expanding and focusing qualities. The components can also be orientated in a range of different ways, assuming the alignment is maintained. This makes the spectrometer well suited for applications where space is at a premium, with the caveat that the components must be correctly selected and aligned. Alignment can be challenging with added degree of freedom making alignment relative to the diffraction object more complex. This can also be compound if the device requires regular realignment, otherwise more cost and testing would be needed to sufficiently shock resist the device. These drawbacks are counteracted with a monolithic design. With a sufficiently high-quality design and simulation stage before manufacturing, the ideal spectrometer layout can be pre-determined. Once a satisfactory design has been finalised the parameters – mirror curvature, grating period, and their relative position to the input and output component – can then be recreated in the chosen substrate using a computer-controlled manufacturing method. From there, alignment is then static with instabilities in the system unable to misalign the optical components. The spectrometer also benefits from the choice of substrate, in this case fused silica. Fused silica is highly chemically resistant when pristine (unaffected by any form of modification) while also being highly transmissive. Fig. 11 shows the proposed Czerny-Turner spectrometer design; both the ray diagram produced by Dr. Calum Ross in the Zemax ray tracing software, and a schematic diagram detailing the important components.

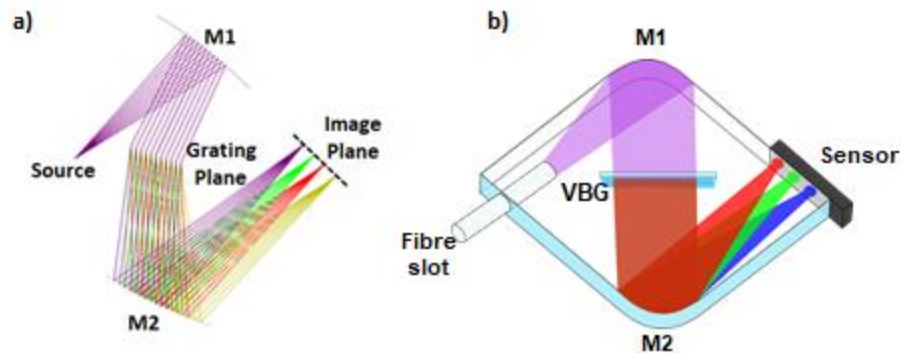


Fig. 11. a) Ray diagram of the proposed monolithic Czerny-Turner spectrometer produced in Zemax by Dr. Calum Ross. Detailed following the source is the collimating curved mirror M1, the Grating plane, the focusing curved mirror, and finally the image plane. b) Schematic diagram of the proposed monolithic spectrometer with a more detailed description of the individual components. This included a fibre slot for coupling of source light, a volume Bragg grating (VBG) in the grating plane, and a sensor in the image plane.

Fig. 11. b) details an important aspect of the design - a fibre slot. This slot allows for the passive alignment of an optical fibre for the coupling of an exterior source light. The slot/source in a) is followed by a first mirrored surface M1. The curvature of this is such that the source light is collimated and directed to the grating plane. In the Grating Plane a Volume Bragg grating (VBG) will act as the diffractive element. VBGs will be detailed later in this project, but in short, the extra parameters provided by the VBG will allow more control over the desired wavelength response and diffraction order position. This is followed by M2 a curved mirror used to focus the diffraction light into the Image Plane. The Image Plane itself is where a sensor or camera will be placed to study the diffracted light.

There are many microfabrication methods that can build such a device, however ultrafast laser inscription is an attractive choice. This method allows volumes within a transparent medium to be molecularly modified, while leaving the surround material pristine. The modification also has tuneable effects; low power can produce a permanent refractive index change, while higher power can make the structure of the substrate more susceptible to selective chemical wet etching. By combining these processes, most of the components in the proposed device can be manufactured with any exterior component, optical fibre and sensor, being passively aligned to the device. Selective chemical etching can be used to create curved surfaces for the mirrors, as well as the fibre slot. The mirror will, however, most likely need to be metal coated to ensure high reflectance. The pure modification mechanism can then be used to generate a VBG. The present design uses a sample 50 mm × 50 mm × 0.5 mm fused silica sample, with a VBG designed for the visible light spectrum.

With such specific requirements, the current standard of the ULI writing system was not suitable enough and such most of the focus of this project is on the development of further advancements to the conventional writing system. The added flexibility presented here resulted in significant progress towards this proposed design, as well as allowing more usability from the ULI in general, contributing to other projects.

2. In-volume modification of dielectrics using ultrafast laser pulses

2.1. A history of in-volume modification

2.1.1. Introduction

With the rise of complex photonic applications, there is a need for a method of bespoke manufacturing within transparent materials – a fabrication method that does not require glass grinding or machine shaping while maintaining the optical qualities of the material is in high demand. Such a method would need to be flexible, cost-effective, and would allow for a wide range of transparent materials to be processed. Due to this demand, progress in this area has been steady over the last few decades, driven by the availability of high-power laser sources. Such sources are required due to transparent material's large bandgap, where lower energy sources simply propagate through the material. The early stage of in-volume modification made use of the rapid development field of lasers while latter iterations took advantage of cutting-edge pulsed sources, however, it began with high-energy UV light sources.

2.1.2. UV base material modification

Early photolithographic techniques to overcome the large bandgap of transparent material used high-energy nanosecond pulsed UV light and photosensitive materials. With this technique, the UV light energy is larger than the bandgap, enabling absorption of light and therefore a permanent modification, however, this cannot be achieved with all transparent substrates. This method requires the use of photosensitive materials. These are typically doped glasses or polymers, with some materials requiring heating after exposure to fully develop the modification [35]. When the conditions for modification are achieved there is a permanent structural change in the material – these can be observed as refractive index changes, structure damage, densification, or nano-crystallization, depending up on the substrates and pulse energies used [36].

When the exposure parameters are appropriately tuned to induce a material change, UV light illumination has been used to micro-fabrication several different types of photonics devices. An early example was the manufacture of reflective filters within the core of silica optical fibres [37]. An Argon laser was focused into the Ge-doped core of an optical fibre.

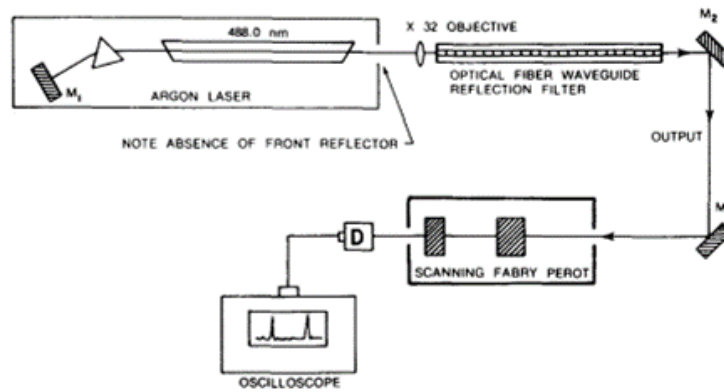


Fig. 12. A schematic diagram of the Argon laser testing setup, used to measure the effectiveness of the reflector. Detailing primary components, taken with permission from the publication by K. O. Hill et. al [37].

When the light, focused through the fibre, interacted with the doped core it resulted in a positive refractive index change - which, when coupled into both ends of the fibre generated an interference pattern that forms the periodic refractive index change. This example provided a high-resolution wavelength filter, ideal for high-capacity wavelength-multiplexing commonly found in communication systems. The system used to test the performance is depicted in Fig. 12, taken directly from the publication.

As this method developed, beam shaping was added into the inscription system, which allow further complexity to the inscribed structures. One interesting example used a photolithographically imprinted phase mask, applying technique called side illumination, which generated a binary structure made from monolithic silica glass. The grating is designed such that the light pattern formed in the material has a periodicity of the desired final Bragg grating, which was imprinted, again, in the core of an optical fibre. Fig. 13 depicts this process, showing a UV light order diffracted by the phase mask and how the overlapping diffracted orders interact with the dope fibre core.

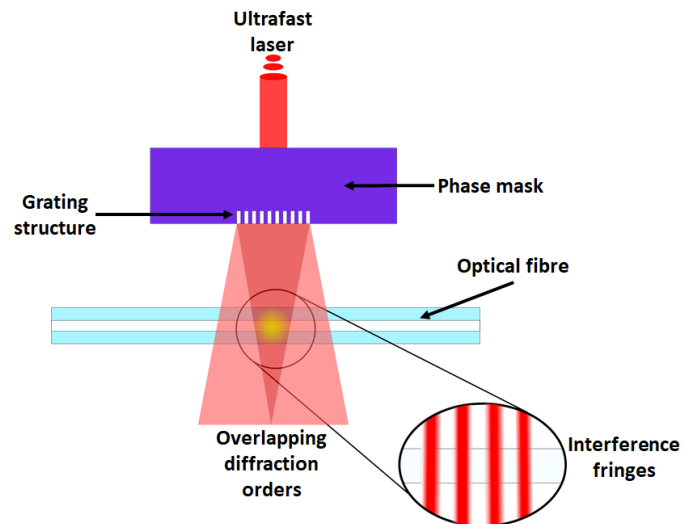


Fig. 13. A schematic diagram of the phase mask writing systems, detailing the incident UV light, the grating, and the diffracted order. Shown also is the optical fibre and the fringes that interact to form the material modification [38].

When the UV source is diffracted by the phase mask and orders interacted with the core of the optical fibre, the interference pattern that is formed imprints the Bragg grating [38]. The addition of such a phase mask allows for added repeatability as well as fine-tuning of the desired parameters prior to the imprinting process. However, they do require a large diameter beam to fabricate large structures, or else the material must be translated through interference pattern. While it has it a wide range of uses, UV material modification does have its limitation – it can only manufacture within photosensitive materials regardless of whether the device requires a phase mask or not. For similar reasons, only high-energy UV sources can also be used. This is a major limit to the possible applications of such manufactured devices. However, many of the steps and techniques present in these and other examples do set a standard for what the preceding process and systems will need to be capable of.

2.1.2. Development of high peak power pulsed laser sources

To fabricate structures using sub-bandgap radiation it is necessary to exploit nonlinear absorption processes. This in turn required the use of pulsed lasers, which can deliver the required peak powers. For example, when an ultrafast laser pulse is focused inside a transparent material, the peak electric field strength can equal or exceed the electric field that binds valence electrons to atoms or molecules. To enable such high electric fields, a new source of high-energy pulsed light was required. In the case of UV modification, for example, nano-second pulsed laser systems were selected because of the higher peak power when compared to continuous wave sources. However, with limited peak powers,

these examples compensate with certain wavelengths of light and the materials selection, restricted to those that are optically sensitive. To achieve modification in arbitrary transparent materials a new method of pulse generation was required.

As new methods of laser pulse generation have become widely available, pulsed systems have become common in laboratories with many uses in contemporary physics, surpassing continuous wave (CW) systems in some lab scenarios. A CW laser is a laser that produces a continuous stream of photons, generating a continuous light wave. In general, the average power achievable from a CW lasers does not allow us to access nonlinear light-matter interaction regimes, restricting their use in material processing and preventing their use for in volume modification. The solution is to use pulsed laser systems, which generate of a series of discrete pulses with higher peak power than a CW laser that emits the same average power. These pulses come in a series of intervals called the repetition rate and span a period called the pulse duration. These two parameters, when tuned appropriately, can be used to get specific light-matter interactions, and can be generated is a range of different ways.

A basic form of pulse generation developed in the 1960s was Q-switching, which is capable of nanosecond pulse durations [39]. The pulse is generated via an intra-cavity component which reduces the quality factor of the cavity while the gain medium is being pumped. This causes energy to build up in the laser gain medium. Once the gain medium becomes saturated, the cavity switches to a high Q state and produces a high energy light pulse. The light is typically low repetition rate with long pulse durations however the nanosecond range pulse duration does limit the available pulse energies to produce nonlinear absorption effects. Shorter pulses, from picoseconds to femtoseconds, require the use of the mode-locking technique, which was introduced shortly before the 1970s [40]. This method is more complex and relies on coherently adding multiple longitudinal modes with fixed phase differences within the laser cavity to synthesize a short pulse. Mode-locking can be enabled using passive or active techniques, using different forms of saturable absorber or an external modulator device. While this method can generate femtosecond pulses necessary to enable peak powers that

can in principle drive nonlinear absorption mechanisms, it does however lack the appropriate pulse peak power to drive the bridging of large bandgap materials such as fused silica.

The peak power that was achievable with femtosecond pulse systems remained capped until the 1980s, when chirped pulse-amplification (CPA) was developed [41]. This Nobel Prize winning process involves first stretching a short laser pulse via a highly dispersive optical element, typically achieving the stretching via a diffraction grating, prisms, or long optical fibres [42]. The pulses then pass into an amplifying medium where the energy of the pulse is increased. After amplification, the pulse is compressed using a pair of diffraction gratings or similar. These steps can achieve ultrafast pulse durations with high peak powers, reaching the gigawatt, terawatt and even petawatt range. With CPA, the appropriate combination of high peak power and short pulse duration allow for in volume modification of traditionally non-photo sensitive high-bandgap materials such as fused silica. Despite being cutting edge, many of the principles used for UV modification do still apply for ultrafast laser system and will be the focus of the following sections.

2.1.3. In volume ultrafast laser modification

With the development of CPA, a range of new materials were available for in volume modification. Much like with UV based modification a cylindrical lens and phase mask system can be used to inscribe periodic structures. Such a method has been used to inscribe Bragg reflectors in optical fibres and volume Bragg gratings in bulk fused silica [9,10]. Fig. 14 is a schematic of such a writing system.

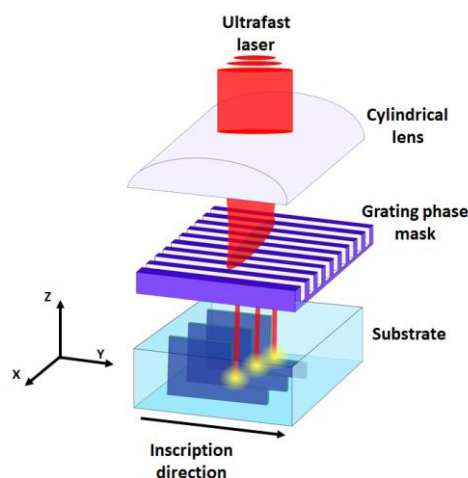


Fig. 14. A schematic diagram of the cylindrical lens and phase mask base writing system using an ultrafast laser source. The primary optical components have been detailed, and the position of modification highlighted in yellow.

Figure 14 details the main components of a cylindrical lens and phase mask based writing system. In this example a volume Bragg grating is being manufactured in a monolithic substrate. Material is first modified along the y axis by translating the sample through the beam. Depth can then be added to the VBG by adding a further layer of modification along the z axis.

While the cylindrical lens and phase mask system can be a highly effective method of fabrication, it is highly dependent on qualities of the phase mask. To remove this dependency, direct laser writing was chosen for this project. This approach involves focusing ultrafast laser pulses directly in a substrate via a compound objective lens, with the focal volume determined by the parameters of the objective in combination with the properties of the laser pulse. This system benefits from the greater control of the peak power distribution within the focus volume. Furthermore, the tight focus enabled by the use of a high NA objective lens can provide in-volume modification with higher spatial resolution. However, this approach does require the use of computer controlled 3-dimensional translation stages, with a detailed understating of its operation and limits to allow for the inscription of arbitrary structures. Fig. 15 is a schematic of the basic operation of this system.

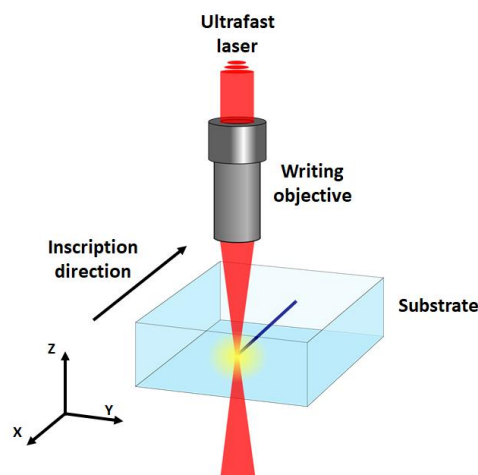


Fig. 15. A schematic diagram of the objective based writing system, detailing the writing objective, the translation direction, and the point of material modification (highlighted in yellow).

Figure 15 depicts how an ultrafast laser focused can be focused into a substrate material using a microscope objective lens to drive nonlinear absorption in the focal volume. The inscription “direction” is also indicated in the figure, which represents the direction that the substrate is moved during the inscription process. There is of course a lot more to discuss regarding direct laser writing

(also called ultrafast microfabrication or ultrafast laser inscription or ULI) which will be covered as this thesis continues. The focus of the following sections is to layout the current standard of ULI, both the system's setup and the different applications devices manufactured from such as system can be applied to.

2.2 The basic experimental setup

There is a set of key components which are required to make up the current standard of ultrafast laser fabrication systems. The first component is the choice of ultrafast laser source. As CPA has become widely adopted there are many different possible laser systems to choose from. For the work outlined in this thesis, we chose to work with the 1030 nm light generated by a Light Conversion Pharos laser system. The Pharos is a Yb:tungstate regenerative amplified system that is ideally suited for this device fabrication due to the highly adaptable laser output – enabling the laser parameters to be tuned to suit a particular applications. The pulse duration can be varied from ~ 185 fs to ~ 5 ps, well within the boundaries required to drive nonlinear absorption and allowing for fine tuning of the desired response with the material. This is assisted by the wide range of possible repetition rates spanning from 1 MHz to single pulse. Finally, the systems exhibit a maximum output power of 10 W, allowing for power to be lost as the beam propagates through the other components in the system. Fig. 16 shows the standard components which then follow the laser source.

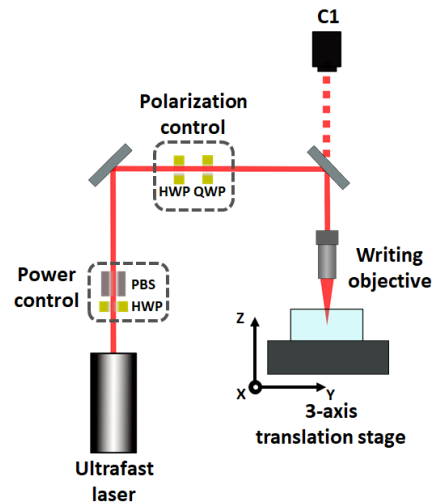


Fig. 16. A schematic diagram of the current standard of ultrafast laser microfabrication system. The ultrafast laser system depicted was the Light Conversions Pharos. This is followed by Power control provided by a polarising beam splitter (PBS) and a half-waveplate (HWP). Following this is Polarization control provided by another HWP and a quarter-waveplate (QWP). Finally there is the final writing objective. The objective leads to a sample mounted onto a 3-axis motion control translation stage. C1 is a camera arranged such that it captures light reflected off the sample, allowing for it to be position appropriately.

The laser is followed by power control and polarization control systems. This is necessary to ensure that changes in power and polarisation can be controlled and synchronised via the same software which drives the motion of the translation stage. For our purposes, the laser power on the substrate was controlled via a half-waveplate (HWP) and a polarising beam splitter (PBS). This was then followed by polarization control via another half-waveplate and a quarter-waveplate. There will be some loss of laser light associated with these components, but the amount of loss is not critical due to the high output power available from the Pharos laser. The final optical component is the objective lens which is used to focus the laser light into the substrate material. Appropriate selection of this lens is crucial to the operation of the ultrafast laser inscription system. The parameters of the objective lens, such as its NA, focal length, and working distance, have a considerable effect on the flexibility of the system and will be covered in a further section. By mounting the substrate material on a set of high-quality translation stages, near-arbitrary shaped modified regions can be inscribed within the substrate. The positioning of the substrate can be monitored using the camera C1, allowing for the sample to be position appropriately before the inscription is initiated. Many of the key parameters are set by the laser and can be used to change the extent of the light-matter interaction, which is key to the nonlinear absorption effects.

2.3 The physics of ultrafast laser inscription (ULI)

2.3.1 Light-matter interactions

As outlined in Section 1.1, if light of a sufficiently energetic wavelength interacts with a material, individual photons can excite electrons from the valance band to the conduction band. This is however not possible for longer wavelength with their lower energies, as laser material processing relies on the ability to induce the nonlinear absorption of light using high peak intensities. This can be enabled by using ns, ps or fs pulses of light. If the irradiation of the substrate material is controlled appropriately, nonlinear absorption can be utilised to induce a permanent in-volume modification to the structure of a dielectric materials. A diagram showing the distinct interaction present when ultrafast light has been focused are detailed in Fig. 17, recreated from a detailed review paper [45]. As shown in Figure 17 there are the interactions and mechanisms which need to take place for the material to result in modification, the specifics will covered in detail on the following paragraphs.

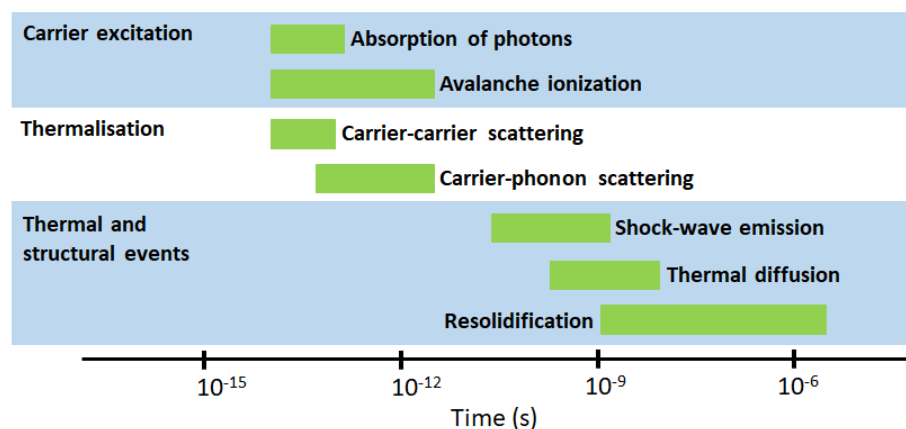


Fig. 17. Detailed here are the individual mechanism which make up the nonlinear absorption process separated into carrier excitation, thermalisation, and thermal and structural events. They are displayed with their approximate timescale plotted in seconds with the approximate starting and end times of each sub-process [45].

When an ultrafast laser pulse of sufficiently high energy is focused into a dielectric material, the carrier excitation stage of the process starts, beginning with the absorption of the incident photon. The leading edge of the pulse can excite electrons from the top of the valance band to the bottom of the conduction band through either multiphoton or tunnelling ionisation. These excited electrons then have a continuum of unfilled energy states above them, and so can be further excited through linear single photon absorption (Joule heating). Electrons in the conduction band continue to absorb light in this manner until they have sufficient energy to impact ionise another electron residing at the top of

the valence band – a process known as avalanche ionisation, which causes the density of the free electron plasma to increase leading to the absorption of the remaining pulse energy. This leads to the thermalisation step of the process, once optical energy has been deposited into the hot free electron plasma, the energy is then thermalized across the carrier sub-system through carrier-carrier scattering, and then deposited into the material lattice through carrier-phonon scattering. This is followed by the start of the thermal and structural events. Several nanoseconds after the initial optical exposure a pressure wave separates from the heated volume. Within a femtosecond of the pulse entering the material the heated volume begins to cool. Once completed a denser volume will remain, producing a permanent refractive index change. With a more energetic exposure the index change will be replaced with either a volume of material with weakened molecular bonds, or in extreme case a hollow volume. This process is highly parameter dependent where subtle changes in pulse energy and pulse duration can result in different outcomes. While this may make the system difficult to optimise, it does offer a very high level of flexibility. This flexibility greatly increases the range of photonic components that can be manufactured, and therefore the applications to which ultrafast laser inscription it can be applied to.

2.3.2 Key material modifications in silica glass and their manifestations

If structural modifications are inscribed using pulse energies only slightly above the threshold for nonlinear absorption and pulse durations below ~ 200 fs it is possible to induce a smoothly varying structural modification which manifests itself through a smoothly varying refractive index change. In silica glass, the maximum refractive index change that can be induced is $\sim 0.5\%$ [46]. Volumes of index change can then be combined to form channels that act as optical waveguides or Bragg gratings.

If the pulse energy or pulse duration is increased beyond that required to induce a smoothly varying structural modification, it is possible to enter a regime where the structural modification involves the creation of periodic sub-wavelength nanogratings. These self-organising periodic nanogratings form perpendicular to the polarisation of the writing beam. This is due to the formation of a disk-shaped plasma volume created by the optical field enhancement within the material,

deforming the normally spherical or elliptical optical volume. The periodicity, as well as the consistency, of the structure is typically dictated by the number of pulse incident on the materials volume. Similar nanogratings have been formed in several doped borosilicate glasses and sapphire but have been studied extensively in Fused silica. These structures manifest themselves through form birefringence, which can be used for a variety of applications, including the creation of novel types of waveplate and data storage. One particularly useful manifestation is the increased susceptibility to chemical etching, which can be used to create a large variety of functional components e.g., microfluidics, micromechanics and micro-optics.

If the laser pulse energy is increased beyond that required for nanograting formation, it is possible to create a small micro-explosion, where hot material is driven into the cool surrounding material, leaving behind a micro-void, which again can be used for applications such as volume gratings and optical storage. Beyond just the pulse duration and energy, there are many parameters which can be tuned to arrive at the desired modification type, volume of modification, and so on. Each variable including a review of pulse duration will be briefly discussed in the following.

2.3.3 The ULI parameters and the roles they play

2.3.3.1 Laser wavelength

In-volume processing of dielectric materials requires the use of sub-bandgap wavelengths. The available wavelengths for ultrafast laser microfabrication are generally limited by the laser sources that are available from commercial ultrafast laser systems that supply μJ level pulse energies. There is however a relatively subtle effect on the writing ability for a given wavelength. While there is very little difference in the quality of the modification when all parameters are the same, there can be a changing in the threshold energy required to bridge the band gap in certain materials. Therefore, the selection of wavelength is dependent upon the flexibility of the prospective laser system. Different wavelengths will require different peak pulse energies - this will also change depending upon the band gap of the selected material. Furthermore, different wavelengths have different diffraction and absorption characteristics, and where certain wavelength will fail to reach of suitable compact enough focal region for some writing application. For this case, using fused silica, near-IR was an ideal choice.

2.3.3.2 Laser polarisation

The selection of polarisation is dependent upon the application – specifically when writing structures to be chemically etched. In that case it is important to have the laser polarisation to be perpendicular to the direction the sample is being translated in. This ensures the nanogratings, which are key to the etching process, are appropriately aligned. When the nanogratings are aligned to ensure a cohesive surface the final surface will have a higher surface quality. With structures inscribed in all three x-, y-, and z-axis, it may be necessary to vary the polarisation arbitrarily. This requires a method of active polarisation control, ensuring a constant level of modification. This is the primary reason the polarisation control detailed in [2.2](#) is computer controlled. Being able to synchronise stage motion and polarisation is a major advantage when inscribing complex structures.

2.3.3.3 Pulse energy

Pulse energy is one of the most important of the ultrafast laser inscription parameters, since small changes to the pulse energy can drastically affect the type of material modification that is generated in the focal volume. As discussed in section [2.3.2](#), when working with fused silica as a substrate material, there are three main modification regimes, primarily determined by the pulse energy used. If too low a pulse energy is used, the peak intensity in the focal volume will be too low to drive nonlinear absorption processes. There will be no transfer of energy from the pulse to the material and no modification to the material. If the pulse energy, and therefore the peak intensity, is only slightly higher than that required to drive nonlinear absorption then the threshold is smoothly varying structural modification can be induced that exhibits a spatial scale that can be controlled via the lens used to focus the pulse inside the material. This smoothly varying structural modification can manifest itself through a positive change in refractive index, which can then be used to inscribe structures such as optical waveguides. If the pulse energy is increased further, it is possible to inscribe structures that contain nanogratings, that manifest themselves through changes in the chemical etch rate and birefringence of the modified material. If the pulse energy is increased even further, the modification can take the form of microvoids or cracks in the material.

2.3.3.4 Pulse duration

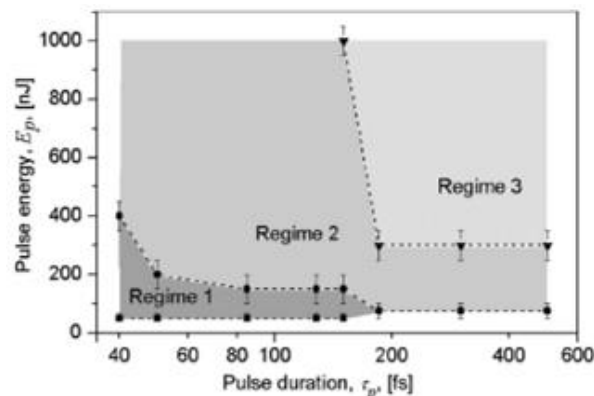


Fig. 18. A plot of pulse energy vs pulse duration detailing the transition zones between different modification regimes, regime 1, 2, and 3. Results were obtained with a fused silica sample [47].

The pulse duration can also be used, to some extent, to control the fabrication regime. As shown in Fig. 18, for example, when using a pulse energy beyond 400 nJ it is possible to transition from Regime 1 (the smoothly varying structural modification regime) to Regime 2 (the nanograting regime) and then Regime 3 (disrupted modification regime) simply by increasing the pulse duration beyond ~ 200 fs. Much like all aspects of ULI, the parameters ideal for producing a certain outcome in a particular glass or crystal substrate material do not always hold when using a different material. This project will focus solely on fused silica, and as such the following sections will be discussing just this glass. When inscribing below 190 fs, and with low pulse energies, the form of modification present in fused silica is said to be in Regime 1. In this regime the modification is said to be ‘pure’, where the laser exposed volume contains primarily refractive index modified material. This is the primary reason for the strict pulse energy and pulse duration parameters, and why the Pharos system was selected. This project worked in both regime 1 and 2, for the inscription of diffraction optics and channels for selectively etching respectively.

2.3.3.5 Pulse repetition rate

The laser pulse repetition rate, or rep-rate, is the last key laser parameter. The rep-rate controls the rate at which laser pulses are exposed to the material. Using a higher rep-rate laser allows the material to be translated faster while delivering the same number of pulses per unit length, but the laser rep-rate can also affect the type of modification that is induced in the material. This is because heat takes a finite amount of time diffuse away from the focal volume. Since this time is of the order of $1 \mu\text{s}$,

incident pulses will arrive on cooler material if rep-rates below ~ 1 MHz are used, and hotter material if rep-rates above ~ 1 MHz are used. Therefore, if lasers with sufficiently high rep-rate lasers are used, this can drive the process of thermal accumulation, achieving substantially higher temperatures in the focal region than can be achieved with single pulses of the same energy.

2.3.3.6 Focusing optics.

The objective lens used to focus the laser into the substrate controls the size and shape of the focal volume, and such the spatial distribution of the induced modification. However, this distribution is also strongly impacted by the pulse energy and pulse duration required to modify the substrate material. The main properties of the objective are its working distance, numerical aperture (NA) and throughput. When selecting an appropriate objective lens, a balance between each parameter is required, as these parameters will impact the volume and the extent of modification in the material. The throughput of the lens will affect the maximum amount of power that is available in the system, while the NA will determine the shape of the focal volume. Working distance is also vital in this project, where a longer working distance allowed for thicker substrate material to be used for different applications. Inscribing deeper within a material does have its own limitations, caused by aberration effects, which will become more relevant as the study continued.

2.3.3.7 Substrate translation velocity

If all other parameters are held constant, the substrate translation velocity effectively controls the amount of modification that is induced in the material without changing the material modification regime. When inscribing individual tracks, a slower substrate translation velocity can be used to induce a higher index or material change, up to some maximum. Higher translation velocities can reduce inscription time but will also lower extend of modification, meaning there is a limit on how fast you can inscribe a certain structure.

2.3.3.8 Substrate material

In many cases the material will be determined by the application of the final device. Each material requires an independent parameter study to find the ideal inscription parameters. This project solely used fused silica glass, although extensive studies has been conducted on many glass and crystalline

materials. Fused silica has broadband transmission (including the near- and mid IR regimes) and is highly chemically resistant without reducing inscription and etching fidelity.

2.3.3.9 Substrate scanning strategy.

Ultrafast laser inscription can be used to inscribe near-arbitrary volumes of material modification inside dielectric materials. To build-up these volumes requires the formation of multiple laser-inscribed “tracks” layered together, inscribing the necessary surface or channel the devices or structure requires. Thus, the substrate scanning strategy is an important consideration when fabricating complex structures.

2.4 Applications of ultrafast laser inscription (ULI)

2.4.1 Refractive index modification

2.4.1.1 Optical waveguide inscription

As discussed earlier, optical waveguides are a basic building block of integrated photonic components that can be manufactured using ULI and are some of the earliest examples of direct laser written structures. The 1996 paper demonstrated tracks of modified material with an elliptical cross section [48]. These were inscribed in a range of silicate glasses with an 810 nm femtosecond laser source, using direct laser writing via an objective lens. The paper proposes the uses of these tracks for beam guiding purpose, where the damaged region can confine and guide propagating light. This proposal for direct laser written optical waveguide was developed further in 1998 where a similar laser system was used to manufacture pure modification light guiding channels [49]. The publication shows optical waveguide whose core diameter could be modulated via the input power, allowing for the inscription of single and multimode waveguides.

By the mid-2010s, optical waveguide manufacture via ULI had development to the point where they are now an emerging manufacturing technique for industrial applications. The different types of waveguides that can be made are commonly split into three categories, which are represented in the previous examples. Waveguides which guide light between pairs or arrays of damaged material are called type II and type III respectively [50]. The advantage of this method is

diameter of the guiding cavity can be adjusted via the spacing of the damaged track. Type I refers to waveguide written using pure modification, as demonstrated in the 1998 publication. The simplest form of these produces a single mode optical waveguide. Fig. 19 depicts these three main types, showing region of pure modification and material damage in pristine material. The light guiding cavities of type II and type III waveguides are also marked [49].

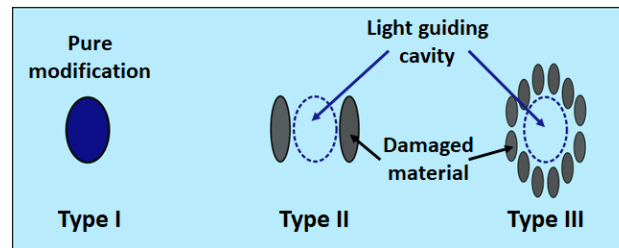


Fig. 19. A sketch of the three standardised waveguide types. Type I: pure modification, type II: two parallel lines of damaged material with the guiding cavity in the centre, type III: an array of damaged material forming the light guiding cavity.

A further advancement to this method is the manufacture of multimode waveguides. These can be made by writing multiple tracks within close proximity, a process called multiscan [51]. This does come with its own limitations - requiring multiple identical tracks means an increase in manufacturing time. To reduce this inscription time beam shaping has been used elongate the focal volume in one axis. By constraining the beam via a mechanical or digital slit multimode waveguide can be writing as few as one track of modified material [52].

Along with the singlemode and multimode guiding structures the inscribed tracks can also be used for evanescent field coupling. When two ULI written waveguides are written close to one another there is a level of cross coupling, the magnitude of which can be precisely controlled via the interaction length and waveguide-to-waveguide separation [53].

A further example of optical waveguide-based structures that can be manufactured using ultrafast laser inscription is a 3-dimensional optical reformatters. One particular example here is 3D 'fan-outs' which reformat optical signals, for example from a multicore fibre, into a linear array for coupling to a standard photonic integrated circuit. One recent devices involved a ULI written fan-out that could reformat light from a 121 core multicore fibre and separating it out into a defined pattern. This device exhibited an insertion loss of around 1.7 dB [54]. Another example of a ULI fabricated

optical reformatter is “integrated photonic lanterns”. A photonic lantern is a device which takes a multimode source and redistributes it across a series of single mode waveguides. [55].

Applications for ULI fabricated waveguides extend well beyond optical reformatters. The wide range of materials that ULI can be used in allows specialised doped glasses and crystals to be applied to certain applications. This has uses in waveguide optical amplifiers. By laser writing a waveguide into an optically active gain material, it can increase the output of a laser coupled into the material. For example, using Er-doped GeGaS glass shows a net gain of 16 dB [56]. With appropriate development and coupling such a device can make for a compact and efficient alternative to other methods of optical amplification.

ULI can also be used to fabricate waveguide lasers. This is a major benefit for solid state laser systems. A solid-state laser typically uses a solid gain medium such as a crystal line or doped glass substrate, in contrast to other laser systems which use gases or liquids (there are also optical fibre based solid state lasers). Typically, these types of lasers involve the imbedding of a waveguide within a section of gain medium. The gain medium is then inserted into an optical cavity and coupled into some form of pump - in many examples this is a diode laser. If appropriately developed, this approach results in a high power single mode laser, which is compact and rugged [57]. Common lithographic techniques can be used to manufacture such gain mediums, however ULI is well suited to this application – allowing for modification of bulk materials.

2.4.1.2 Diffractive structures

Light guiding structures are not the sole use of ULI, it can be used to manufacture a wide range of diffractive optics. Making use of the refractive index change, ULI can be used to write a series of lines parallel to each other. When incident light interacts with these lines it diffracts, in a manner like the way light diffracts from gratings made using lithographic techniques or even by simply scoring a metal surface. The grating parameters can be tuned by varying the spatial dimensions, but also the ULI parameters. The most common type of ULI fabricated gratings is the transmissive grating, which is fabricated by writing lines of index modification within the volume of a material. Light passes through

the glass, where it is then scattered when it encounters the modified regions. At normal incidence the diffraction pattern will be as expected with a monochromatic source: producing spaced orders with decreasing power distribution leaving from the central 0th order. However, when a tilt is applied to the grating, the power distribution across the diffracted orders can be changed - this is called applying a blaze or simply a blazed grating. This is used to direct more power into a specific order. The application of these gratings is relevant to the project and will be covered in more detail as the thesis progresses. Of course, with such a versatile manufacturing system many different grating types can be manufactured, in particular Volume Bragg gratings (VBG), a device that benefits from ULI. A VBG is a grating which spans a volume within a substrate, containing not only a period of parallel lines of modification but also a significant thickness of the grating spanning perpendicular to the lines' writing direction. This added parameter gives VBGs a level of flexibility in terms of the wavelength response that can be encoded into the grating. ULI's advantage here is that the process will result in an embedded grating while maintaining the pristine nature of the surrounding material. The computer-controlled precision of the ULI system is also an advantage when tuning the response of a 3-dimensional device.

2.4.1.3 Optical storage

In the current digital world, there is a need for more forms of data storage. By using ULI, high capacity, low energy, and long lifetime optical storage devices can be manufactured. The first approach here used ULI and higher energy pulses to form voids within a material. The position of voids in the material in effect form the binary digits from which data can be written and read. There can be many different ways to read the inscribed data: one foundational example uses the Nomarski differential interference contrast laser microscope [58]. Optical storage devices using voids can be very data dense and can use the material's inherent resistance to decay to store the data over long periods of time. Further development from this involves using more complex written structures. Instead of individual voids, shapes with a defined direction can be inscribed: this give a further dimension in which to store data which can further increase the storage density [59].

Recent progress in optical storage device from Microsoft has shown the use of nanograting instead of material voids can further increase the storage capacity. Current examples show evidence of a 5-dimensional storage solution where data is encoded via layers of ULI inscribed nanogratings, the birefringence of which encodes the stored data. The data can then be read by studying the polarisation angle change and retardance that nanograting applies to an interrogation beam [60]. This method of data storage is proposed as a low cost and stable form of cloud storage.

2.4.2 Selective chemical etching

2.4.2.1 Introduction

Selective chemical etching has just as many applications as refractive index change and has been used to manufacture a wide range of optical devices. Individual tracks or arbitrary shaped surfaces can be inscribed and etched. A basic demonstration of chemical etching capabilities is using it to dice material or to produce a hollow channel. The former case is depicted in Fig 19 as Set 1, where 1(a) shows the modified material, (b) shows the void produced during the chemical etching process and, (c) shows the final sample split in two. Set 2 in Fig. 20 shows the steps for a channel along the axial extent of the beams focus, with modified ring marked out in (a), (b) shows the void created during the etching and (c) shows the final channel.

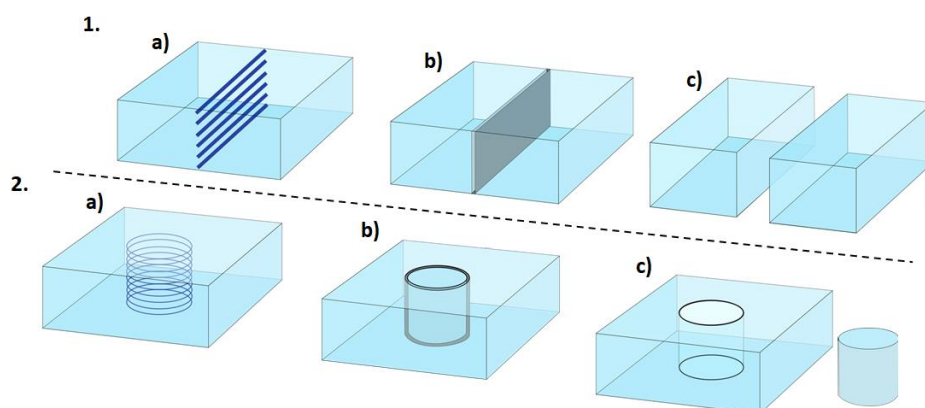


Fig. 20. 1: dicing of a substrate using chemical etching assisted ultrafast laser inscription. Detailing steps – a) the initial modified regions, b) the modified region being removed via the chemical etchant, and c) the final outcome with the sample diced into separated section. 2: the removal of material from a sample producing a hollow channel. Detailing steps – a) the initial modified regions, b) the modified region being removed via the chemical etchant, and c) the final outcome with a hollow channel etched into the substrate and the cylinder of removed material.

As Fig 20 demonstrates, the shape and position of the modified regions has a major effect on the outcome of the etched material. The choice of chemical etchant also has a considerable effect on the

selectivity of the etching - the ratio of etched pristine and modified material. The chemicals range from bases to acids, diluted and heated and is typically selected based of the sample being etched. For fused silica, hydrofluoric acid (HF) was originally used as an etchant, although its use within the field has gradually been replaced by potassium hydroxide (KOH), which not only provides higher selectivity, but is also significantly safer to use [61]. For other examples, such as crystalline materials, H₂O₂ and NH₄OH mixtures have produced high selectivity results [62]. This project was primarily focused on fused silica and KOH: the particular temperatures and dilutions, as well the goals of the study will be detailed in the relevant section.

2.4.2.2 Microfluidics

A basic application of chemical selective etching is that it allows the fabrication of hollow channels in a bulk substrate. These channels are written much like pure modification tracks but with pulse energies sufficient to alter the molecular structure such that the modified volume become susceptible to chemical etching. While coming with their own challenges (such as over etching) these channels have been applied in a wide range application and devices in particular microfluidics [63].

An interesting example is the use of micro fluid channels for 3D liquid mixers. These structures would be difficult to fabricate without ULI, with channels written in different axes forming a series of interconnected cells. The orientation of these channels allows liquids to flow together and passively mix, giving result far beyond what is achievable with a one dimension mixers [64].

Microfluidic channels can also be used in lab-on-chip devices, specifically for analysis or spectrographic purposes. The main advantage of a lab-on-chip structure is the system of liquid separation and delivery can be designed in tandem with the spectrometer device, resulting a system which requires less optical and fluidic alignment or mechanical assistance to function as desired. Examples have such fluid channels paired with an AWG, and operate via measuring the chemical fluorescence [65].

In a similar vein these channels have been used for cellular analysis. More specifically they have been used to make a cell stretcher, where a microfluidic channel is flanked on both sides by

optical waveguides. When a cell flows through the channel a laser coupled into the fibres traps the cell. The force exerted upon the cell by the laser light can then be used to stretch or squeeze the cell. This gives a viewing window to study in detail the cell with a certain level of control provided by tuning the laser power. A particularly interesting example used this process to trap and stretch a red blood cell, however data acquisition was limited due to the surface quality of the channel obscuring the view to the cell [66]. Surface quality is a challenge associated with much of chemical etched device. Such a device can be further augmented with different sensors and sorting channels for further application specific readings.

In a similar fashion these channels have been used as part of a selective plane illumination microscopy (SPIM) on-a-chip device. SPIM is a measurement technique with high spatiotemporal resolution. It uses a side mounted light source to illuminate a single section of a biological sample. Then by scanning this light up and down this sample a series of image sheets of different cross sections can be acquired. This is a typically fast microscopy technique which reduces the possibility of photo-damage, meaning living samples can be studied. The ULI written device contains an input and output tube. This is used to 'flow' sample within the field of view of the microscope. There is also a slot for a passively aligned optical fibre, in front of which a cavity acts as a focusing objective and can be filled or empty with differing refractive indexed liquids. This cavity is arranged so that it creates the light sheet to cross-section the samples as they pass through the objective's field of view. The main advantage of this design is that its small size and portable nature allows for any standard fluorescence microscope to be converted into a SPIM system [67].

2.4.2.2 Micro-optics

Ultrafast microfabrication assisted chemical etching has further uses: when volumes of modified materials are stacked together they can be used to manufacture whole surfaces. A simple example involves individual tracks the width of a glass sample stacked together which when etched will in effect dice the material. With correct motion and polarization control the same technique can be used to make arbitrarily shaped surfaces including spherical and hemi spherical shapes. These types of

surfaces are useful for the manufacturing of microlenses. A particular focus has been microlens arrays, a periodic structure of identical lenses used in small scale applications. These are used in devices such as projectors, cameras, medical instruments, and applied in fields such as optical communications. One method of making such an array involves inscribing a grid into a glass sample. When chemically etched the gridlines will etch faster than the pristine material between the gridlines. Because of this there will be a gradient of etched material, consistent across the entirety of the sample. The resulting material pattern will depend upon this grid - it can be a series of pyramid shapes, but can be hemispherical or asymmetrical [68]. This can help produce rapid prototypes for testing, with the pulse energy affecting the etch rate and therefore the final shape. The only possible issue would be selecting the ideal pulse energy and etchant: the chemical, as well as the temperature, etching time, and the dilution.

Similarly, such design principles have been used for small scale optical devices for in vivo medical imaging. One interesting design is for a microfiber Raman probe. In many ways it demonstrates many of the relevant design principles that were vital to this project. The probe is made of two separate parts which are joined together using UV curing glue. One is a cylinder which contains passively aligned fibre slots aligned to an array of lenses formed into a 'flower petal' shape. The second part contains a focusing object with one large convex focusing surface [69]. When both probe parts are combined the final device has a sub-millimetre length and diameter, making it ideal for attaching to the current standard of medical imaging endoscopes. The main issues regarding this device - and why it is relevant to section further on in this write up - is the manufacturing times. The curved surface of the cylinder requires layers of modification to be stacked, which greatly increases the manufacturing time. This is an issue that ULI device fabrication struggles with and often holds the system back from mass production applications. Long manufacturing time can also lead to instabilities in the laser or optical system. When the laboratory cools or heats during evenings and mornings, the consistency of the laser writing can be negatively affected typically through things such as shifting in

optical alignment. An example of this temperature change within this project ULI laboratory was captured by Dr. David MacLachlan over a period of 20 hours and is plotted in figure 21.

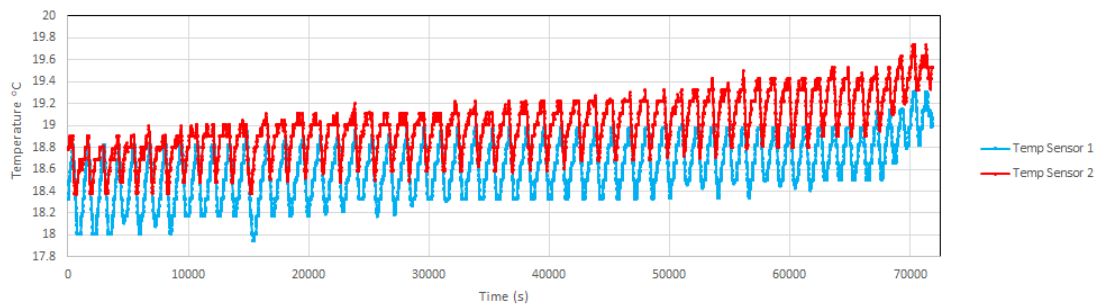


Fig. 21. Plot of the temperature change in degrees Celsius over the course of 20 hour for two sensors in the ULI laboratory.

The plot shows a change in the ambient temperature over time. It also shows that, with two separate temperature 1 and 2 in blue and red respectively, there was also a temperature gradient within the lab. This gave a very general overview of the temperature change over a single day, but not over a longer period or the temperature change on key components.

This project focuses on optical components, but ULI is of course not exclusive to photonic devices. It can also be used for mechanical devices and due to the high precision, it offers it can be a very effective method. A good example is the displacement measuring device developed by Bellouard et al which is partially photonic and inscribed into fused silica [70]. Large volumes of a substrate are removed via the ULI process leaving thin but flexible fixtures. With an appropriate amount of these “flexures” attached to a single slab of materials, the slab can be moved back and forth, returning to an equilibrium position due to the elasticity of the flexures. One end of the slab has an array of waveguides with varying throughputs, while the other end extends outside the device where it can be moved by an exterior source. When the slab is moved the waveguide array will move across the path of another pair of waveguides. This means the light traveling through the second waveguide set will be modulated as the displacement changes. By recording this modulated light the displacement of the slab can be calculated [70]. The main advantage of this silica device is that it can be used in environments where standard electronics may negatively affect, such as areas with a high EM field.

With this foundation of knowledge, the key investigations of the project can be introduced. The focus will be on the limitations in the current standard of ULI systems, how they will affect the

manufacturing of the spectrometer device, and what solutions to these problems can be applied to the system.

3. SLM-enabled focal elongation for reduced manufacturing times

3.1. Introduction to ULI manufacturing times.

The process of ULI enables the manufacturing of precision glass components ranging in scale from μm to mm, and cm in some cases. However, even for small structures, the manufacturing time can be in the scale of hours or even days. This is due to a multitude of factors ranging from the mechanical limitation of translation stages to the limitation of the available laser source, but the primary limitation comes from the complexity of the structure and the small focal volumes of the inscription laser. With a focal volume of a few microns in dimensions, it takes time to manufacture a larger-scale structure or surface. Doing so requires layering together modified regions, which means as the size of the object increases more regions need to be layered, leading to longer manufacturing times. Object size and focal volume limitations will always be the biggest bottleneck when attempting to manufacture devices in small time frames.

Single scan tracks of laser-modified material are typically the easiest and fastest structure to inscribe. For tracks spanning to the edges of a sample, the substrate needs to begin some distance away from the focus of the ultrafast laser system. This distance must be sufficiently long to allow the stages to accelerate to the desired translation velocity, ensuring it remains consistent across the breadth of the modified track. The same holds for the end of the track, as the translation stage requires time to safely decelerate. This acceleration, or ramp rate, and the target translation velocity are set within the stage translation control software, measured in mm/s^2 and mm/s respectively. The distance preceding and following the desired track length is called the runoff and is measured in mm. This requirement is true when using ULI for both pure refractive index modification and chemical etching-rate enhancement applications. As an example, when writing tracks in this project for making VBGs, a velocity of 4 mm/s gave the best modification results. For this, a ramp rate of 500 mm/s^2 over a 0.25 mm runoff was given on each end of the track. This was longer than the minimum needed but ensured the stages could safely accelerate and decelerate while allowing the laser shutter to complete opening or closing. If faster velocities or lower ramp rates are needed due to mechanical or

optical constraints the runoff may require a more precise value. Of course, a single track can take a very short amount of time to manufacture, in the region of seconds depending upon the size of the track; however, this time increases when writing a structure with a larger number of modified tracks. For a simple example, when writing multiscan waveguides, the manufacturing time will be increased proportionally to the number of scans. It's important to note that the time for a single track in this case may also include both the fly back with the shutter closed and bringing the sample into a position from another inscription run. A further complication can be added if the tracks are to be curved because then the translation velocity and stage movements need to be synchronized in such a way as to ensure a consistent arch.

Tracks, even when very long, curved, or combined, are often still on the shorter end of manufacturing timescales, taking from seconds or minutes to several hours. The long manufacturing times occur when writing complex surfaces and three-dimensional devices, which can take days of continuous ULI. The repositioning can be more complex in these cases as well – either including a fly back to the starting position then a change in the z-axis, or a change in the z-axis with the inscription direction going in the reverse assuming the surface is being inscribed tangentially to the x- and y-plane. The former is slower but will produce a smoother surface post-etch due to the consistent alignment of the inscribed nanogratings, meanwhile, the latter is faster but with the alternating nanograting orientations the surface quality is reduced. Larger surfaces also require more tracks with the focal volume dictating the spatial separation between adjacent tracks and therefore the total number of tracks. A longer distance will result in less track per surface but will affect the consistency of material modification. If the separation between tracks is too large, there will no longer be a singular surface, but individual tracks. The Optosigma objective selected for this project produces a focal volume of $\sim 1 \mu\text{m}$ transversely and $\sim 8.3 \mu\text{m}$ axially which, depending upon the pulse energy, allows a track separation of up to tens of μm along the optical axis. If the inscribed surface is millimetres in size it can take dozens of written tracks to complete the whole surface. This is further complicated when attempting three-dimensional devices on the scale of mm or cm. Such large timescales may increase

the risk of instabilities in the laser writing system, impacting the inscribed device. An inscription run over days will have stability issues as buildings heat and cool as the day turns to night, shifting optomechanics noticeably. These challenges will affect the fabrication of the monolithic spectrometer when using the current standard of ULI systems.

In total the proposed integrated monolithic spectrometer device has four surfaces that require chemical etching: two will act as mirrors and therefore need to be curved, one requires a slot for passively aligned optical fibre, and the fourth surface will be the image plane. In addition to these surfaces, the spectrometer also requires a VBG inscribed into the centre of the device. The surfaces themselves may take up to an hour in total, but the VBG will take considerably more time. Work that will be detailed in Chapter 4 showed volume Bragg gratings that were 3.5 mm by 3 mm by 0.1 mm took ~12 hours to be fabricated. However, the spectrometer will require a larger grating 15 mm wide and 100 μm thick, spanning the sample's total z-axis depth of 500 μm , note this axis is relative to both the substrate and the translation stage, each axis is detailed in Fig. 22 – a CAD image of the writing stages, the granite arch, platform and the breadboard.

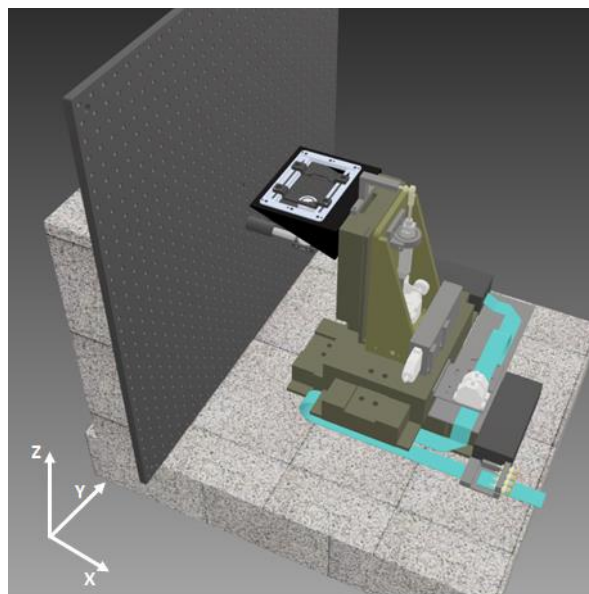


Fig. 22. CAD image of the ULI writing stages produced in Autodesk inventor.

This VBG will require close to a week of continuous writing. For a prototype device, such a time scale may be acceptable, even considering system stabilities. However, if these devices are to be mass manufactured, the time must be dramatically reduced. With current “standard” ULI systems, there is

very little room for optimization. This issue with long ULI manufacturing times is common for all other devices but is a particular issue with the proposed spectrometer. A method of decreasing this fabrication time is required. This would be advantageous for not just the spectrometer but would allow for a wider range of device types to be manufactured using ULI.

The method proposed and implemented here for decreasing ULI fabrication times involves controlling the shape of the writing laser's focal volume, specifically, elongating it. Beam shaping is a vast subject and will be touched on throughout this thesis. In this particular section, methods of elongating the beam will be covered in detail. Beam elongation in this context means enlarging the axial length of the focal volume while maintaining intensity above the modification threshold. This would allow for a larger volume of the material to be modified at once, meaning fewer tracks per surface, reducing the manufacturing time required. The method of achieving this elongated beam is detailed in the resulting publication - reproduced in its entirety in appendix [8.1](#). However, beam shaping and methods of doing so will be introduced first, as this step of the project was key not just for beam elongation but for all results depicted within this thesis.

3.2 SLM-assisted beam shaping for enhanced ULI

3.2.1. The experimental approach

The beam shaping assisted laser writing system used to achieve the goal of increased manufacturing speeds is depicted in Fig. 23 and makes use of an LCOS (liquid crystal on silicon) spatial light modulator (SLM) to drive this beam shaping. Key components are detailed and separated into their spatial planes on the optics table – x / y or y / z .

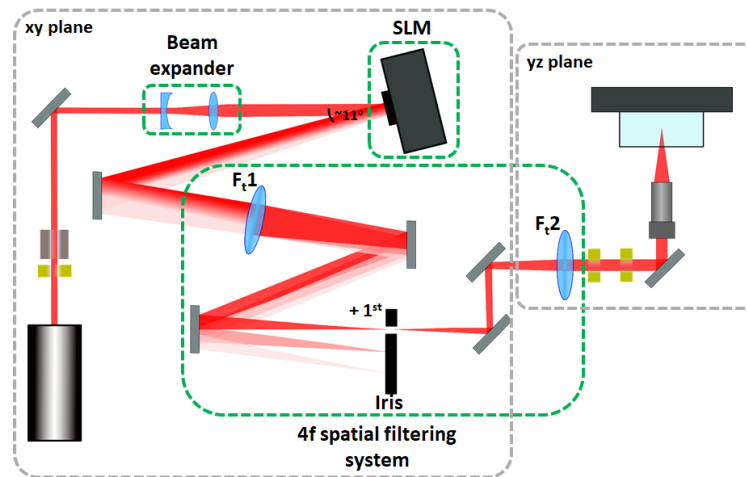


Fig. 23. A schematic diagram of the beam shaping assisted ultrafast laser inscription setup. The new additions to the standard setup are highlighted in the green boxes, including the beam expander, the SLM, and the 4f spatial filtering system. Noted in the spatial filter system are the two Fourier transform lenses Ft1 and Ft2, the iris used to remove unneeded orders, and the position 1st diffraction order. The grey dashed boxes separate sections of the system which are in different spatial planes, these are the xy plane for the first section and yz plane for the second.

Shown are the same primary components that were included in the ULI system schematics in Chapter [1](#) - along with the additional components necessary for effective beam shaping. Immediately following the Pharos and power control system is a beam expander. This is needed to expand the beam width from 4.5 mm to 13.2 mm (measured at the $1/e^2$ points of the intensity profile), slightly overfilling the SLM's 16 mm x 12 mm active area along one axis. The overall fill factor was $\sim 71\%$. While the SLM's operation will be covered in detail in Section [3.2.2](#) it is important to note now that for ideal operation the SLM must have an angle of incidence of around $\sim 5.5^\circ$ (with a total of $\sim 11^\circ$ field of view in front of the SLM). This is to ensure the light interacts with the LCOS array as efficiently as possible.

Following the SLM was the 4f Fourier filter system. The operation of this set of components will be covered in Section [3.2.3](#); however for now it is important to know that the system contained two biconvex lenses which spanned the distance between the SLM and the final writing objective, while also applying the appropriate demagnification to counteract the beam expander. The lenses selected were: a 1000 mm focal length, 2-inch diameter lens (F_t1) and a 400 mm focal length, 1-inch diameter lens (F_t2), both anti-reflection coated for near-IR light. The optics following the 4f system depicted in the y / z plane in Fig. 23, as well as the translation stages themselves, were mounted on a granite platform and arch. This along with the optical table added stability to the writing system. The stages were mounted directly to the platform, while a breadboard was added to the arch for the

mounting of optical components. Fig. 24 is a photograph of the stages, the granite platform and arch, and the breadboard.

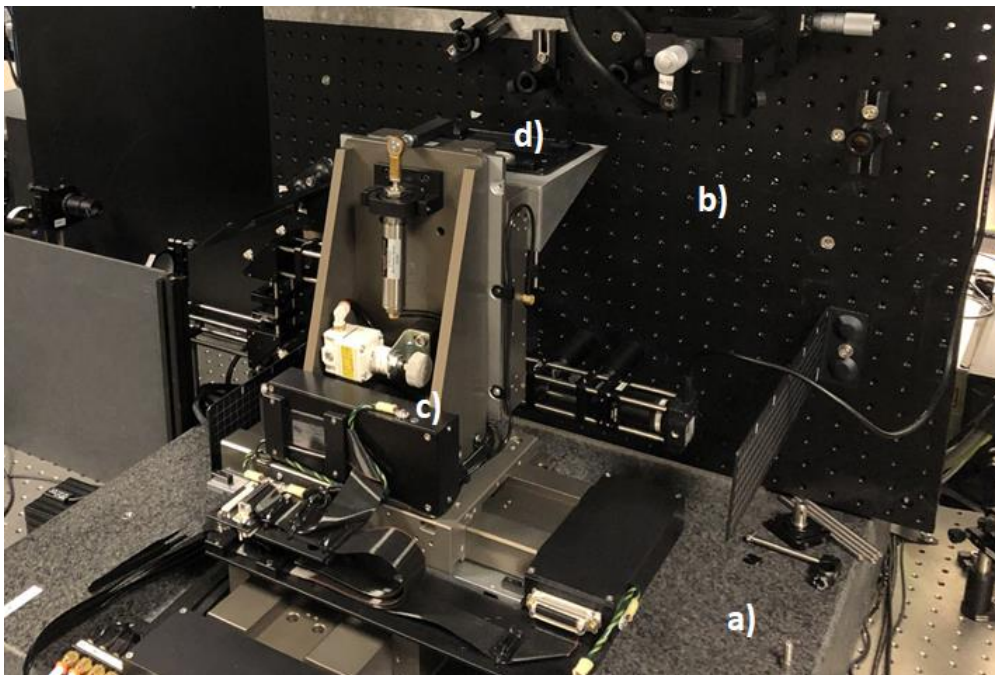


Fig. 24. A photograph of the writing stages detailing - a) the granite base and arch, b) the breadboard, c) air bearing translation stages, and d) the sample mount.

The granite platform (a) measured 715 mm by 675 mm by 125 mm, depicted with the stages (c) attached. On the stages was a sample mount d) where the substrate being inscribed was held. The breadboard (b) measured 750 mm by 750 mm and had a cage system attached - this simplified the alignment of any mounted optics. Mounted on the breadboard within the cage system in the y/z plane were the F_2 lens, the polarisation control system, and the final writing objective. There were also three mirrors with low group delay dispersion dielectric laser line mirrors (042-1030, EKSMA optics). The 4f spatial filtering system, including the SLM, was implemented between power and polarisation control systems detailed in Section 2.2. This was due to the SLM's horizontal polarisation dependency. Horizontal in this case is said to be parallel to the optical table and is the polarisation state outputted by the Pharos. The translation stages were controlled via a piece of software called A3200 which runs off a proprietary scripting language called Aerobasic. An additional piece of coding was required however to allow for control of the power and polarization control systems. This was

written in C++ and allowed for the changing of power and polarisation to be synchronized with stage movements. A similar script was used to control the SLM but this will be covered in Section [3.2.2](#).

For the most part, this system was consistent throughout the entirety of the project, with any change being noted in the relevant sections. The main variable being tuned during the experimentation phase was the laser's parameters and the phase masks projected onto the SLM. These masks were vital to the success of the project and this beam-shaping assisted system. The choice of different phase masks applied and the reasons for this will be discussed in their own dedicated section: in particular, this will detail the blazed grating which was required for an ideal operation of the SLM.

3.2.2. Spatial-light-modulator

A Spatial Light Modulator (SLM) is an optical device that enables the amplitude and / or phase profile of an incident light beam to be actively controlled [71]. Applying a spatial change to light is called beam shaping and has a wide history in optics - in particular, laser microfabrication as detailed in Chapter [1](#) where fused silica diffraction gratings were used as a beam shaping phase mask [38]. The advantage of an SLM over these methods is its digital nature which allows for active beam shaping with essential arbitrary phase masks. SLMs come in several different forms with different methods of interacting with light and ways of applying beam shaping. For our purposes, we chose to use an SLM technology that imparts a computer controllable spatially varying phase profile – this is referred to as a phase-only SLM [72]. This type of SLM applies a phase change in a pixelwise manner to the beam upon reflecting off the active area of the SLM. The active area is the name given to the area that through one means or another applies a phase change. The X13138 SLM chosen was manufactured by Hamamatsu and used an electronically addressed LCOS (liquid crystal on silicon) array as the active area [73]. This LCOS array had a resolution of 1280 pixels x 1024 pixels and a pitch of 12.5 μm , and a pixel bit-depth of 256. A photograph of the SLM as it was mounted for use in the ULI system is included in Fig. 25.



Fig. 25. A photograph of the Hamamatsu spatial light modulator, mounted and positioned within the final beam shaping assisted ULI system.

With correct calibrations, this SLM can allow for a peak phase delay of up to 2π for 1030 nm. The tuning of this delay is what allows for the phase control of the light. The liquid crystal molecules that make up a single pixel of the SLM can have their physical orientation adjusted via a computer-controlled electronic system, where the applied phase delay is related to this orientation. When light passes through these orientation-shifted pixels the light has its phase component changed. With appropriate coding this method can give fine control over the incident light phase, and therefore how the light is shaped. This LCOS array is in front of an aluminium mirror, which sacrifices high power reflection efficiency for broadband reflectivity. When a collimated beam is incident with the active area the wavefront moves through the LCOS layer and is reflected off the aluminium mirror back through the array: upon these interactions a phase change is applied to the beam. Figure 26 shows a cross-section of the SLM's active area, detailing the main components involved in this process.

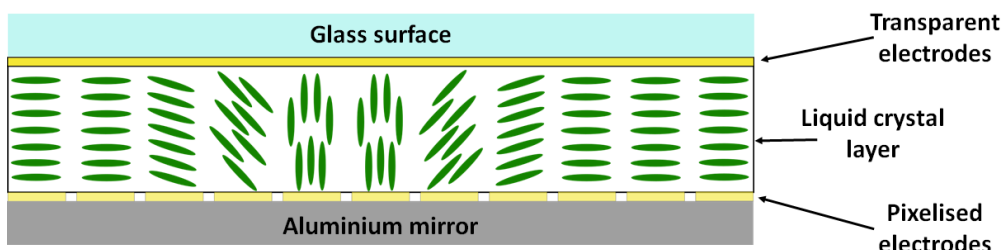


Fig. 26. A schematic cross-section of the active area of a LCOS (liquid crystal on silicon) SLM operation in the reflection mode. Details included are the glass surface, followed by a transparent electrode layer which in tandem with the pixelised electrode layer controls the orientation of the liquid crystal layer. Finally included is the aluminium mirror.

There are many ways to control the LCOS array. For our purposes, rather than use low-level programming, the SLM was coupled to a computer monitor with an identical resolution. When an image was set as the desktop background of the PC - the same image was displayed on the SLM. This means that the desktop background would need to be an image that contains the required phase information which could produce the desired final beam shape. Such phase masks were generated using Python or Matlab. Phase masks could be cycled through by using the translation stage software, enabled by extension script written in C++. The masks themselves were greyscale 8-bit images with 256 grey-levels, whose distribution of pixel depths directly related to the applied phase change of the SLM. An example of the masks used in this project are shown in figure 27, where a) is an example of a flatness correction mask provided with the SLM, b) is a blaze diffraction grating in isolation (covered in detail in Section [3.2.3](#)), and c) is both combined and was used for ULI fabrication using a Gaussian beam. This method of encoding the SLM was highly flexible and required an understanding of Fourier optics to take full advantage of its beam shaping capabilities. Fourier analysis specifically will be a main topic of discussion as this thesis continues.

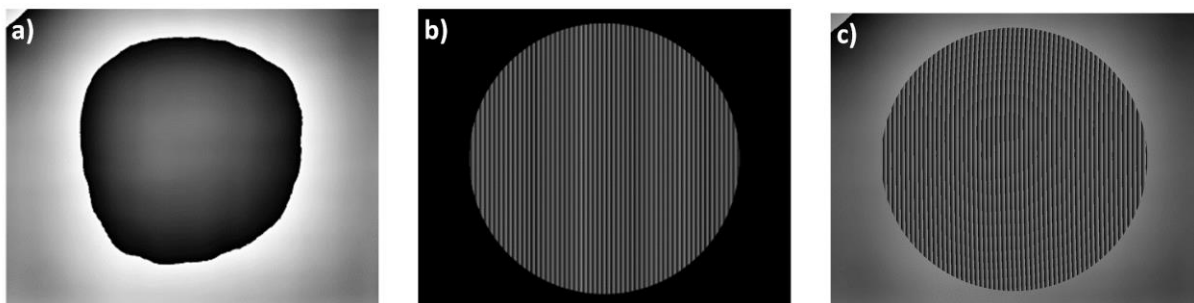


Fig. 27. A set of phase masks used to produce Gaussian beam laser writing with an SLM where: a) is the correction mask packaged with the SLM and calibrated for 1030 nm, b) is a blazed diffraction grating with 16 pixel per line for a density of 6.25 lines per millimetre (L/mm), and c) is the final phase mask of both a) and b) contribution combined.

There were many issues to consider when adding beam shaping to the current standard of ULI system, with one issue related to the SLM itself. The LCOS array does not give 100% efficient phase control, meaning a portion of the incident beam will be reflected off the active area with its phase unaffected. There will of course be further optical power losses due to such things as scatter and absorption. The unmodulated light results in a collection of power in the centre of the shaped beam profile. The 'zeroth' reflection order is suitable for many applications, however, with the goal of not

only producing a ULI system capable of manufacturing the proposed device but a general long-term addition to the system, a more flexible solution was required [74]. The solution that is proposed here is heavily reliant on optical Fourier transforms, which is part of the field of Fourier optics. A basic understanding of this and the related process was key to the successful application of beam shaping in microfabrication.

3.2.3. Fourier optics and filtering

Fourier optics is the mathematical study of light in which a single wavefront is regarded as a combination or superposition of plane waves [75]. In a practical optics environment, a “perfect” thin lens performs a Fourier transform on a propagating wavefront when positioned $1-f$ away from an object. $1-f$ after this lens (from here on called F_1) will be the Fourier transform of the object. This position, $2-f$ away from the object, is called the Fourier plane. In a scenario with an SLM, the active area of this device acts as the object plane and the Fourier plane will contain the Fourier transform of the applied phase mask. For example, if the Fourier transform of a target is projected onto the SLM, this target will then be reproduced at the Fourier plane [76]. The same process takes place when the light propagates through the final objective lens used to focus the light inside the substrate. Therefore, the Fourier transform of an object $1-f$ away from the objective will be formed within the substrate. While an interesting subject, it is relevant here as it is the key to overcoming the limitation of the LCOS array.

To overcome the negative effects of the un-phase shifted zeroth order a method of removing or suppressing it was required. To this end a blazed diffraction grating phase mask applied to the SLM in tandem with a Fourier optics system, added to the ULI system. This ensured the maximum power was distributed into a single diffracted order. The grating period dictated the spatial separation of the diffracted order after the first Fourier transform, in this case, 6.25 L/mm (lines per millimetre) with 16 pixels per line. This spacing allowed for efficient spatial filtering with no overlaps when producing beam profiles with a large area. Along with a varying pixel height from 0 to 2π , a peak diffraction efficiency of $\sim 82\%$ relative to the power incident on the SLM was produced - the highest achievable

with our system. The remaining unwanted orders still require filtering to ensure they do not interfere with the operation of the systems. There is a wide range of different filtering techniques that could have been implemented, however, when using an SLM-based system a Fourier optics filtering system has been shown to be ideal. As shown in Fig 28, when an SLM is placed in the object plane of F_{t1} while a blazed grating is projected onto it, distinct diffraction orders will be generated in the Fourier plane as depicted in Fig. 28 a).

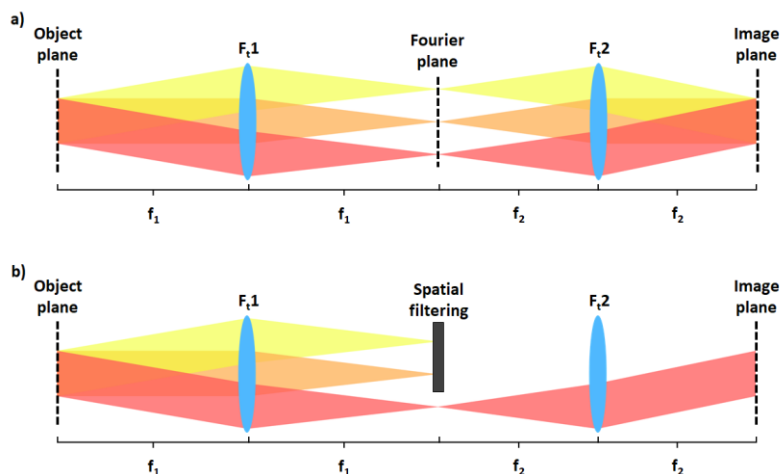


Fig. 28. Pair of diagrams illustrating the Fourier spatial filtering system. a) depicts the system, where light from the object plane is Fourier transformed in the Fourier plane by the Fourier transform lens F_{t1} . The image formed in this plane is a series of distinct orders. The second Fourier transform lens F_{t2} does another transform resulting in a field present in the image plane. b) is the same system but with a spatial filter, demonstrating the effect this would have on the results present on the image plane. The orders of light are separated out into three colours: yellow -1st, orange 0th, and red +1st.

The system of lenses shown in Fig. 28 is, in effect, taking the near-field Fresnel diffraction pattern produced close to the SLM and converting it into the far-field Fraunhofer diffraction pattern, a pattern which forms very far downstream of the initial interference source [77]. This brings the pattern into a position that is both easy to access and easier to spatial filter [78]. This method is both energy-efficient and information efficient, which is important here as the blazed grating will not be the only element projected onto the SLM. At the Fourier plane, each individual diffraction order will also contain the Fourier transform of any other phase mask applied to the SLM. This is where a second Fourier transform lens (F_{t2}) becomes necessary. When F_{t2} is placed one focal length away from the Fourier plane, shown in both Fig. 4 a) and b), a further transform is applied. When no spatial filtering is applied (a) the wavefront in the Fourier plane will be identical to that of the object plane. With spatial filtering (b) the image plane will contain all phase components present on the SLM bar the blazed diffraction

grating. The final beam will then no longer have the power distributed into the centre, maintaining the integrity of the desired beam shaping. When coupled into the final writing objective a final Fourier transform is conducted. The system in its totality (F_{t1} , F_{t2} , and the final writing objective) is a 6-f Fourier system, where three optical Fourier transforms are conducted. Implementing such a technique into a conventional ULI system did come with its own challenges which were covered in Section [3.2.1](#), where optics and optomechanics were selected to ensure idea operation. When this was achieved arbitrary phase masks could then be applied to the SLM allowing for testing of different methods to obtain an elongated focus.

3.2.4. Vortex beam-assisted ultrafast laser inscription

The blazed grating, depicted in plot b) of Figure 27, was one of many different phase components required for beam shaping and combined with the other phase masks – a process made available by the large bit depth and high resolution of the SLM. Along with this grating, there were other necessary phase masks that had to be applied for all inscription runs done on this system. Firstly, a flatness correction mask had to be added. The aluminium mirror which makes up the back surface of the SLM is slightly bowed due to manufacturing imperfections, resulting in aberration. The SLM was supplied with a set of predetermined correction masks for particular wavelengths: in this case the correction mask for 1030 nm was selected. This is depicted in isolation in plot a) of Figure 27. One further phase mask was used to crop the profile of the beam. The addition of this pupil crop allowed for efficient coupling into the back aperture of the final writing of object. This crop was encoded directly onto the blazed grating as depicted in Figure 29.

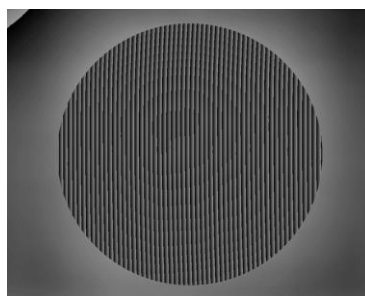


Fig. 29. A digital phase mask containing: the blazed grating, the flatness correction mask packaged with the SLM, and the pupil crop.

Figure 29 shows the final combination of the three phase masks and displays the characteristics of the flatness correction mask, the blazed grating, and the pupil crop. The sum of these masks required phase wrapping to ensure the peak 2π phase delay – as the final phase mask may produce beyond 2π values. The value use to wrap the phase mask was wavelength dependent and scales via an integer number, in this case for 2π phase delay at 1030 nm the integer value was 150. The data was provided by the manufacture alongside the SLMs documentation. The final addition to the SLM for this project was for the generation of beam elongation, by utilising a digital axicon lens.

As was introduced in Section 3.1, beam elongation shaping is commonly performed using an axicon lens, which in turn generates a Bessel beam. A true Bessel beam is a propagating beam which does not experience diffraction when formed with an infinitely large wavefront [79]. However, the physically achievable version is a pseudo-Bessel beam (which will simply be called a Bessel beam in much of the following text) which manifests as a focal point that is elongated along the optical axis. Along with being in effect an elongated focus it has other distinct attributes. Due to the way it is typically generated the wavefront focuses a series of rings extending out from the elongated focus: this contributes to another quality where a Bessel beam can reform if disrupted [80]. As with many beam functions, this can be generated in several ways, but the most relevant to this project is the axicon lens as depicted in Fig. 30 [81].

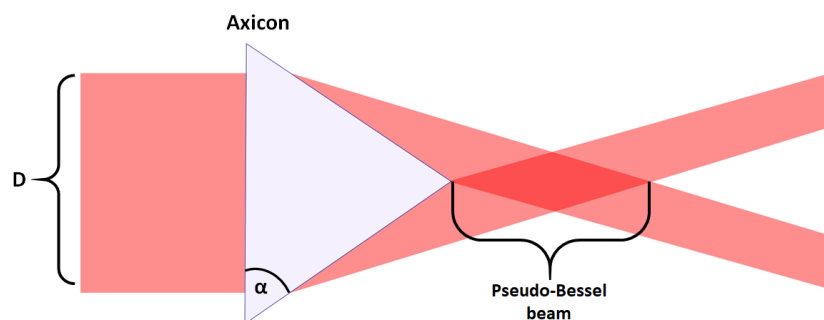


Fig. 30. A diagram of the basic operation of the axicon lens. Detailing: the wavefront diameter D , the axicon gradient α , and the position of the pseudo-Bessel beam.

Figure 30 shows the basic effect of an axicon on a wavefront with diameter D . The conical-shaped axicon lens refracts the propagating wave in such a way that the constructive interference forms an elongated focus called a pseudo-Bessel beam. When this is formed using a Gaussian beam the

produced elongated focus is called a Gaussian-Bessel. The angle α of this axicon dictates the length of the beam elongation as shown in equation (2). In this case the elongation of the beam is reference to as the depth of focus (DOF), and R is the radius of the beam incident upon the axicon (D/2)

$$DOF \approx \frac{R}{(n-1)\alpha} \quad (2)$$

The initial goal of this project was to generate a Bessel beam using the SLM, using a digital facsimile of an axicon. In a Matlab script, a series of digital axicons were generated: this took the form of a series of concentric circles with a gradient of pixel value within each ring, in effect building up a conical lens. The initial conical phase mask for an axicon with a phase angle of 4.27 mrad is depicted in Fig. 31 (a).

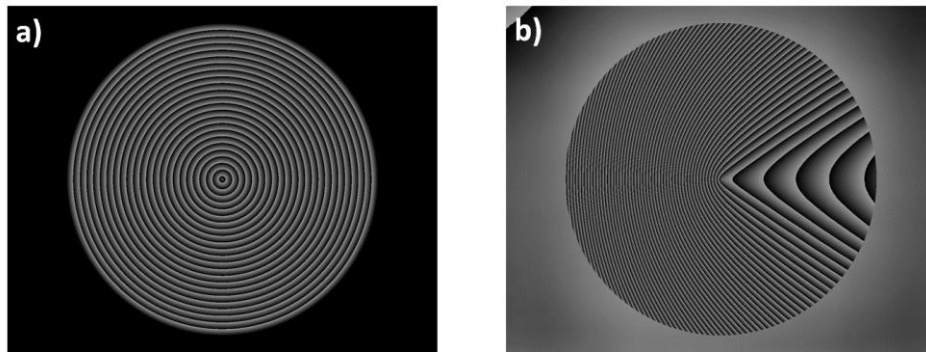


Fig. 31. (a) a phase mask of a digital axicon with a phase gradient of 4.27 mrad. (b) is the final vortex beam phase mask containing the blazed grating, pupil crop, and flatness correction.

The application of such a digital axicon did produce an elongated focal volume, with an axicon phase gradient of 4.27 mrad producing a focal volume extending close to 300 μm along the optical axis. However, upon closer examination it was found that these elongated foci were not pseudo-Bessel beams. It was found that the digital axicon as implemented was generating an optical vortex, an optical field that has a point of zero intensity at the centre. This vortex forms at the Fourier plane because of the digital axicon being in the SLM's object plane, meaning the Gaussian-Bessel beam was formed immediately after the SLM. As the wavefront propagates away from the SLM, it separates out into a series of orders which when focused through F_1 to form the optical vortex, which can be seen as a ring on each diffracted order in the Fourier plane. After spatial filtering the conjugate of the vortex, the vortex focus, is reformed at the back aperture of the writing objective. Therefore, at the focus of the writing objective an optical vortex is formed, which is within the substrate. However, with the large demagnification occurring in the 6-f system, the focus is essentially elongated. This method

of beam elongation scaled in a manner that is inverse to the behaviour expected for a Bessel beam, where an increase in the angle of the digital axicon extends the focal axial length. This implies that when the digital axicon angle is 0° a Gaussian beam is recreated, an advantage as the elongated and standard beam laser writing is often required for device manufacturing. This is reflected in the equation which governs the phase shift applied by a Bessel beam, show in equation (3). Where the change in phase is represented by φ , λ is the wavelength, and R in this case is the semi diameter of the incident beam.

$$\alpha = \frac{\varphi\lambda}{2\pi R} \quad (3)$$

The process from Gaussian-Bessel beam generation to the formation of the optical vortex was simulated by Dr. Calum Ross in the Zemax wavefront simulation software: the results are shown in Fig. 32.

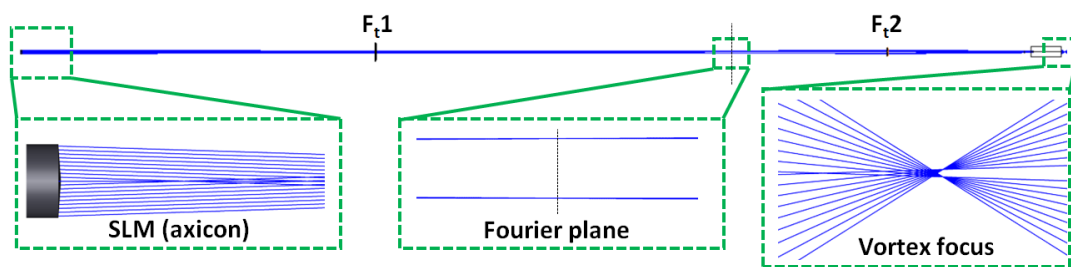


Fig. 32. A Zemax simulation of the optical system spanning from the SLM while displaying the digital axicon to the image plane of the second Fourier transform lens. Highlighted is the wavefront immediately after the SLM, showing the generation of a Gaussian-Bessel beam. Next, the Fourier plane is highlighted which shows the ring-shaped focus formed $1f$ away from the first Fourier transform lens (F_{t1}). Finally, the vortex beams focus is highlighted, formed in the image plane $1f$ away from the second Fourier transform lens (F_{t2}).

The simulation shows the wavefront as it propagates through the first two lenses of the 6-f system. Key sections are highlighted starting with the SLM. What is shown is the Gaussian-Bessel beam generated after the SLM when a digital axicon is applied. After this the Fourier plan is shown - this is after the first Fourier transformer lens (F_{t1}) where a ring-shaped wavefront is generated. Finally, the optical vortex focus is shown. This is formed in the image plane of the second Fourier transform lens (F_{t2}).

When this vortex focus is focused it is from the elongated focal volume as shown in Fig. 33 which shows the cross-section of the inscription focal volume over a series of distances along the

optical axis. This figure shows that as the optical is focused the produced focal volume maintains its size over a distance of 200 μm along the optical axis.

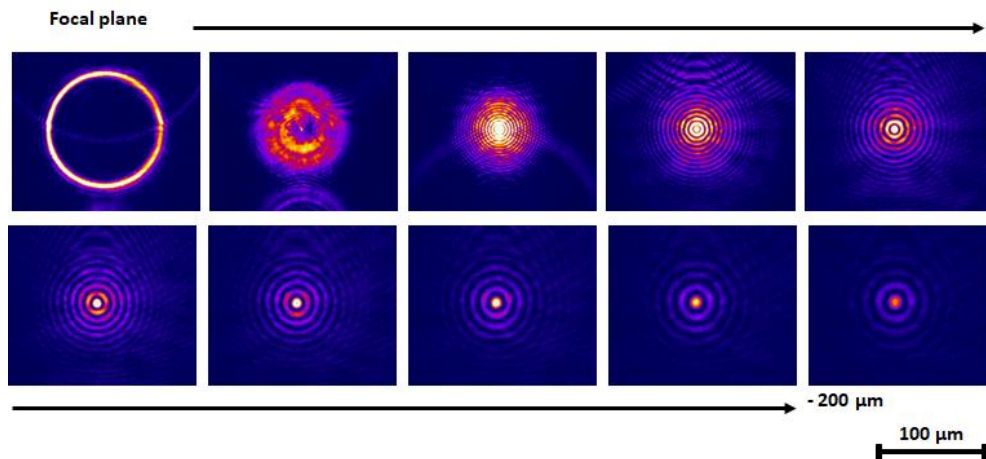


Fig. 33. A series of photographs of the focal volume along the optical axis. What is shown is that as the ring wavefront is focused the final axial volume is maintained over a distance of 200 μm . The distance between each image is 20 μm , with the image plane moving towards the writing objective.

While this form of beam elongation was not the expected result it did prove to be beneficial. With further study, it was found that using a true pseudo-Bessel beam (generated either with a digital or physical axicon) would require a radically different writing system. To incorporate this form of beam shaping, the Fourier plane would need to be one focal length before the writing objective. This would present a further challenge when applying the other, non-axicon, phase masks: in particular with the translation stage spatial filtering would prove difficult. If the project demanded it, two optical systems could have been coupled into the same writing objective, which would then require a method of switching between each line during a run for both forms of inscription and the manual removal of components. This would add now unnecessary complexity and further area instabilities into the system. However, with the use of Vortex beams, these issues can be circumvented – with a system capable of a range of beam shaping applications as well as traditional unshaped laser inscription.

Once the optical setup of the SLM-enabled ULI system was finalized a detailed study of these vortex beams was conducted. The main goal of this was to increase the focal region's axial length such that fewer written tracks were required to produce a complete surface that could be chemically etched. A range of parameters were tested, including pulse energy, repetition-rate, translation velocity, and digital axicon angle, to strike a balance between the elongation while maintaining a

consistent etching selectivity. In tandem with this, pulse duration and polarization were also studied, not only to test the effects on the etch rate but to also find at what pulse duration the selectivity become polarisation independent. A ULI process that requires little in the way of polarisation control for curved surfaces would prove beneficial.

In the investigation vortex phase masks were generated to produce a peak phase shift of 0, 37.5, 75, 112.5, and 150 radians. This corresponded to the conical phase-based angles of 0, 1.07, 2.13, 3.20, 4.27 mrad for a semi diameter of 5.76 mm. Again, it is important to note that when applying the 0 mrad phase mask the beam will inscribe as a Gaussian beam. This can be seen in micrographs (a) and (b) in figure 34. Where (a) shows the generation of an electron plasma while using a Gaussian beam, while (b) shows the elongation of the electron plasma when a 3.20 radian vortex beam was applied. Further depicted in figure 34 are micrograph images of a selection of etched channels. These shows that position of the area modification forms prior the nominal focal plane, due to the overlapping waves as they propagate to form the optical vortex. These micrographs also further show that the thickness of the channel is dictated by the pulse energy – not the conical phase-based angle.

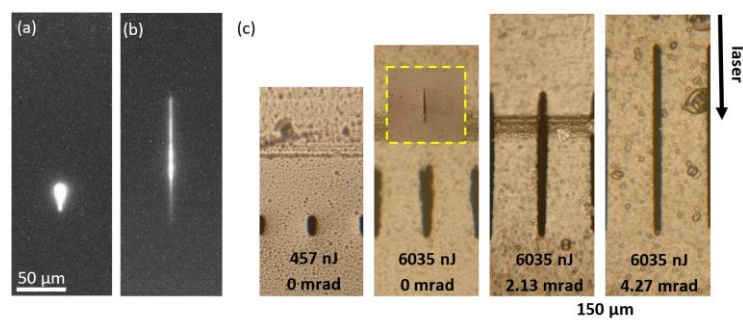


Fig. 34. (a) and (b) are micrographs of partial free-electron plasma emission from the focal region inside fused silica under irradiation with a Gaussian and vortex focus (generated by imparting a 3.20 mrad conical phase front) respectively. (c) is a series of micrographs showing etched channel facets written with a range of pulse energies and conical phase masks to highlight the DOF elongation. The repetition rate was 50 kHz, polarisation was circular, translation speed was 4 mm/s and the pulse duration was 1440 fs when writing the channels shown. Inset: A corresponding channel cross-section prior to etching (at same scale).

These channels were all written at a nominal depth of 500 μm for a pulse duration range of 500 nJ to 2250 nJ for all conical phase front bar 0 mrad which was capped at 350 nJ to prevent the influence of filamentation. Figure 34 only shows a subset of the written sample while the data from the first phase of investigate is show in figure 35.

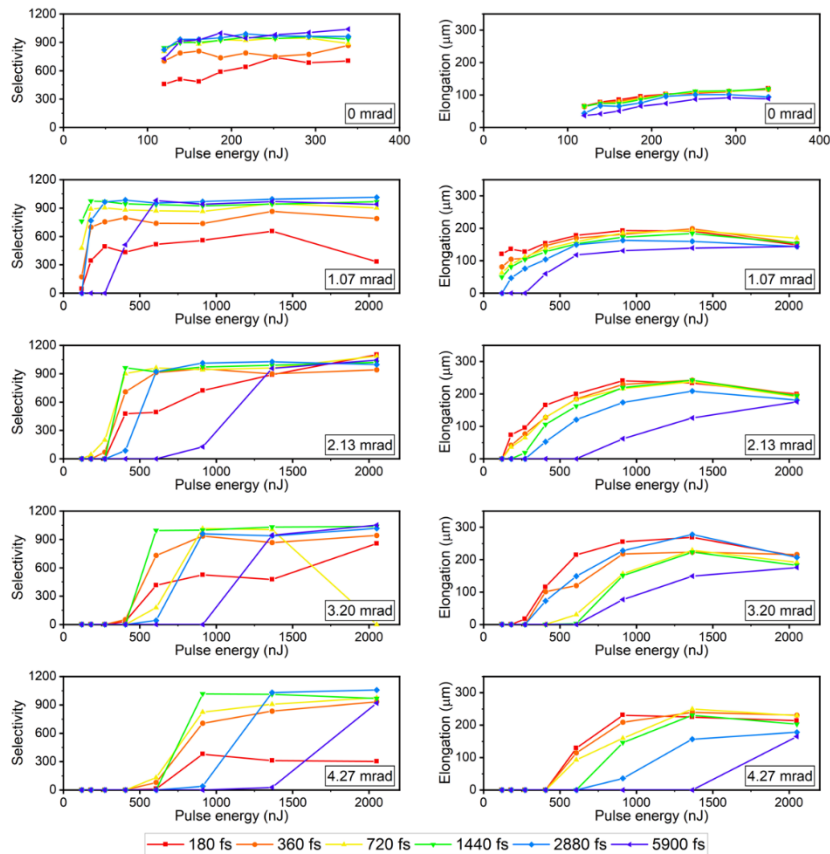


Fig. 35. Line graphs displaying etching selectivity (left) and DOF (right) for several SLM generated conical phase masks for varying pulse energy and pulse duration. In each case, the laser polarisation was circular and the translation speed was 4 mm/s. The uncertainty in the selectivity is approximately 5.2%.

This data set shows the etch rate and DOF (or beam elongation) vs pulse energy for each tested conical wavefront at a range of pulse durations. The selected pulse durations being 180, 360, 770, 1440, 2880, and 5900 fs. Beyond demonstration further the ability of vortex beam to elongate the beam it also showed that the etching selectivity was higher for longer pulse durations. As all channel were written with the same polarization, circular, this implies selectivity became polarisation insensitive at longer pulse durations. The data does show an increase beam elongation for increased conical phase front however the pulse energy did need to be increased to facilitating the increase in modified area. The results also show that an increase in pulse energy can increase the modified volume for the Gaussian case. This method may also incur filamentation at high pulse energy which could also further increase the elongation. Pulse duration was also shown to affect the beam elongation, where the pulse durations 2880 fs and 5900 fs show a drop in the elongation. This is suspected to be due to the reduction in the peak intensity within the focus, reducing the modified area.

Following these results, a second investigation was conducted, this time included translation speed. Translation speed is an important variable as it dictates the overlap between pulses. The speeds selected were 1 to 8 mm/s, which corresponds to an overlap of 75 to 10 pulses, with the same pulse energy range as the previous investigation. A further change to this investigation was the pulse duration range. It had been shown that 720 and 1440 fs was the minimum needed to produce the optimal selective etching at 4 mm/s and such a further number of pulse duration were test: 1080, 1440, 2160, 2880, 4390, and 5900 fs. To narrow the focus onto the effect of translation velocity and pulse duration the vortex beam phase mask was fixed at a gradient of 3.20 mrad. The results are depicted in a similar fashion as before in figure 36.

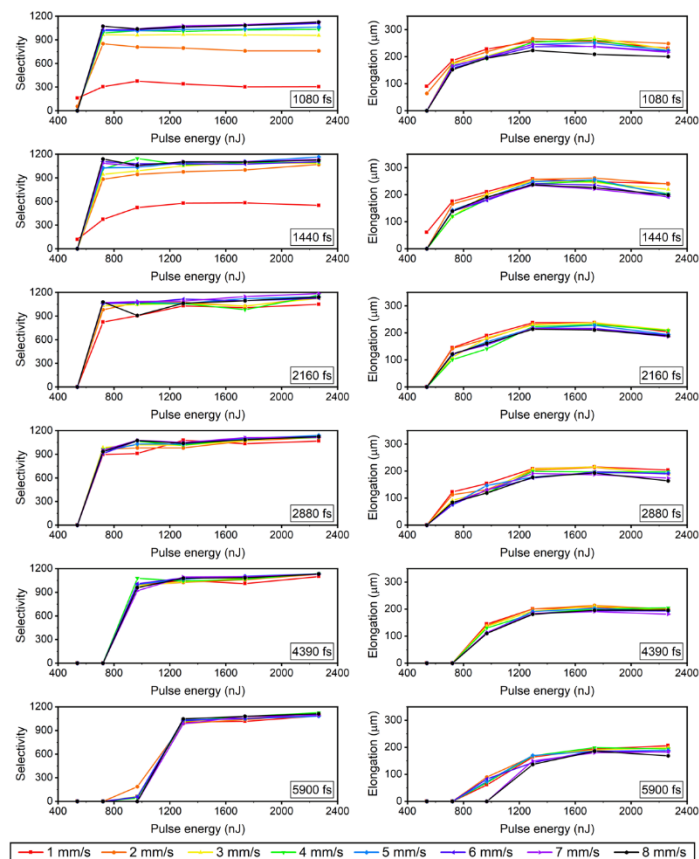


Fig. 36. Line graphs displaying etching selectivity (left) and DOF (right) for several pulse durations with varying pulse energy and writing speed. In this case, the laser polarisation was circular and the axicon base-angle was fixed at 3.20 mrad. The uncertainty in the selectivity is approximately 5.2%.

It was observed that translation speed only had a significant effect on etching rate for 1080 fs and 1440 fs, while the effective beam elongation decreased with increased pulse durations. The result do suggest that for the longest beam elongation while maintaining selective etching pulse durations

between 1080 and 1440 fs at a translation speed above 3 mm/s are require. However, if translation speed is limited longer pulse duration can compensate for that limitation.

With the parameter space narrowed a final set of parameters was investigated. This final studied covered a wide range of differing repetition rates, pulse energies, translation speed, and again over the range of vortex phase masks. The one laser parameter kept constant in this case was the pulse duration which was set to 1440 fs due to the high performance of polarisation incentive etching and DOF elongation it had shown up to this point. The results are depicted in the heat map in Fig. 37.

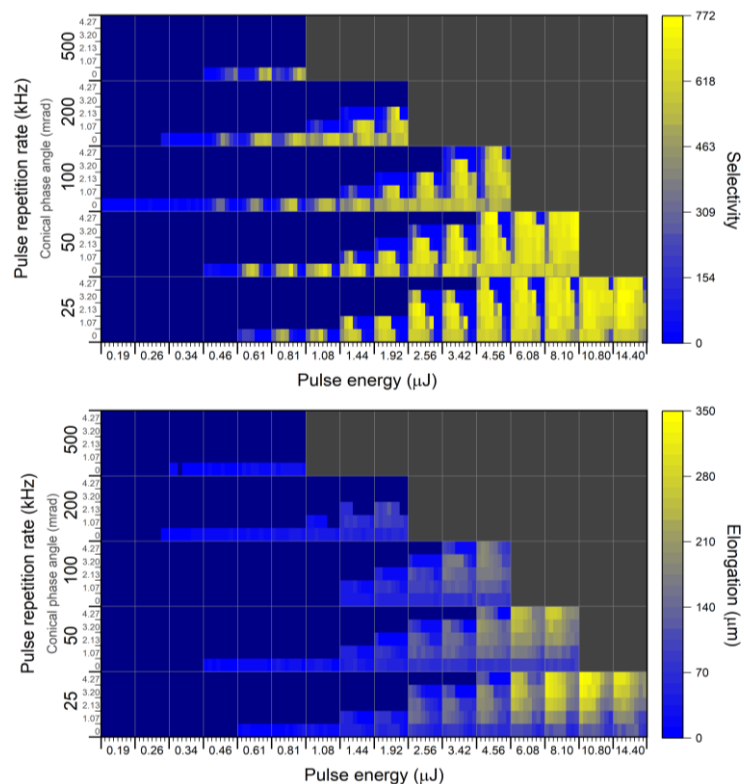


Fig. 37. Heat maps displaying the results of the final parameter space investigation. The selectivity (top) and DOF (bottom) were measured for channels written with several pulse energies, writing speeds, conical phase base-angles and pulse repetition rates. The minor tick marks along the pulse energy axis represent doubling sample translation speeds from 1 to 128 mm/s, while the minor tick marks along the repetition rate axis denote base-angles from 0 to 4.27 mrad. Circularly polarised light was used throughout. The uncertainty in the selectivity is approximately 5.2%.

Each heat map represents the effect the same parameter space had on first selectivity and secondly beam elongation. The y-axis on both maps shows the pulse energy where each energy is separated into eight divisions representing a different translation speed. For this investigation a different range of translation speed was selected, going to a much larger final value. These speeds were: 1, 2, 4, 8, 16, 32, 128 mm/s – going below and well above the 3 mm/s minimum limit highlighted by the previous investigation.

These results are detailed but breaking them down they give a good indication of how parameters selection should be done going forward – maximizing the desired outcome of the material modification. First the data shows that the pulse energy threshold for modification increases as the conical base angle of the vortex phase mask increases. The etching rate is negatively affected by slow translation speeds, which produced a low focal volume overlap. This was the inverse for the effective beam elongation, where slower translation speeds increased the total DOF. Also observable in the result was that an increase in repetition rate for like pulse energies increased the optimal translation speed. This could be advantageous in a mass manufacturing environment where increasing the writing laser repetition rate can allow for the increase in manufacturing speed, however it would require the selection of a spatial light modulator with a sufficiently higher average power limit to take full advantage of this.

One final interesting observation for the data supports a previous assertion. While using the 0 mrad vortex phase mask the elongation was increased by increasing the pulse energy. This was mostly due to filamentation via Kerr-focusing and did not produce beam elongation close to maximum measured using higher conical base angle vertex beam phase mask.

The outcome of study was a demonstration of this beam elongation technique in the inscription of a series of geometric shapes. These examples were done with both a traditional Gaussian beam and then the 4.27 mrad conical base angle vortex beam. The initial testing was on finding the maximum layer separations for the raster scan which built up the surface. Figure 38 (a) and (b) show micrographs of these tests. Testing was done in 2 mm thick fused silica samples which were then chemically etched in 8M KOH at 85°C for 2 hours. It was found that for the Gaussian example had maximum a layer separation of 16 μm . This was more than the 4.4 μm theoretical limit for the 0.6 NA writing objective, meaning some form of filamentation was present. When using a vortex beam a layer spacing of 200 μm was found to be acceptable, a significant increase when compared to the Gaussian written surfaces. With these values set a series of shape were written. The geometric shapes were a star, circle, and triangle, within a greater ellipse. These were writing in a 10 x 10 x 1 mm substrate and

are depicted before selective chemical etching in figure 38 (c). With a writing speed for both Gaussian and Vortex beam set to 4 mm/s. It was demonstrated that for the Gaussian case the sample took 15 minutes to complete, while using a vortex beam this took just 72 seconds. This was a 12-fold reduction in the manufacturing time which did require an increase in the writing pulse energy from 1620 nJ for the Gaussian case to 8100 nJ for the vortex beam.

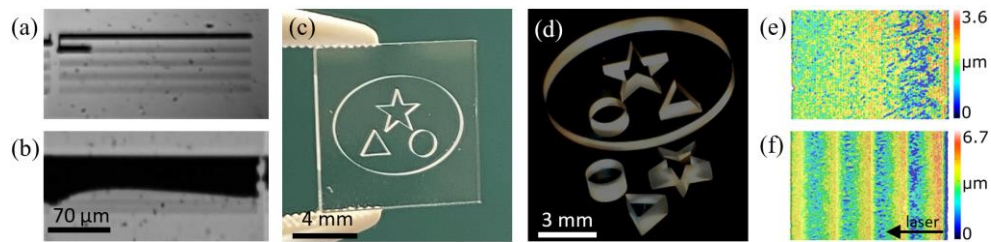


Fig. 38. (a) and (b) show chemically etched tracks written with a vortex beam to determine the maximum z-spacing for continuous modification through silica glass. The surfaces were formed by raster scanning 2 mm long tracks in 2 mm thick glass. Note the micrographs were taken with the surfaces tilted. (c) shows a star, triangle and circle within an ellipse, each inscribed into a 1 mm thick fused silica substrate. The separated components, written with a vortex beam in 72 s, and subsequently etched for two hours, are shown in (d). (e) and (f) are surface profiles of the 1 mm thick etched surfaces inscribed with a Gaussian and vortex focus respectively.

Both beam examples was chemically etched for 2 hours with the post etch sample shown in figure 38 (d). Also included are roughness measurements of the Gaussian and vortex beam examples in (c) and (f) respectively. Both roughness's were significant, with the Gaussian case measuring 336 nm mean roughness. Also observable with the Gaussian case was a depth dependency. The vortex beam also yielded interesting results showing a surface roughness of 460 nm with a periodic variance due to the non-uniform energy distribution present in the vortex beam shaped focal volume. Going forward more work would be required to find the best method of mitigating this roughness. This could include limiting the pulse energy or doing post-etching grinding and polishing on the surface.

This study not only resulted in a publication but also provided a strong foundation of knowledge for later projects. It not only progressing the work on the proposed microspectrometer device but also contributed to the body of knowledge of ultrafast laser writing as a field.

3.3. Author contributions

The majority of the lab work was conducted by myself with Dr. Calum Ross acting as the primary RA. His role was to provide advice and support for the initial implementation of the SLM into the ULI

system, as well as contributing several simulations and the final set of etched objects for the final publication. Mr. Jacopo Siliprandi worked closely with the SLM and this project at the beginning and was instrumental in gaining a deeper understanding of the SLM device. He later contributed significantly to the proceeding publication on beam shaping for aberration compensation. Professor Robert Thomson was the principal investigator offering advice on the project and providing the final feedback on the publication. Professor Thomson was also instrumental in the concept and design of the microspectrometer device.

3.4. Review and future studies

The work outlined in the publication included in it entirely in the appendix enabled a impressive 12-fold decrease in ULI manufacturing times. As such, it is clear that the use of vortex beams was successful in addressing the long manufacturing times encountered during some ULI applications. The results presented here lay a strong foundation for further application of this beam-elongating process in both this and other ULI projects. Progress has been made in this regard. Dr. Ross presented at CLEO 2022, a method of ULI manufacturing optical fibre using this very process [82]. His presentation showed the manufacturing of 6 mm thick disks of fused silica, which were stacked, and laser welded together. Once welded the preform was extruded using an optical fibre pulling tower. Without a beam elongated to 200 μm the inscription time of a single disk was reduced by over an order of magnitude and enabled the inscription of 50 disks required for a single preform, which would otherwise be impractical. This was a good demonstration of the beam elongation technique and provided much-needed background for further studies. Shortly after this success, the first microspectrometer was fabricated. This made use of the vortex beam elongation process. The success and failure of its development will be covered in detail in Chapter [5](#).

3.5. Conclusion

The goal of this study was to produce a method of decreasing the manufacture time of ultrafast inscribed optical devices. Large manufacturing times can result in a decrease in the quality of the

optical device as well as reduced applicability of this manufacturing method for industrial use. The first step was the introduction of a phase controlling spatial light modulator, which when coupled with a 6-f Fourier spatial filtering system allowed for near arbitrary beam shaping. On to this SLM a digital axicon was projected. This resulted in the formation of an optical vortex at the Fourier plane of the 6-f system: when this vortex was focused through a writing objective an elongated focus was achieved. Through the application of a digital axicon with a phase gradient of 4.27 mrad focal extension of $\sim 300 \mu\text{m}$ was achieved. Results showed that even with the elongation etching selectivity remained high and practical demonstrations showed a 12-fold decrease in manufacturing time. These results showed promise in the introduction for this method for a range of different ULI applications including the proposed microspectrometer device.

4. SLM-assisted aberration compensation during ULI

4.1. Introduction

4.1.1. Ultrafast laser microfabrication at depth

Chapter 3 introduced the use of an SLM for focus elongation as a method to decrease ULI manufacturing time, achieved via increasing the volume of the modified material. Beyond decreasing the manufacturing time, modifying larger volumes of the material may allow for larger, close to macro-scale, objects and structures to be inscribed. However, when trying to inscribe deeper into large substrates, certain limitations come into play which would limit the size of manufactured devices. When focusing light into a transparent material, the focal volume will not match that formed in a vacuum due to aberration imparted on the beam.

As an optical wavefront passes through an interface between two regions of differing refractive index, the wavefront is modulated through refraction [83]. In the simplest case, the ratio of the incident angle and refracted angle on a flat surface is related to the ratio of the two refractive indices. In more complex situations, a curved interface can be used to form a lens, which can focus a wavefront to point at some distance from the lens. By precisely designing the shape of the interface and selecting the appropriate transparent substrate the desired focal characteristics of a lens can be achieved. If a wavefront were to be focused into the volume of a substrate - refraction would distort the lens' focus. Figure 39 is a schematic of such a process showing a) a lens that focuses the light to a focal point, and b) where the lens results in an aberrated focal volume.

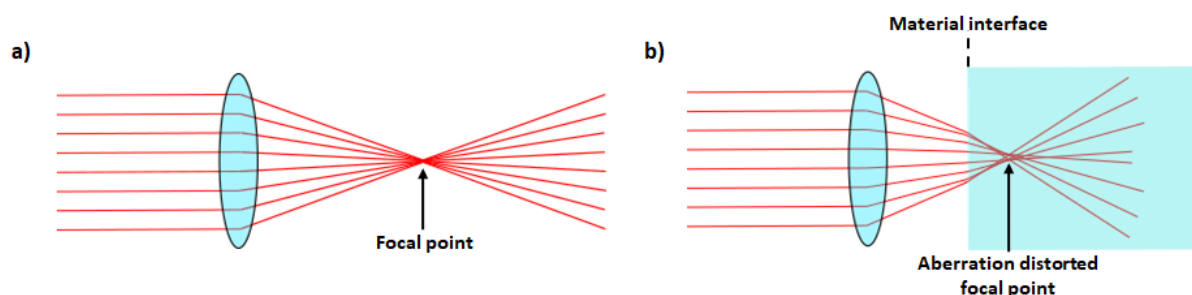


Fig. 39. A schematic of two biconvex lenses where – a) produces a focal volume and b) results in a focal point that is distorted due to the material interface.

Lenses can be designed such that they compensate for aberration although this is limited to a single point within the material. This is an important effect to take note of when manufacturing using ULI because when the focal volume is distorted the material modification is negatively affected.

The form the substrate-induced aberration takes can be varied depending upon the type of substrate and writing objective: for a case such as ULI the aberration will be non-chromatic in nature due to the narrow bandwidth of the laser source. The aberration present during ULI will be called the 'substrate aberration' and it is a combination of individual forms of aberration all combining to distort the focal volume. One example is the effect of numerical aperture (NA). Often high NA objectives will be used because of the high resolution they provide, however, a large NA results in a more diverging beam and therefore the focus becomes more susceptible to spherical aberration. This is further complicated when attempting to focus deeper into a transparent medium. When the material depth increases, the aberration contribution will also increase. A distorted focal volume will then reduce the generation of electron plasma and there reduce the quality of the modified material. A schematic of how the aberration scales with depth during the ULI process is shown schematically in Fig. 40.

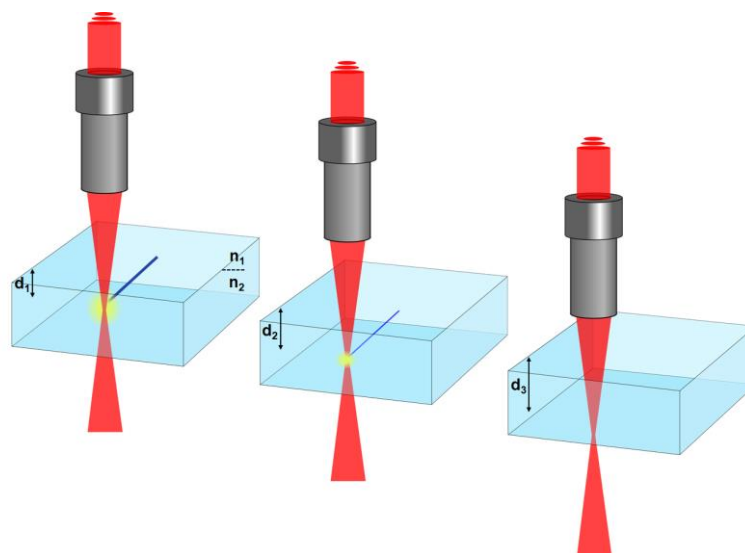


Fig. 40. A writing objective focusing a laser source into a transparent medium. This shows that as the depth of the focus inside the substrates increases from d_1 to d_2 to d_3 the plasma generation depicted in yellow decreases. The material is denoted as index n_2 , while air is denoted as index n_1 .

The figure shows that when inscribing at greater depth within a dielectric substrate the distortion of the focus directly affects the plasma. At extreme depths, there will be no material modification present. The reduction or absence of material modification is due to the distribution of the pulse

energy change such that the nonlinear absorption process is negatively impacted. As stated, in extreme depths this effect can result in no material modification; however, at shallower writing depth or where weak aberration is present, the extent of refractive index change can be reduced, affecting both the quality of pure index change guiding structure, and the rate of selective chemical etching. These side effects have a particularly negative effect on ULI-fabricated VBGs, both in general and more specifically when they would be applied to the proposed spectrometer device.

VBGs, or volume Bragg gratings, are diffraction devices first covered in Chapter 1 of this thesis but are particularly relevant to this chapter. These gratings have both a periodic surface structure and thickness all contributing to the diffraction and Bragg characteristics [84]. The tunability of these grating allow them to act as efficient Bragg filters which can discriminate wavelengths through the diffraction of a transmitted source or the reflection of certain wavelength, depending upon the orientation. Fig. 41 shows a schematic diagram of a VBG orientated in the transmission, where the periodic structure is present on one axis and spans some distance perpendicular to that axis.

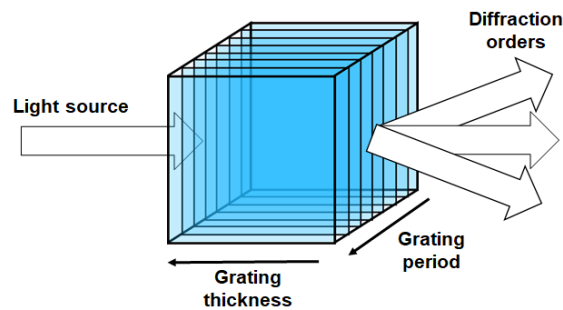


Fig. 41. A volume Bragg grating: depicting the period structure axis marked as grating period and the distance the structure spans along the axis marked as grating thickness. Also depicted is an input light source and the subsequent diffraction orders, demonstrating the primary orientation the VBG operates in this case.

Also shown in Fig. 41 is the direction of an input light source and resulting diffraction orders. This is how VBGs are employed in the proposed spectrometer device, but they can also be used in other configurations depending on the desired application. The thickness of this grating gives a further dimension to tune the desired grating response including diffraction efficiency and bandwidth. The Bragg condition of the transmission form of this grating is typically given as the equation (4).

$$\lambda_B = 2n_0\Lambda \cos(\theta) \quad (4)$$

Where λ_B is the wavelength at the Bragg condition, n_o is the refractive index of the material, Λ is the grating period, and θ is the angle of incidence. Typically, when designing a VBG for a particular wavelength it is the grating period, Λ , which has the greatest impact. These gratings are common in a wide range of applications, in particular metrology and astronomy. For example, an astronomical instrument has recently been proposed that involves the stacking of different volume Bragg gratings, combining their characteristics to separate and diffract different wavelengths simultaneously [85]. This design is potentially an ideal application for ULI manufacturing, however, the axial stacking of VBGs will encounter aberration deeper into a substrate. This is a problem many forms of VBGs will encounter, even in the proposed spectrometer device.

VBG manufacturing can be performed in a range of ways, but ULI is particularly well-suited because it allows the device to be embedded into the substrate and constructed layer-by-layer [43]. Structures with the periodicity of the desired VBG require stacking with a separation sufficiently close to ensure a consistent material modification is achieved. The periodicity or the grating period is strongly related to the dimension of the modified region of material which is related to the chosen writing objective and the writing wavelength. An example of this process is depicted in Fig. 42 [44].

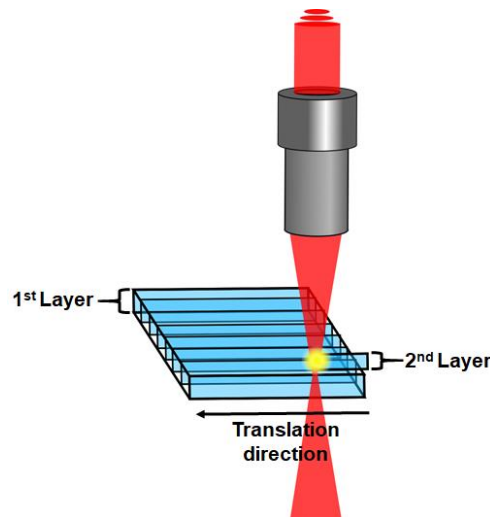


Fig. 42. A depiction of the process of manufacturing a volume Bragg grating. Shown is the direction of the writing beam relative to the grating. The translation direction is depicted along with the completed first layer, and the second layer.

As Fig. 42 shows, the first layer is inscribed the deepest into the material with each subsequent layer being written 'above' the other. This means the final surface is written at a shallower depth within the material meaning it is less likely to be significantly affected by the substrate aberration. A grating made

from a few layers at a relatively shallow depth in a substrate can be manufactured with no measurable degradation to the expected diffraction characteristics. However, for a VBG spanning many layers or written at greater depths, the far surface (the layer deepest within the material) of the VBG may have a drastically different extent of modification. In extreme cases this may result in the layer failing to inscribe properly. The result will be a VBG with a gradient of refractive index change over the gratings' thickness, or in extreme cases, a thickness different to that encoded in the writing system due to uninscribed layers. When speaking on spherical aberration in particular the aberration can be expressed as an extension in the longitudinal focus, given by equation (5). Where LA is the focal elongation, f_d is the focusing depth within a material, n is the refractive index of the material, and NA is the numerical aperture of the writing objective [86].

$$LA = \frac{f_d}{n} \left(\sqrt{\frac{n^2 - NA^2}{1 - NA^2}} - 1 \right) \quad (5)$$

In the case of inscribing in fused silica at 500 μm and 900 μm the elongation would, approximately, be on the scale of $\sim 250 \mu\text{m}$ and $\sim 450 \mu\text{m}$ respectively. To overcome this challenge a method of aberration compensation that could be applied during the ULI process for an arbitrary set of depths needed to be developed [87].

With the SLM already implemented into the ULI system there was immediate scope for the addition of such an aberration correction. The goal of this phase of the project was the selection of a correction method, then testing and developing the techniques as required. The result was a publication in *Optical Materials Express*, detailing the successes of this project [88].

4.1.2. SLM-assisted Zernike polynomial generation

With the end goal to compensate for aberration, the form and extent of this aberration first needs to be quantified. These forms can be variable, depending on what substrate is being focused into and with what writing object and laser source; however, many of these are higher-order aberrations, contributing only a small amount to the true aberration. A monochromatic light source such as the one being used here can have aberration of the form of astigmatic, coma, trefoil, quadrafoil, and so on, but it was decided early on that the primary aberration contribution was spherical in nature [89].

This decision was made based of the state of the experimental set-up and the choice of writing objective. With the alignment of the writing objective and the sample being static and repeatable the chance of off-axis aberration such as coma was significantly reduced. The objective itself was also designed to reduce astigmatic and spherical aberration within a vacuum. When focusing within a material these aberration source will become more significant but, with the machined and polished surface astigmatism is most like to be of a lower significant when compared to spherical. We are also focusing solely on correcting fundamental orders of aberration, with higher order not being taken to account in this case. Spherical aberration is common with lenses, mirrors, and writing objectives, which due to their curvature can cause the outer section of the wavefront to be focused away from the desired focal point.

To compensate for the spherical aberration a phase mask that can reverse these aberration effects at a specific depth needed to be generated and applied to the SLM. For our purposes, Zernike polynomials were selected as the basis for this correction [90]. Zernike polynomials are a set of orthogonal polynomials which represents the deviation from a flat unit circle [91]. Their orthogonal nature means there is no overlap between each individual polynomial, and as a result they can be added or subtracted from each other without repetition of values. These polynomials have a wide range of uses in the field of optics, but in particular optometry, where they are used to mark specific forms and magnitude of aberration [92]. They contain radial and azimuthal components which are used to denote forms of aberration including: astigmatism, defocus, coma, but most importantly spherical. The general equation is depicted in equation (6) where R_n^m represent the radial polynomial, ρ is the radial distance, φ is the azimuthal angle, and m and n are integer values.

$$Z_n^{\pm m} = R_n^m(\rho) \cos(m\varphi) \quad (6)$$

The Z_4^0 Zernike polynomial depicts the phase / spatial deviation of radial and azimuthal components associated with spherical aberration [93]. This polynomial has the radial component shown in equation (7).

$$R_4^0 = 6\rho^4 - 6\rho^2 + 1 \quad (7)$$

As a phase mask, this contained all the information necessary to compensate for the aberration in the focus, however, the singular polynomial is not enough. For a comprehensive correction method, a way of scaling the amount of correction applied based on the inscription depth was also needed. To this end the spherical aberration polynomial was scaled via a Zernike expansion coefficient, also called the aberration coefficient. This magnitude factor took the form of a negative integer value which was applied to the normalised version of the spherical aberration Zernike polynomial, and increased or decreased the contribution of phase change that was being applied. This is illustrated in Fig. 43 which shows the Z_4^0 polynomial in grey scale as well as the multiplication of the aberration coefficient X .

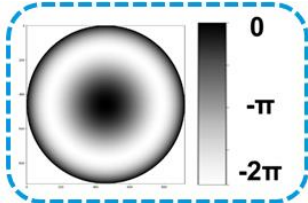
$$X * Z_4^0 = Z(X)$$


Fig. 43. Depiction of the normalized Z_4^0 polynomial in greyscale, alongside the equation showing the polynomial the expansion coefficient X , and the final notation used.

When the polynomial is scaled as required and added to the required blazed grating phase masks, as detailed Chapter 3, the phase mask is denoted as $Z(X)$, where X is the aberration coefficient. When the coefficient X is 0, it means no spherical aberration compensation is applied. Inscribing with this phase mask, $Z(0)$, results in Gaussian beam focal volume without any wavefront shaping. Fabrication using this beam produced a reference value to compare the success of the aberration compensation. A different range of X coefficient were tested throughout this project, these were: 0, -3.0, -3.5, -4.0, -4.5, -5.0, -6.0, and -7.0. Investigations where each of these values were tested will highlighted as they become relevant. When the base Zernike polynomial was multiplied by one the coefficient it went beyond the 256 bit-depth limit of the SLM, however this was already compensated for when the final phase mask was phase wrapped. When the necessary elements of the phase masks are combined before they can be projected on to the phase mask, they must first be numerically wrapped, then phase wrapped. The former means the totality of the image does not go beyond 256-bit depth. While the later ensures that the final phase contribution the desired phase delay - 2π for the maximum bit value.

Once they were generated, the different magnitude phase masks required testing to gauge the success of the correction and understand the effects different magnitudes had on the writing fidelity. To test the effectiveness of Zernike polynomial-based aberration compensation via an SLM a test structure had to be selected. For the reason detailed earlier a VBG was an ideal candidate. They are not only a vital component in the proposed micro-spectrometer, but they can be easily characterised – giving an indication of how successful the compensation was. The first experimental section focuses purely on the development of a VBG suitable for aberration testing.

4.1.3. Preliminary volume Bragg grating studies

Research has shown that VBGs fabricated with ULI can exhibit diffraction efficiencies of ~90% for a 633 nm beam [94]. Whilst an impressive result, such an efficient grating was not required for this study. This study required a VBG sufficiently efficient to get a measurable change in diffraction efficiency between two VBGs written at different depths. A set of parameters for a reference VBG was therefore necessary. As depicted in Fig. 42, the VBGs were inscribed layer-by-layer, where the main parameters that are of concern are the pulse energy, grating period, grating thickness, and grating separation. These parameters dictate the diffraction characteristics of the VBG.

To study these gratings two different laser sources were used – the first and primary source was a simple 633 nm HeNe laser. This was selected for several reasons. First, it is a common and readily available source and emits light in the visible spectrum – the main spectrum that the proposed spectrometer device will be operating with. The focus on calibrating the gratings on a single wavelength did make the following experiments more straightforward; however, for both completeness and to ensure the VBG is well tuned for 633 nm, a wavelength study was also conducted. This was done via a supercontinuum source where select gratings were tested with a range of different wavelengths. The wavelengths tested ranged from 500 nm to 633 nm, and 700 nm to 1100 nm, in steps of 100 nm. These discrete wavelengths were achieved via a set of 10 nm bandwidth line-pass filters.

The 633 nm efficiency study was conducted for each individual VBG, which were written in sets on one or more 1 mm thick fused silica samples. A schematic and photograph of the characterisation setup is depicted in Fig. 44, as is it including in the final publication.

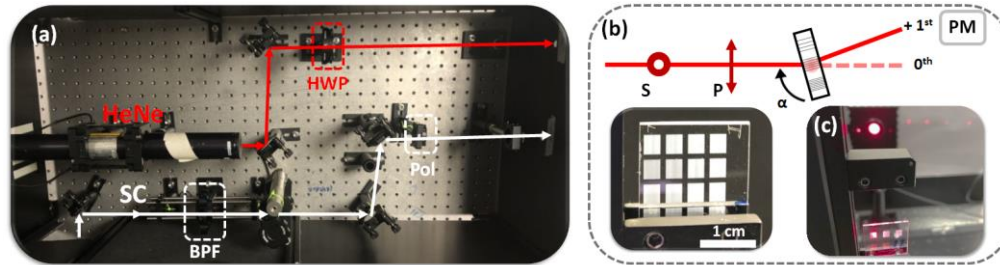


Fig. 44. (a) Annotated digital photograph of characterization set-up, showing the HeNe beam path (red arrows), and the SC beam path (white arrows). The beam paths are followed by a half-wave plate (HWP) and polarizer (Pol) for the HeNe and SC respectively. The bandpass filters (BPF, FKB-VIS-10, Thorlabs) in a rotating turret is depicted on the SC line. (b) Schematic of the grating showing the grating rotation axis, the first and the zeroth orders and the position of the power meter (PM). The two polarisation states P (p-polarization) and S (s-polarization) are also depicted. This is pictured with: (c) a digital photograph of a sample in the foreground, and the integrating sphere and a diffraction pattern in the background.

Image (a) in Figure 44 shows the beams path of the two sources used to test each grating, the 633 nm HeNe and the broadband supercontinuum source (SC). The polarization for each source was controlled via a half-wave plate (HWP) for the HeNe source and polariser for the SC. This allowed for the selection of two polarisation states to perform tests with. For our purposes, P-polarisation was defined as the polarisation when light aligned perpendicular to the direction of the gratings' periodic structure, and S-polarisation was defined as when the light was polarised parallel to them. The polarisation states are detailed in plot (b) along with a schematic of the VBG containing sample. The samples were mounted onto a system with rotation, x-, y-, and z-axis translation. The latter was used to centre the beam on the surface of the VBG while the former was used control the angle at which the laser beam interacts with the VBG. Adjusting the angle was used to maximise the power into the positive first-order diffraction point, similar to a blazed grating. This 'blaze angle' was maximised for each VBG regardless of whether this angle was different, thus ensuring the 'ideal' performance of the grating was captured. This power of the first-order diffraction spot was compared to the power of the laser beam after passing through pristine (unmodified) substrate. Thus, the evaluated efficiency considered the losses associated with reflection and absorption losses in the substrate material. The diffraction efficiency evaluated in this manner is thus referred to as 'relative diffraction efficiency'. This procedure

was conducted for both light sources and over both P- and S-polarisation states. depicted with this is an example of a mounted VBG sample, note the cloudiness of the VBG suggesting some degree of glass modification beyond Type I [95].

The work conducted on finding a set of parameters was not detailed in the final publication reproduced at the end of this chapter. These studies involved the development of a reference VBG at a shallow depth including VBG thickness and writing pulse energies. Many parameters were decided upon early in the development process, such as the grating period and line separation, with the primary work done on establishing the other variables. The result of this study did not produce a VBG with the highest available diffraction characteristics but a grating that was suitable for the aberration correction study. The grating period was 6 μm , this was initially selected to ensure distinct regions of pristine material between modified regions. This, however, result in a much higher order grating period for 633 nm light and was mostly one of the main reason the VBGs diffraction efficiency was capped at close to 50%. A period of $\sim 1.5 \mu\text{m}$ would have been more sufficient, matching the period found in commercially sold diffraction gratings and other ULI written gratings [94]. Equation 4 indication sub 1 μm period would be ideal at normal incidence but this may be below the limit of the writing capabilities of the present ULI system.

Moving on, for the layer separation a value of 2.26 μm was selected, giving sufficient overlap between layers to provide a consistent gradient of volume modification. These values were decided after reviewing the literature and discussion with Dr. David MacLachlan. They can of course be tuned to improve the results, however settling on these values allowed for more time to be allocated to the aberration compensation aspects of the project. Although these parameters were finalised early a study of the inscription pulse energies and the number of layers was still required.

For this project, a shallow grating means a grating writing between 100 μm and 250 μm , with the final VBG being written at a mean depth of 200 μm . However, this final configuration was not decided upon until after several rounds of parameter studies. The early studies were focused on a set of VBGs made with 8 layers of modified material. These 8-layer VBGs were written for a range of pulse

energies with the shallowest surface starting 100 μm below the substrate's surface. This 'thin grating study' showed that VBGs with so few layers were inadequate for the depth studies. The result of the pulse energy study and subsequent wavelength study are depicted in Fig. 45.

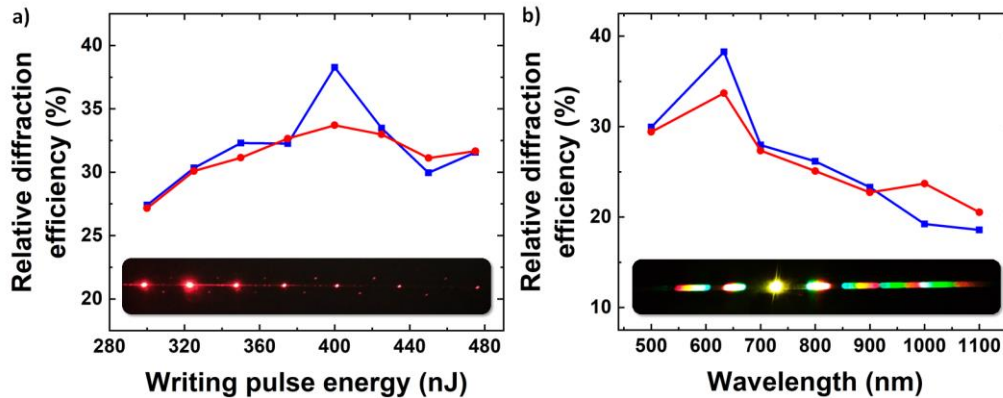


Fig. 45. Relative diffraction efficiency for P- (square markers, blue line) and S- (circle markers, red line) polarizations in percentage with respect to: a) writing laser pulse energy, showing a peak efficiency for horizontal light for a writing pulse energy of 400 nJ characterized using the HeNe laser, b) wavelength measurements using the SC assisted by a set of bandpass filters with a FWHM of 10 nm and showing a peak at 633 nm. Insert: a) diffraction pattern of the grating written with a pulse energy of 400 nJ, b) diffraction pattern of the grating written with a pulse energy of 400 nJ with the SC source without the bandpass filters.

The pulse energies used for the ULI process ranged from 300 nJ to 480 nJ, with the relative diffraction efficiency showing a peak at a pulse energy of 400 nJ - producing the first-order efficiency of 32.5% for S- polarised light, and 38% for P- polarised. This result was deemed to be too low for the aberration correction depth study. It was decided that above 40% was a suitable goal. This allowed for a measurable (via studying the manufacture VBG) decrease in reflective index change across the depth of a substrate while not prolonging this phase of the project. The wavelength dependent study showed a peak efficiency at 633 nm for both polarisations, meaning the grating period was selected appropriately. However, the thickness and pulse energy still needed further refinement. To this end, a series of VBGs were written with 400 nJ for a range of thicknesses: the theory being that the refractive index build-up over 8 layers did not allow for a higher diffraction efficiency. The VBG thickness ranged from 10, 15, 25, and then 40 to 80 microns in steps of 10. The results, while not producing the desired grating, did inform the next phase of parameters studies.

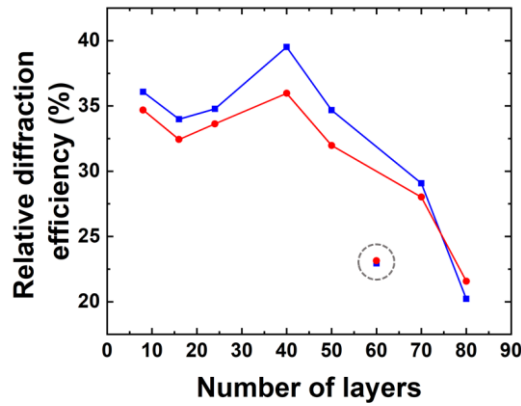


Fig. 46. Relative diffraction efficiency for P- (square markers, blue line) and S- (circle markers, red line) polarizations with respect to number of inscribed grating layers, fabricated with a laser pulse energy of 400 nJ. Experimental result measured for 60-layer grating points is presented in a grey dashed circle due to the relative diffraction efficiency result significantly deviating from the global trend presented.

Fig. 46 shows a peak in efficiency at 40 layers, producing a result close to that seen with eight layers – with the layer numbers before and after dropping in efficiency for both polarisation states. One outlier, which is highlighted in the figure, was the efficiencies of the 60-layer grating showing values far below the expected trend – this was most likely due to instabilities present in the system. These instabilities became more pronounced as the layers were increased: the increased manufacturing time made the system more susceptible to changing environmental conditions. Returning to Figure 46: the result with 40-layers was close to that with 8 and therefore was sufficient for the aberration correction study. The results obtained here showed that the grating thickness was not at the required extended, which was supported after returning to the literature to review the Mitukus et. Al paper.

VBGs with a thickness of around 100 μm did produce efficiencies close to 40% and as such this was the thickness selected for the next set of inscribed VBGs [94]. To produce a VBG of this thickness would require 45 layers, close to the 40 layers which produced the previously highest performing grating. A further alteration was the pulse energy. However, the writing pulse energy was significantly reduced, the reasoning being that with the increase in layers the combined refractive index change will result in increased scattering. The result in Fig. 47 shows the effects of these changes in parameters.

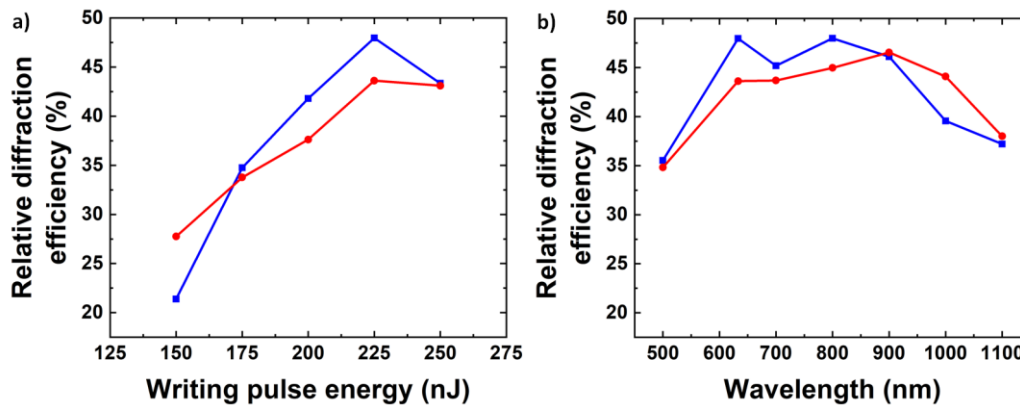


Fig. 47. Measured diffraction efficiencies for P- (square markers, blue line) and S- (circle markers, red line) polarized light. a) First-order diffraction efficiencies for VBGs fabricated using a range of pulse energies. It is observed that diffraction efficiencies >40% are realized using a pulse energy of 225 nJ. Here, the diffraction efficiency was measured using a HeNe laser at 633 nm. b) Measured diffraction efficiency vs wavelength for the VBG fabricated with 225 nJ pulses, showing that diffraction efficiencies above 40% relative diffraction efficiency could be obtained for wavelengths between ~600 nm and ~1000 nm.

The results show that a 45-layer VBG written at 225 nJ produced diffraction efficiencies for both polarisations over 40%. The wavelength study showed above 40% efficiency for values between 600 nm and 900 nm, with the peak value at 633 nm. This was an improvement on the previous set of gratings, however still not close to the ~90% efficiency - but this was not necessary for this study. The parameters were used for the depth study, where sets of gratings were written at a mean depth of 850 μm for a range of aberration coefficient masks and compared against a reference grating written at a mean depth of 150 μm .

While the grating parameters were set, there were still many challenges – often solved through trial and error. Issues arose early on when trialling early iterations of the Aerobasic scripts. VBGs were being inscribed at incorrect depths, or with incorrect layers and phase masks - this was exacerbated by the 12 hour manufacturing time for a single grating. The manufacturing times delayed the implementation of correction, which was further complicated when writing sets of five gratings. A set of five VBGs took two and half days of continuous laser writing, to complete which not only further delayed the diagnosing and solving of potential issues, but also increased the risks of environmental changes influencing the inscription. Continuous writing was necessary to ensure continuity with parameters - which may change over time, due to other researchers interacting with the system or environmental changes over days or weeks.

After much work a set of VBGs of suitable quality were manufactured at two depths and across six different aberration coefficients. The VBGs were inscribed within a 20 mm by 20 mm sample with a 1 mm thickness and with gratings at a mean depth of 200 μm and 900 μm for shallow and deep respectively. The shallow reference VBG was written with the Z(0) Zernike coefficient phase mask, meaning no aberration compensation was present. For the aberration coefficient, parameters ranged from Z(-3) to Z(-5) in steps of 0.5 – included again was the Z(0) phase mask. The final results showed the Z(-4.5) aberration correction phase mask produced a P- and S-polarisations relative diffraction efficiency of 42% and 36% respectively, an increase from the result of a VBG written at the same depth but with no correction mask (6% for P and 8% for S). Figure 48 (a) plots the change in relative diffraction efficiency as function of differing Zernike polynomials. Plot (b) in the same figure of the wavelength response of the best performing grating. Showing the 633 nm was still the best performing wavelength.

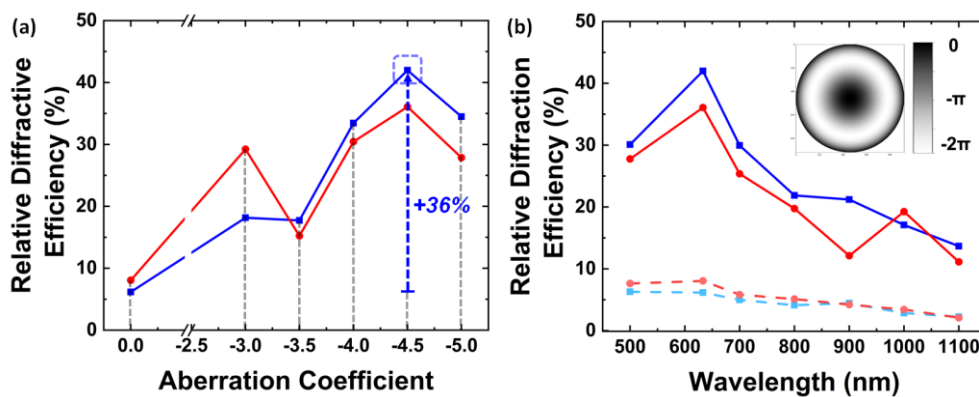


Fig. 48. (a) Relative diffraction efficiency versus aberration coefficient for a set of VBGs written at mean depth of 900 μm for a range of SLM profiles ranging from Z(0) to Z(-5), measured with both p- (square markers, blue line) and s- (circle markers, red line) interrogation beam polarizations. A blue dashed arrow highlights the best performance improvement when using the Z(-4.5) aberration coefficient mask. (b) Relative diffraction efficiency versus wavelength for a VBG written at a mean depth of 900 μm , for corrected (solid curves) and uncorrected (dashed dot curves), for both p- (square blue) and s- (circle red) polarizations. Inset: the Zernike polynomial component of the mask projected onto the SLM, for Z(-4.5) in grey scale from 0 to 2π .

This result, while a clear improvement upon the uncorrected value at the same depth, was also close to the diffraction efficiency of the reference grating which produced an S- and P-polarisation relative first order diffraction efficiency of 48% and 44% respectively. The work is further detailed in the final publication included in its entirety at the end of this chapter.

Beyond the results depicted in the final publication, a study of blaze angle vs relative first-order diffraction efficiency was also conducted. As covered, all results produced in the figures were taken at the ideal blazed angle, the angle which maximizes the positive first diffraction order. It was appropriate for the main studies but meant the angle dependency of the gratings was not reviewed. After questioning by one of the reviewers of the paper, the two best-performing gratings, the Z(0) shallow grating and the Z(-4.5) deep grating, were then studied for diffraction efficiency versus the angle of the grating. The result plotted in Figure 49 (a) shows a peak for a blazed angle of -4.5° for the reference grating, and -2.5° for the grating at depth.

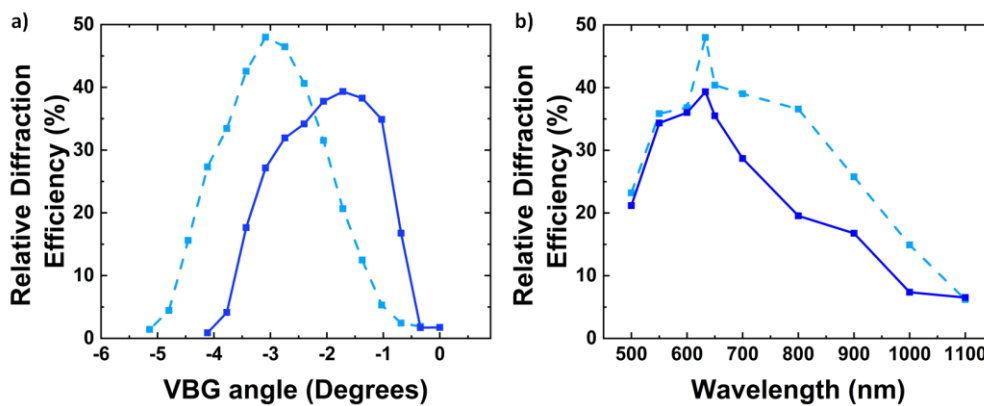


Fig. 49. a) Plot of relative diffraction efficiency vs angle for the reference angles (dashed curve, light blue), and corrected VBG written at a mean depth of $900\ \mu\text{m}$ (solid curve, dark blue), showing peak efficiencies at -4.5° and -2.5° respectively. b) Plot of relative diffraction efficiency vs wavelength for the reference grating and the corrected grating at $900\ \mu\text{m}$, at -4.5° and -2.5° respectively.

What is clearly shown in Fig. 49 (a) is that angles preceding and after the ideal blaze angle show a profound decrease. More interesting are the results depicted in (b) which show the wavelength dependency for both gratings at their ‘ideal’ angle. While the trend for the corrected grating at depth (dark blue, solid curve) follows close to that seen when maximising the angle, the uncorrected shallow grating is a drastic change. Before, as depicted in Figure 3 in the publication, there was $\sim 40\%$ efficiency for a band 600 nm to 900 nm; this has dramatically reduced. It appears to be the case that the grating writing without Zernike polynomials and at a shallow depth are far more angle dependent with respect to wavelength, where the correctly selected angle can greatly improve the diffraction efficiency.

There were more limitations with this approach to the study. While other depths and Zernike coefficients were studied briefly, none of the results made it to the point of a complete detailed study:

this was primarily due to time, but also due to an attempt to keep the project and results focused on one specific point. Although VBG writing was an important and time-consuming part of the project it was not the only component. For a complete understanding of the results gained with the grating, a plasma study was also conducted. This study was performed with the same depths and Zernike polynomials and allowed for a deeper understanding of the mechanics at play when correcting the aberration.

4.1.4. Introduction to free electron plasma imaging

The results detailed in the VBG study provided strong evidence that the method of adding Zernike polynomials to the ULI process did aid in maintaining the performance of VBG grating when inscribed at depth from 850 μm to 950 μm . These results were promising and with further development should be able to achieve aberration correction at arbitrary depth for a range of different ULI written photonic devices. However, the steps taken to acquire this data, and to write and test sets of VBGs, were time-consuming and provided conclusive results only for a limited depth and phase mask range. What was proposed was another study that provided results that would both aid in supporting the results acquired during the VBG study and could also stand on their own as a set of results and methods that take less laboratory time to acquire. Such a method could greatly accelerate the rate at which conclusive data can be acquired and decrease the time to successfully write structures or devices. Looking through the literature indicated that imaging the light emitted by the free electron plasma was the best method [96]. This was a complex procedure requiring a rigorous procedure to be laid out and followed to ensure accurate results were obtained. This made up the majority of the second half of this project, and the second half of the results in the publication attached at the end of this chapter.

The main challenge with this phase of the project was implementing a method of imaging the plasma to the now beam-shaping assisted ULI system. The method needed a high magnification, three-axis motion, and to be compatible with a range of optical filters and other components. For simplicity, an identical camera to the C1, depicted in Fig. 5 in Chapter 2, was selected to capture the plasma images. This camera needs a focusing objective and given the clearance available around translation

stages, a 6.5x zoom lens made by Thorlabs was selected. This lens contained a variable zoom which added flexibility – allowing for focus at varying depths within the fused silica substrate. On this objective was mounted firstly a near-infrared filter. From the initial testing of the lens, it was found there was a significant near-IR scattering within the substrate which obscured the broadband plasma: the filter rectifies this by removing the scatter. There was one further addition which was a neutral-density filter, specifically 0.5 ND. This was applied during certain conditions for which the intensity of the plasma over-saturated the camera. The system in its totality is depicted in the schematics in Fig. 50.

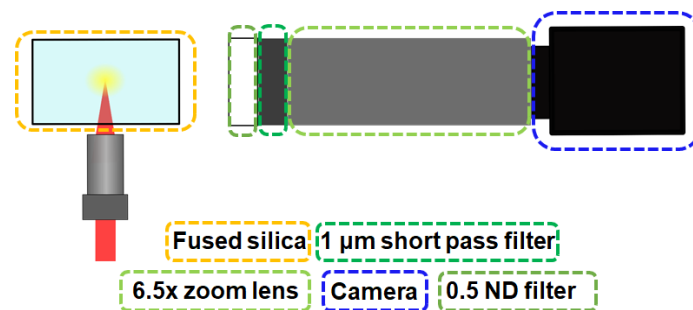


Fig. 50. Schematics of the plasma image camera setup. Details the camera, the zoom lens, the short pass filter, the neutral density filter, and the position of the fused silica sample.

Depicted in Fig. 50 is the camera, with the ND filter, IR filter, and zoom lens attached. This entire assembly was mounted onto a set of translation mounts, which allows it to be moved along the x, y, and z-axis so the camera can be positioned to better image the plasma. It is arranged such that the fused silica sample, which is mounted under the translation stage platform, is in full view at the lens's lowest zoom. One alteration had to be made to the writing stages: in their normal state there was not enough clearance below the sample mount to image the fused silica, so a similar mount, which was thinner along the edge was used instead. While that change in weight may affect the resulting inscription process and would need a recalibration of the air-bearing stages, in this case, it was unnecessary as any resulting structure of this study was not analysed. These additions to the writing systems were straightforward enough to be removed when nominal laser writing was being conducted and could be added in again within a matter of minutes. What took considerably more time was the design of a protocol to accurately and consistently capture the electron plasma.

One thing to consider when imaging the electron plasma is the extinction rate. When the laser pulse enters the substrate and generates the plasma the material begins to be modified. As the material changes the plasma generated will drop, often on a very short time scale. This fast extinction rate made capturing images of the plasma at its peak difficult. One possible solution is scaling up the pulse power as the material is being modified. Doing so, even after complete plasma extinction, will produce further plasma. However, this will give a misleading data set as the injection of further pulse power will result in plasma being generated within already modified material. The best solution for this project was to translate the substrate through the laser focus and to time the image captured such that the peak generation in pristine material was acquired. For each depth and phase mask, a single image was captured, as close to the peak plasma emission as possible. The capture was initiated shortly after the shutter was opened, while the substrate was positioned such that the modification was formed in pristine material. The peak pixel value of the image was taken as an indication of the plasma intensity. These steps were repeated five times per value, and then averaged. This process was conducted for four depths (including the reference depth) in the substrate for six Zernike coefficient masks. The depths related to the VBG's inscription positions, the first at 200 μm which was the mean depth of the reference grating. As with the VBG study this value acted as a reference as well as normalisation value. The remaining three depths represent positions of the VBG written at a mean depth of 900 μm . After the VBG inscription study it was clear the applied correction did not fully return the efficiency of the VBG to that which was achievable at shallower depths. One interesting possibility is that for a 100 μm spanning VBGs may require more than the single corrected phase mask to fully increase the performance. The plasma study was shaped to reflect that, where the range of Zernike coefficients were tested over 850 μm , 900 μm , and 950 μm depths within the substrate – reflecting the top, middle, and bottom of the VBG respectively. A wider spread of Zernike coefficients was also selected, giving an expanded view compared with the previous selection. Selected were: the -3, -4, -5, -6, and -7-polynomials, as well as the Z(0) phase mask. The peak pixel intensities of these values

were then compared to the intensity of the reference value: the closer the value was to the reference the more successful the correction was.

Along with a change in the selection of phase masks, the pulse energy was also changed. Certain depth and phase mask combinations produced a plasma intensity sufficiently high to saturate the camera. To solve this, the 0.5 ND neutral density filter was added which reduced the incident light by ~32%, below the saturation point of the camera. This allowed for an increase in pulse energy from 225 nJ to 300 nJ, improving the signal-to-noise ratio. The filter was applied to all values bar the Z(0) phase mask at 850 μm , 900 μm , and 950 μm depths, due to the amount of plasma generated at these conditions being considerably smaller. The pixel values were increased accordingly before the averaging and normalisation steps.

While difficult and time intensive this was found to be the best method to get the desired result within an appropriate time frame for this project. The results that were acquired were very enlightening and support the VBG study as well as providing another avenue for tuning the appropriate aberration compensation mask. The results regarding this study, which was included in the final publication, are depicted in Fig. 51.

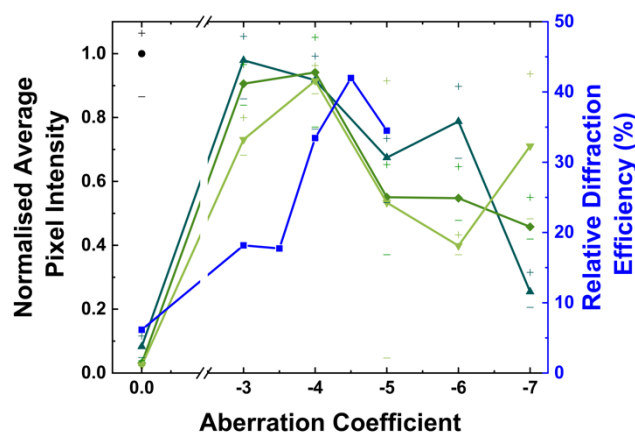
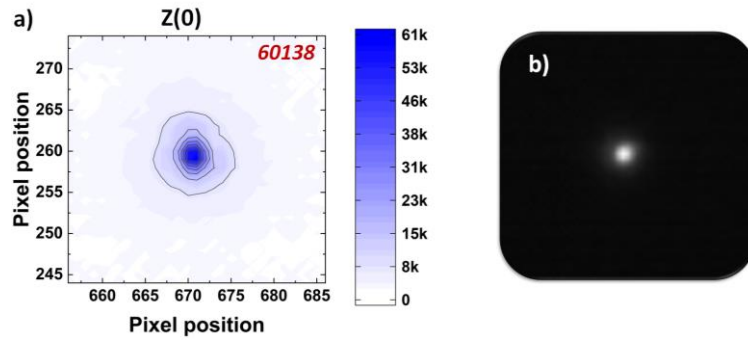


Fig. 51. The normalized average peak pixel intensity recorded when imaging plasma produced with a range of aberration coefficients at shallow and deep depths, namely: 200 μm (shallow reference, black point), 850 μm (dark-green upward triangle), 900 μm (green diamond), and 950 μm (light-green downward triangle). Each point is the normalized average of five measurements and the error bars represent the minimum and maximum measured values. The blue line represents the relative diffraction efficiency of a VBG written at 900 μm (interrogated with horizontally polarized 633 nm light).

The normalised average pixel intensities are plotted in three shades of green and are depicted with the relative diffraction efficiency of the best performing writing VBG (blue square); also included is the normalised average reference pixel intensity (black circle). The plot shows an increase in pixel intensity

with the application of Z(-3), however the increase and subsequent decrease of the pixel intensity is not homogenous across all layers. All layer depths have close intensity values when using the Z(-4) phase mask, close to the Z(-4.5) phase mask which produced the best performing written diffraction grating. This set of result not only supports the initial plasma study, but also provided some data toward the theory that more than a single correction coefficient maybe required for ideal correction of a 100 μm depth spanning structure. Fig. 52 shows a subsection of these results in more detail, depicting plots of the average pixel intensity for the Zernike range at the depth of 900 μm alongside the reference value.

200 μm – Reference



900 μm

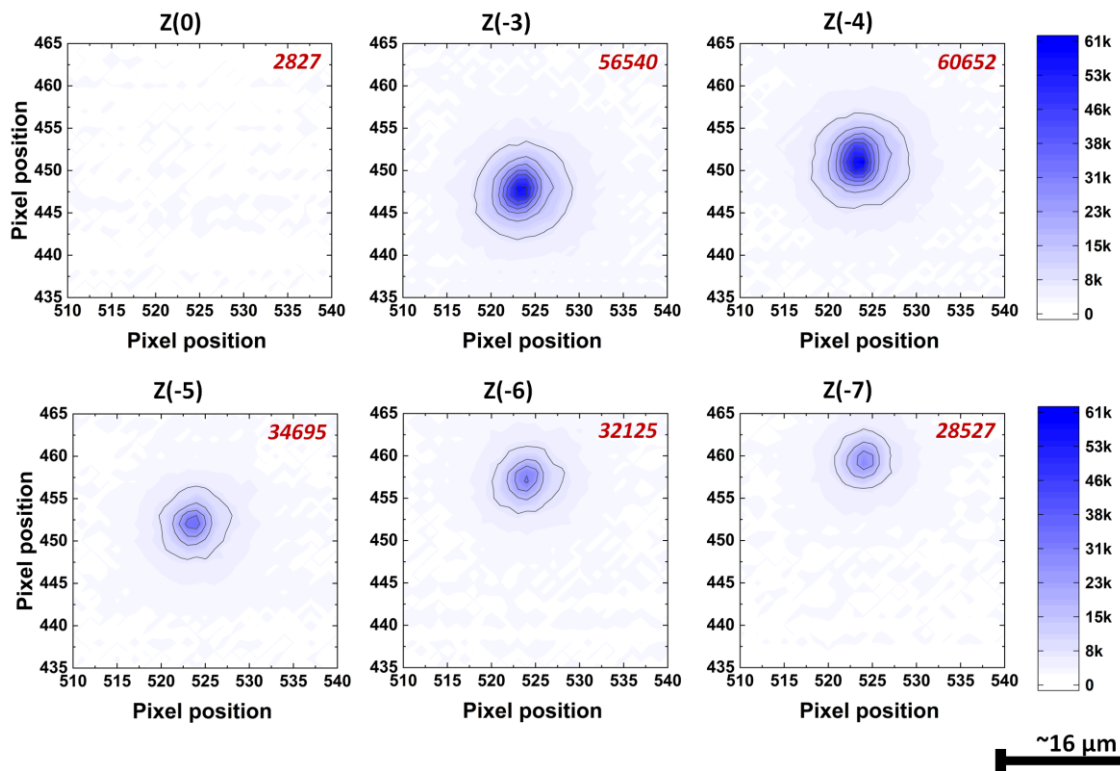


Fig. 52. A series of unnormalized plasma images split by depth. First shown is the 200 μm reference value where a) is the coloured and scaled image, and b) is the original plasma image. Second are the 900 μm depth plasma images for Z(0) to Z(-7). Images were taken with a monochromatic CMOS camera, coloured, and scaled in Origin. Shown is the peak pixel intensity in dark red for its respective plot.

These images are unnormalized but scaled when an ND filter was present to closer represent the intensity value. The reference shown in plot a) is well-defined and set the bar for what should be achieved with the Zernike correction mask. The plot b) is the image of electron plasma at the same

configuration but without the false colour and contour marking. These plots are followed by a selection of images taken at 900 μm . When no aberration correction is applied no plasma could be visualized at this scale. Along with the clear change in intensity value these plots also show a shift in the plasma's position relative to the camera. As the polynomial increases the focal volume, it also shifts it deeper into the substrate - further along the optical axis. It is currently believed that with the higher polynomial the SLM is attempting to focus the beam deeper into the substrate. This may mean that such a coefficient may be used to correct aberration at a deeper depth. A further study will need to be carried out to confirm whether that is the case. With development, improving data acquisition, and looking at a large range of depths and coefficients, this method could be used to truncate the parameter space, especially when this aberration compensation process is applied to the more complex structures in large volumes of substrate.

4.2. Author contributions

The majority of this work was conducted by myself. This included the coding and running of the inscribed VBG grating, the design and construction of the characterization setup with both laser systems, and the plasma imaging study. The second author of the paper, Mr Jacopo Siliprandi, was instrumental in the success of the paper. He produced a method of generating Zernike polynomials of the spherical type at a range of different magnitude coefficients. He did this using Python where he also combined the polynomial with the other phase mask component that was generated in Matlab. Along with his experimental contribution, he assisted in many sections of the paper, primarily in the written section on the Zernike polynomials, while I took the lead in the majority of the writing of the final publication.

Dr. David MacLachlan offered advice on the formation of volume Bragg gratings in fused silica. He has considerable experience in this area, manufacturing volume gratings in a range of materials to great success in many cases. His advice on both the manufacturing of the VBGs and their characterization greatly reduced the amount of time needed early in the project. Dr. Aurélien Benoît

assisted in the formation of the plasma imaging protocol and was present during the initial measurements, offering his feedback on the quality of the results. This was developed into the final consistent protocol. On top of this, he offered advice and feedback on the presentation and content of the figures and diagrams present in the paper. The final two authors, Prof. Robert Thomson and Dr. Calum Ross, were my academic supervisor and the lead post-doctoral researcher I worked with respectively. Prof. Thomson conceived the application of aberration compensation for enhanced VBG fabrication, provide support and feedback on the final written publication, while Dr. Ross supervised much of the paper writing, offering criticism and feedback. He also assisted in corrections and additions to the paper after the comments from the paper reviewers were received.

4.3. Review and further study

While limited in its scope the project shows promise in the use of the Zernike polynomial for the device manufactured by this group and in particular the spectrometer device. The main limitation of what is presented here is the focus only on one depth for one photonic device. Primarily this was done to keep the study as short and concise as possible. Regardless this set of results did produce a good foundation to build on for further studies, where more depths can be tested, as well as a lookup table of coefficients for a given depth within certain materials.

Since the paper was published the results have been presented at CLEO 2022. This included both VBG and plasma studies. Further work has, additionally, been carried out since then. Mr. Siliprandi has been applying aberration compensation to the inscription of channels for chemical etching. The goal of this study is not only to test for change (if any) to etching selectivity but also to test in a range of different depths, from around 1.5 cm. At the time of writing there has been no publication regarding this work. However, solely looking at the results depicted here, the knowledge and techniques gained greatly assisted in the development of the micro-spectrometer device.

4.4. Conclusion

The goal of this study was to produce a method of maintaining a consistent level of material modification across the depth of a dielectric substrate. With the SLM previously introduced into the ULI system - methods of aberration compensation were tested. This was firstly conducted via the manufacture of volume Bragg gratings. The results showed that via the application of a correctly scaled Zernike coefficient a VBG written at a mean depth of 900 μm produced comparable diffraction efficiency to that written at 200 μm . When the Z(-4.5) phase mask applied there was a ~42% increase in the relative first-order diffraction efficiency. However, the long manufacturing times limited the possible parameters this study could review. A method, which decoupled phase mask testing from device manufacturing, was conceived to allow for fast acquisition of aberration correction values. The proposed method was to image the electron plasma generated by ULI directly. Implemented directly into the ULI system, a set of result which supported the VBG manufacturing study were obtained. The plasm images acquired showed an equal intensity across three depths when generated with the Z(-4) phase mask. Results also showed evidence that multiple phase mask maybe be require to maintain a constant plasma intensity across the 100 μm the VBG spanned when writing at a mean depth of 900 μm . By applying these two studies together, spatial light modulator assisted beam shaping using Zernike polynomial, there is scope for correction of spherical aberration at arbitrary depths.

5. Prototype integrated spectrometer device

5.1. Development of a microspectrometer device via beam shaping-assisted ultrafast laser inscription

5.1.1. Review of current capabilities

With the implementation of beam shaping into the ultrafast laser microfabrication system, new avenues of manufacturing are now open. The two methods developed so far (beam elongation and aberration compensation) were vital to understanding the new SLM implemented system, but also provided tools necessary for the microfabrication of the proposed monolithic device.

The introduction of vortex beams allowed for a significantly reduction in inscription time – this allowed for the development of the microspectrometer. Each surface of the device and the VBG will need some form of material modification, and a short inscription time will aid in iterating the device development. The following sections cover the application of beam elongation in the starting stages of spectrometer development.

While the relatively thin 500 μm substrate is unlikely to impart severe spherical aberration onto the inscription laser, a subtle reduction in intensity may affect the consistency of the modification. This will not be an issue when inscribing surfaces to be etched due to the higher pulse energy requirement. This means you can increase the pulse energy to the point where aberration does not significantly reduce the selectivity. Where this reduction in the consistency of material modification will become important is when inscribing the volume Bragg grating. The VBG designed for the spectrometer needs to span the entire depth of the substrate (500 μm) and needs a length tangential to the optical axis within the spectrometer of 15 mm. If the entirety of its length has an inconsistent amount of modified material the diffraction efficiency will be negatively affected. The work carried out in Chapter [4](#), with a magnitude-scaled spherical aberration Zernike polynomial, can be used to maintain the modification of material across the entirety of the VBG.

5.1.2. Review of the current idea from the spectrometer device

The basic design of the spectrometer we aimed to develop was previously detailed in Chapter [1](#) of this thesis but will be reviewed again here. The spectrometer is based on a Czerny-Turner design,

containing two reflective surfaces and a diffraction grating. Fig. 53 is a schematic diagram, the same as the one shown in Chapter 1.

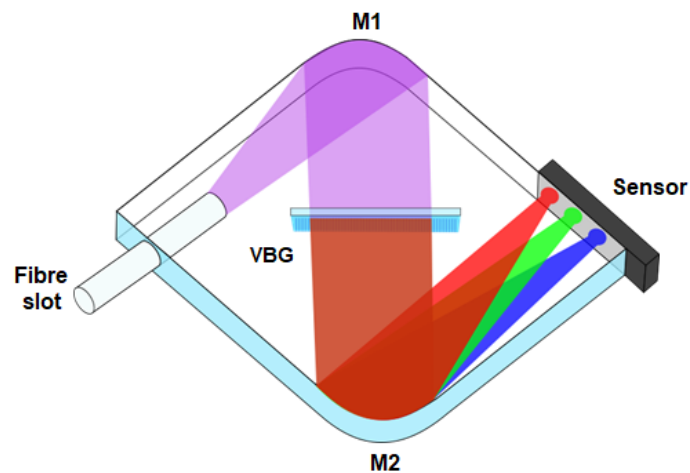


Fig. 53. Schematic diagram of the proposed monolithic spectrometer with a more detailed description of the individual components. This included a fibre slot for coupling of source light, a volume Bragg grating (VBG) in the grating plane, and a sensor in the image plane.

Detailed are the specific components needed for the proposed device. Firstly, an etched fibre slot allows for both the attachment and passive alignment of an input fibre. The fibre is permanently attached using a UV-cured refractive index matching glue. The optical beam coupled into the glass slab first diffracts, and then interacts with the first parabolic curved mirror (M1). This mirror is again formed by chemical etching and collimates the input beam as it directs it to the volume Bragg grating at the centre of the device. This VBG is formed via tracks of modification, stacked together to form a 3-dimensional volume. The diffraction characteristic of this grating is designed such that the resulting diffraction orders for the visible light place the positive first orders sufficiently far apart from each other for independent detection via a linear array sensor. The grating is followed by a second parabolic curved mirror (M2) that focuses the orders onto the image plane where this sensor is placed. The spectrometer in its totality will require both forms of material modification with pure modification and selective chemical etching.

With the addition of beam elongation, the manufacturing time of certain surfaces could be decreased; however, such a method could not be implemented for the VBG. During early calculations, it was found that manufacturing a grating suitable for this study would require days of continuous writing. This is beyond the acceptable timescale to effectively manufacture a grating with predictable

characteristics due to the manufacturing system being susceptible to shifting environmental conditions in the laboratory. Even with the temperature controls available in the labs, over the course of days, minor fluctuations in the optical components can reduce the writing fidelity of the laser inscription. This becomes more noticeable with the relatively low pulse energies required for pure modification.

There were two options available at the time to resolve this issue: commit time to the development of an elongated beam written VBG or revise the design of the micro-spectrometer. The former, while an exciting research avenue, did present several issues. The previous VBG study took a considerable amount of time to conduct, even with the low diffraction efficiency requirement. In the case of the spectrometer, the VBG would need to be as efficient as possible for the visible spectrum, as well as requiring a specific layout to ensure orders are not overlapping. Therefore, another parameter study would need to be conducted which would need to cover the change in grating parameters, as well as the range of vortex beam gradients. Regarding the vortex beam specifically, while a longer elongation would require fewer modified tracks to build up the VBG along the optical axis, the longer beams would have an increased thickness perpendicular to this axis. The increased thickness of the modified tracks will have to be considered when designing the VBGs, but a thorough test would be required regardless of how detailed the planning is. This is further complicated by the VBG needing to be in a different geometry, the opposite of that which was used for the previous grating study. While the application of a vortex beam would decrease the manufacturing time, the change in the thickness of the beam would also have to be considered when designing this study - in particular, considering that different vortex beam gradients will have different volume thicknesses. While the end goal of this proposed device will require such a study, it was not within the timescale available to this particular student and project. The alternative was to then redesign the spectrometer device such that the VBG is no longer required. The revised design would redesign the spectrometer so that the light propagating with the substrate interacts with an exterior diffraction grating. These changes are detailed in the following section.

5.1.3. Revisions to the spectrometer device

By removing the VBG from the spectrometer, the design and manufacturing process can be significantly truncated, allowing for a prototype device to be manufactured and tested before the end of the project. The main addition to the design was a large surface, where a blazed grating could be placed: Fig. 54 shows this altered design.

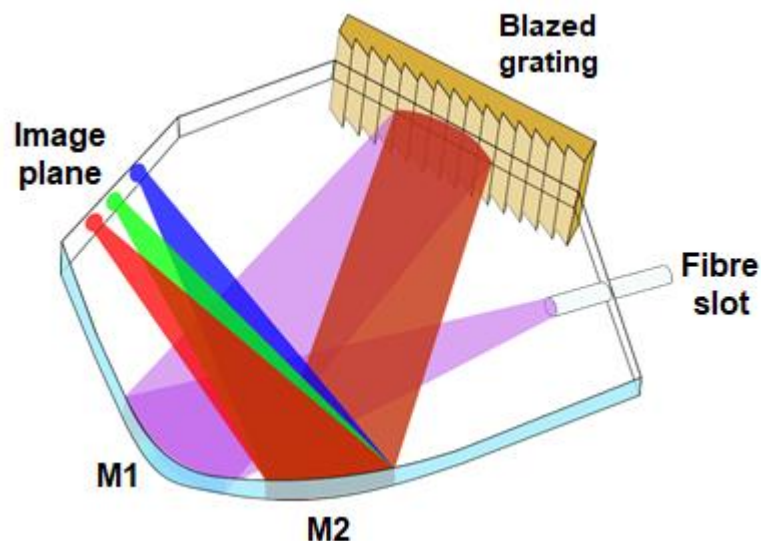


Fig. 54. Schematic diagram of the revised monolithic spectrometer. This included a fibre slot for coupling of source light, an exterior blazed grating, the two curved reflective surfaces, and a sensor in the image plane.

Several components were carried over to this revised design: this includes the fibre slot, the two reflected surfaces, and an image plane, shown in Fig. 54 without the linear sensor. The main difference was the introduction of the exterior blazed grating. To facilitate this the two curved mirrors had to be repositioned while maintaining the same collimating and focusing. M1 was positioned such that the beam is collimated onto the new surface with the exterior grating. M2 has moved accordingly, capturing the first-order reflections from this exterior grating, and focusing them onto the image plane. The quality of this surface must be sufficiently high to allow as few losses as possible during light transmission through and back through the surface. While not by any means a perfect solution (the use of this grating will require further alignment issues to be considered), it did mean the manufacturing time was significantly reduced.

The blazed grating itself was an off-the-shelf item, bought for this purpose from Thorlabs (GR25-0608). The selection available was of course limited but for the first prototype demonstrating

the basic operation of the device it was sufficient. The selected grating blazed wavelength was quoted as 750 nm for a blaze angle of 13°. This is formed via an aluminium reflective coating on a glass substrate: the repeating structure had a period of 600 / mm. The diffraction efficiency of the blaze wavelength at the blaze angle is between 60% and 80%, with a drop off to ~40% for wavelengths between 500 nm and 1000 nm. While this means the diffraction efficiency for the broadband light source will be very low, for a simple proof of concept the results should be sufficient. Once the design had been settled on, the process of scripting the inscription run, and the later chemical etching was relatively straightforward. One thing that needed to be kept in mind was the surface quality of certain surfaces. This was the main deciding factor on whether beam elongation was implemented. This will be covered in the next section.

5.1.4. Device inscription and etching

Once the spectrometer design revisions had been completed, the first prototype device was manufactured. Even without the integrated VBG, this provided a good opportunity to test the basic writing and etching parameters. Each surface of the spectrometer was split into two types: optical and non-optical. The primary difference between these two types is the surface quality requirements. Optical surfaces refer to any surface which interacts with a wavefront as it propagates in the material. For this design, these included curved mirrors and the interface for the diffraction grating, which are highlighted in red in Fig. 55.

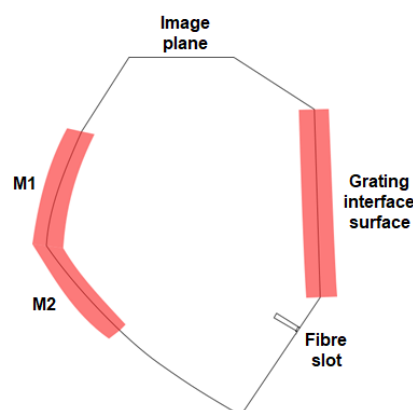


Fig. 55. Schematic diagram of the revised monolithic spectrometer with the main components labelled and the optical surfaces highlighted in red.

Along with the highlighted surfaces, the curved surface mirrors M1 and M2 are depicted, with the fibre slot, grating interface, and the image plane. Since optical surfaces interact with the wavefront, they need to be written with a high surface quality to prevent scatter losses. This restricted the use of vortex beams to surfaces that were not interacting with the wavefront, as it was found that the surface quality can be negatively impacted when elongation is applied. These optical surfaces, therefore, had to be written with the traditional line spacing and a Gaussian beam. The line spacing was set to 4 μm and the pulse energy was set to ~ 600 nJ, which produced a smoother surface after selective chemical etching, meaning these surfaces took the normal amount of time to inscribe. However, the non-optical surfaces were written with a vortex beam. By applying the 148 radians phase mask, a beam extension of ~ 200 μm was achieved, increasing the track separation to 160 μm along with an increase of the pulse energy to ~ 8000 nJ. This was a significant gain in manufacturing efficiency, resulting in a 1.5-hour total inscription time. Note that this time included inscribing the fibre slot which could only have been manufactured via traditional Gaussian beam inscription. The global laser parameters were a 50 kHz repetition rate and a pulse duration of 1.5 ps.

The selective chemical etching was done in 8 mol/L of potassium hydroxide (KOH) and heated to 85°C. The etchant was also circulated continuously with a magnetic rod, ensuring as close as possible to an even heat distribution within the liquid volume. It took around 2 hours to etch the final device. After this, a multimode fibre was UV glued into the fibre slot. Once fully dried the device could then be moved and brought to the characterization set up.

5.1.5. Device testing

For testing, the spectrometer was attached to a 5-axis translation stage. This allowed the image plane to be positioned, but the main use was for moving the device relative to the blazed grating. Fine control of this position is a requirement as the grating's surface is delicate. The spectrometer needs to be as close to the grating as possible, to limit scattering losses. However, if the edge of the spectrometer touches the grating it can scratch and damage the repeating structure. The grating was

mounted separately from the spectrometer, again to reduce the chance of damage. The schematic in Fig. 56 details the setup.

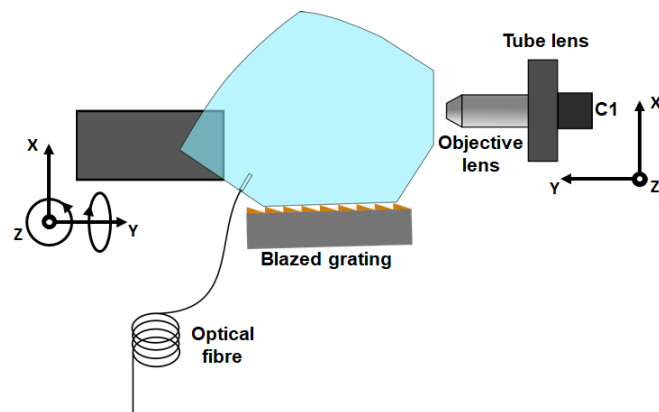


Fig. 561. Schematic diagram of the setup used to test the prototype spectrometer. Detailed are the optical fibre used to couple light into the spectrometer, the blazed grating, the objective lens, tube lens, and camera C1. Along with this are the directions of travel available to the spectrometer and imaging components.

An objective lens was used to image the image plane of the sample. The 4× objective lens (RMS4X, Thorlabs) was paired with a tube lens (TTL180-A) and mounted on its own set of translation stages, allowing it to be positioned appropriately. This alongside a CCD Thorlabs camera would theoretically be able to capture the separated orders of the probe’s light as it finishes its propagation through the device. Fig. 57 is a photograph of the spectrometer mounted on the analysis system (a) along with an image of the device as light propagated through it (b).

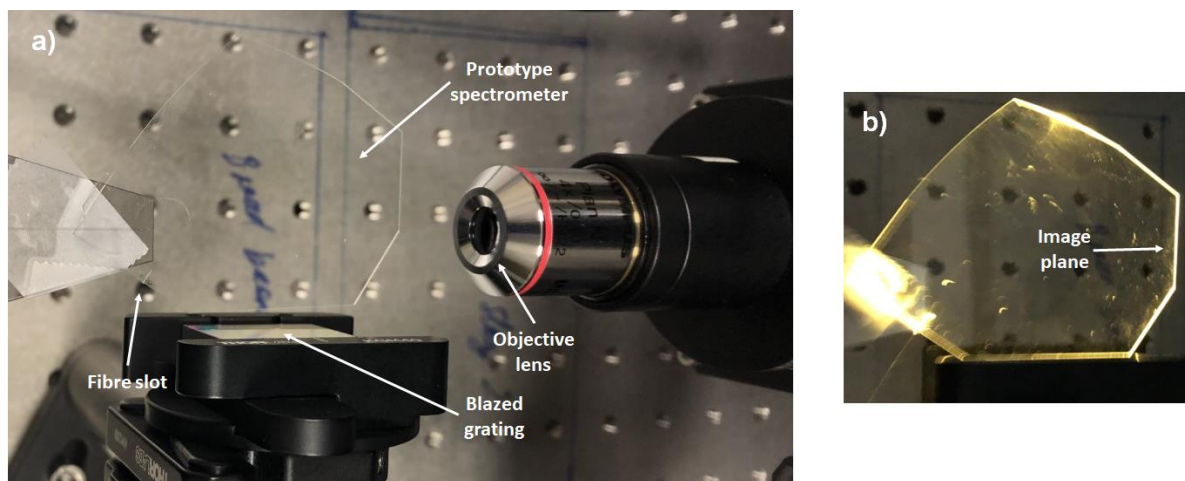


Fig. 57. Photographs of a) the prototype spectrometer mounted in the analysis systems, depicting the prototype, the grating, the fibre slot, and the objective lens. b) the spectrometer as the super-continuum light is coupled into it, highlighted is the image plane illuminated via the input light.

A super-continuum (SC) source was coupled into the multimode fibre and acted as the source light used to test the capabilities of the spectrometer. The light was successfully coupled into the

device and did propagate to the first optical surface M1, but the losses were too high, and no light was captured at the image plane. This was essentially where the project ended. Even when increasing the output power of the SC source, no light was present at the image plane, and as such, no power or throughput was measured. This means beyond the proof of applying a vortex beam to the design of the spectrometer very little quantitative data was acquired. If this specific test setup would be to be carried forward, there are several alteration that could be made. First surface polishing and sliver plating could be applied, reducing loses on the reflective surface. Secondly refractive index matching fluid could be added between the blazed grating and the spectrometer surface, removing losses present at the air-grating interface.

Regardless of the result this was the first step that would need to have been taken for the proposed monolithic integrated spectrometer and did allow for further planning for the following prototypes to be manufactured and tested by the next research on this project.

5.2. Discussion

5.2.1. Further development

Despite the failure of this first phase of prototypes a foundation for the future was laid. Given the limited time available for this specific part (the majority of the experimental focus being put into the development of the tool to manufacture such a spectrometer) this was a positive outcome, leaving a significant amount of useable data for the next researcher involved in the project.

First and most importantly a VBG writing study with vortex beam and aberration compensation must be devised. This may be one of the longest development stages in the path to a final spectrometer with a wide parameter space to study. The study, or studies, would need to consider the grating period when writing with vortex beams, taking into account the thicker transverse beam profile. It would also need to deduce the ideal axial elongation to use. A shorter focal extension will require more inscription time but produce a more consistent refractive index change across the volume of the grating. This will of course require a new pulse energy parameter scan. While the work carried out in Chapter 3 is directly relevant to this study one of the major changes that will affect the

characterisation is the change in the geometry of the VBG. The VBGs in Chapter 3 were written such that the interface of the grating was parallel to the top surface of the substrate. In the case of the spectrometer, the grating's interface will have to be perpendicular, such that it can interact with light propagating within the substrate. This change in geometry will require studying and planning to ensure it is done correctly; however, using the elongated beam will make increasing axial modification easier, requiring fewer or no stacked layers of inscribed material.

Some form of aberration compensation covered in Chapter 4 may also be required for the integrated spectrometer, particularly when it comes to fine-tuning the spectrometer's performance. The proposed plasma imaging study could be used to truncate the process of finding the ideal phase mask or masks for the 500 μm spectrometer. The result of this could then be integrated into the VBG study, ensuring a consistent level of modification can be achieved across the volume of the grating. However, an etching study would also have to be conducted. The primary goal would be to test surface quality versus aberration correction as the poor surface quality also contributed to the losses in the first prototype.

A further addition to this would be other methods of ensuring the optical surface has a high reflectance. A solution suggested during the project but never implemented would be silver coating those surfaces. An attempt was made to polish the surface using a Dremel and colloidal abrasive fluid. While this did make a difference in the surface quality, however, this had to be done carefully due to the fragility of the sample. Once these two steps have been studied to a satisfactory standard, they can be combined to manufacture a micro-spectrometer closer to that of the proposed design. Laser polishing may also be suitable for polishing the mirror surface assuming one is available. The characterisation system proposed here would be suitable for further studies of later iterations of the device.

The process of designing, manufacturing, and testing such a device is a long one and may take the work of many different researchers. With the work demonstrated here, the integration of beam shaping shows promise for the manufacture of an integrated spectrometer device. The basic

prototype shown at the conclusion of the work is the start of further development which may prove ULI to be an ideal process for a monolithic device, meeting future demands in a wide range of applications.

6. Conclusion

6.1. Vortex beam elongation

As the complexity of the structure being manufactured increases, so does the required manufacturing time. When time scales move from hours to days, the quality of the inscribed device can be negatively affected – this can be caused by changes in temperature and other environmental conditions. Even when subtle these can cause small changes in the optical alignment which can reduce the throughput power and other qualities one would desire to be stable. Proposed in this project was a method of decreasing the manufacturing time via the elongation of the focal volume of the inscription laser. When direct laser writing, both with refractive index change-based modification and those designed for selective chemical etching, regions of modification need to be stacked together to generate a structure. When forming a surface along the optical axis these regions need to be placed on top of each other with a sufficiently short distance between regions to ensure as close to a consistent level modification as possible. For very large surfaces or volumes, this will take very many individual regions which greatly increases the amount of inscription time. By the application of an elongated beam, the number of stacked regions can be reduced, decreasing the manufacturing time.

On-the-fly control of the focus elongation was enabled via a spatial light modulator (SLM) which was integrated into the current standard of the ultrafast microfabrication setup. The SLM allowed the writing beam to be phase shaped to produce the behaviour and in this case, was used to apply a vortex beam. A vortex beam was formed via a digital axicon where the encoded conical phase dictates the beam's axial extension. A series of parameter studies found high chemical etching selectivity of close to 1000 for a beam extension of $\sim 350\ \mu\text{m}$ was achievable. These results were put to the test by the manufacture surfaces using both traditional approaches using a Gaussian beam, and also the SLM-enabled vortex beams. When a vortex beam with a conical phase of 4.27 mrad (close to $350\ \mu\text{m}$) was used to write a 2 mm thick surface it showed a 12-fold reduction in manufacturing time. The only addition aside from beam shaping was an increase in the pulse energy, from 1620 nJ to 8100 nJ. Both surfaces showed comparable selectivity when etched with 8 M of 85°C KOH. These

results are detailed in the final publication produced at the end of this aspect of the project “Investigation focus elongation by spatial light modulation for high-throughput ultrafast-laser-induced selective etching in fused silica” [97]. Detailed is the use of vortex beams as a method of beam elongation which greatly decreased the laser inscription time. This has utility in industrial mass manufacturing, allowing more devices to be manufactured in shorter time scales. However, its main purpose in the context of this project was to aid in the manufacturing of the proposed integrated spectrometer device, where the elongated beam reduces the time required to inscribe the surfaces of the device.

6.2. Aberration compensation

A further impact of manufacturing complex or large structures is the depth-related aberration imparted onto the writing focus. As the focus moves deeper into a dielectric transparent material the refractive index change between the material and the air produces aberrant effects, which affect the fidelity of the focus. This causes a reduction in the energy and spatial distribution of the free electron plasma, which in turn reduces the extent of material modification. In effect, this means there are regions within a substrate that are inaccessible through the standard ULI process. This will in one way or another impact the proposed spectrometer design, in particular the VBG component of it. Looking at VBGs specifically - a high-efficiency VBG that operates as designed requires a consistent gradient of material modification across its entire volume. Even for very shallow depths (such as the 500 μm substrate selected for the proposed device) the reduction in electron plasma will produce a sub-optimal grating.

A method to compensate for this aberration would be beneficial for not just the spectrometer device but for direct laser writing photonic devices. With the SLM already integrated into the system, it was an ideal way to implement the correction. The spherical component of the beam aberration was compensated using a Zernike polynomial which directly represented the deviation from a unit circle spherical aberration produces. To control the amount of the compensation that was applied this

polynomial was scaled via an expansion coefficient, giving a range of different magnitude phase masks. The success of the aberration compensation was first demonstrated in this thesis in a VBG study.

VBGs that spanned 100 μm were written at two mean depths: 200 μm and 900 μm . The former shallow depth acted as a reference, where the final grating has a reduced amount of aberration. The latter, deeper gratings, were written with a series of different Zernike magnitude phase masks. The success of the correction was determined by the grating with the first-order diffraction efficiency closest to that of the reference measurement. The VBGs were designed primarily for 633 nm light and as such were studied using a HeNe laser; however, a broadband supercontinuum source was also used. This was mainly to ensure that a peak diffraction wavelength of 633 nm was achieved but also provided insight into the overall wavelength response of the VBG.

The results showed that a VBG written at 900 μm using the $Z(-4.5)$ phase mask produced a positive first-order relative diffraction efficiency of 41.9% for horizontal polarization. This was comparable to the 47.9% measured with the reference grating and was a 35.7% increase in the efficiency measured for an uncorrected grating at 900 μm . While a promising result, the 12-hour manufacturing time made doing larger parameter studies for more depth and Zernike expansion coefficient impossible in the timeframe available for this aspect of the project.

What was required was a faster method of gauging the success of the applied aberration correction, ideally without manufacturing and characterizing an optical device. To this end, a study to image the plasma directly was devised. In a similar fashion to the VBG study, a reference value was measured at 200 μm . Then to closely match the previous study three depths were studied, representing the top, middle, and bottom surfaces of the VBG written at a mean depth of 900 μm . Furthermore, a wider selection of phase masks was selected, giving a broader overview of the effect different Zernike polynomials had on the electron plasma. The results show a peak pixel intensity close to that at the reference for all depths at $Z(-4)$. However, by looking at a range of depths it was seen that there was an increase in the plasma intensity at a depth of 850 μm for the $Z(-3)$ phase mask. This added evidence to an earlier assertion that devices or structures over a certain size may require many

different Zernike magnitudes to maintain the same level of modification throughout. The results for both methods are detailed in the final publication “Volume Bragg grating written in fused silica at depth via spatial-light-modulator assisted aberration compensation” [88].

By combining both methods there is scope for the correction of spherical aberration present at arbitrary depth within a transparent substrate. The plasma study could be used to truncate the parameter space, reducing the amount of writing time needed to find the ideal Zernike magnitude for a certain depth. While having application in most forms of ULI-based devices, this method will have a major benefit to the integrated spectrometer device. It will ensure all components operate at their optimal configurations in a scenario where even minor losses will have a major effect on the utility of the final device.

6.3. Prototype spectrometer

These two developments were vital in gaining an understanding of and familiarity with beam-shaping-assisted ultrafast laser writing systems. However, at this early stage of development, the tools were not available to manufacture the spectrometer as initially designed. With the embedded VBG there was not enough time left in the project to fully develop the grating using both aberration compensation and beam elongation. To allow a prototype to be inscribed before the project ended, the design was altered. The reflective and imaging surfaces were moved to allow for an exterior to be used in place of the integrated VBG. While a departure from the original plan this did offer an opportunity to test the use of beam elongation for the etched surface. Via the application of the vortex beam phase mask with a 148 radians phase gradient, certain surfaces were manufactured at a faster rate. This was exclusive to surfaces that did not interact with the wavefront, as the currently available vortex beam writing did not produce sufficiently high surface quality. The final manufacturing time of the device was 2 hours. However, there were significant losses that resulted in no image being captured on the image plane. Despite the time restrictions and the failure of the final results, the results, and technique detailed here show promise for the use of ULI for the manufacture of monolithic

integrated photonic devices, where beam shaping can enable avenues of design that were before inaccessible to traditional systems.

6.4. Looking forward

The work in this project has laid a foundation of knowledge and techniques for the further development of a versatile ultrafast laser inscription system assisted by spatial light modulator driven beam shaping. With the SLM integrated ULI system already built and tested there is scope for further development, both with the techniques shown within thesis and many more. The application of vortex beams has shown significant increase in manufacturing times, while the use of aberration correction shows promise for the reduction in the loss of writing fidelity within large substrates. Both combine open new avenue for what ULI is capable of manufacturing. This includes but not limited to the proposed microspectrometer.

7. References

1. T. L. Dimitrova and A. Weis, "The wave-particle duality of light: A demonstration experiment," *Am. J. Phys.* **76**(2), 137–142 (2008).
2. C. J. Woodward, "On an apparatus to illustrate the interference of two plane waves," *Proc. Phys. Soc. London* **2**(1), 182–185 (1875).
3. Y. I. Nesterets and T. E. Gureyev, "Young's double-slit experiment: noise-resolution duality," *Opt. Express* **23**(3), 3373 (2015).
4. D. E. McCumber, "Einstein relations connecting broadband emission and absorption spectra," *Phys. Rev.* **136**(4A), 16–19 (1964).
5. G. Kirchhoff, "Ueber das Verhältniss zwischen dem Emissionsvermögen und dem Absorptionsvermögen der Körper für Wärme und Licht," *Ann. Phys. Chemie* **185**(2), 275–301 (1860).
6. M. C. Hutley, *Diffraction Gratings*, Techniques in Physics, 6 (Academic P., 1982).
7. J. W. Brault, "New approach to high-precision Fourier transform spectrometer design," *Appl. Opt.* **35**(16), 2891 (1996).
8. G. C. Bjorklund, "Measuring Weak Absorptions and Dispersions," *Opt. Lett.* **5**(1), 15–17 (1980).
9. D. Hunger, T. Steinmetz, Y. Colombe, C. Deutsch, T. W. Hänsch, and J. Reichel, "A fiber Fabry-Perot cavity with high finesse," *New J. Phys.* **12**, (2010).
10. D. Jervis, J. McKeever, B. O. A. Durak, J. J. Sloan, D. Gains, D. J. Varon, A. Ramier, M. Strupler, and E. Tarrant, "The GHGSat-D imaging spectrometer," *Atmos. Meas. Tech.* **14**(3), 2127–2140 (2021).
11. G. Dent and E. Smith, *Modern Raman Spectroscopy: A Practical Approach* (Wiley, 2005).
12. K. Kong, C. Kendall, N. Stone, and I. Notingham, "Raman spectroscopy for medical diagnostics - From in-vitro biofluid assays to in-vivo cancer detection," *Adv. Drug Deliv. Rev.* **89**, 121–134 (2015).
13. A. Rygula, K. Majzner, K. M. Marzec, A. Kaczor, M. Pilarczyk, and M. Baranska, "Raman spectroscopy of proteins: A review," *J. Raman Spectrosc.* **44**(8), 1061–1076 (2013).
14. Y. Ozaki, "Infrared Spectroscopy—Mid-infrared, Near-infrared, and Far-infrared/Terahertz Spectroscopy," *Anal. Sci.* **37**(9), 1193–1212 (2021).
15. S. Hyttel-Sorensen, A. Pellicer, T. Alderliesten, T. Austin, F. Van Bel, M. Benders, O. Claris, E. Dempsey, A. R. Franz, M. Fumagalli, C. Gluud, B. Grevstad, C. Hagmann, P. Lemmers, W. Van Oeveren, G. Pichler, A. M. Plomgaard, J. Riera, L. Sanchez, P. Winkel, M. Wolf, and G. Greisen, "Cerebral near infrared spectroscopy oximetry in extremely preterm infants: Phase II randomised clinical trial," *BMJ* **350**(January), 1–11 (2015).
16. T. Shi, Y. Chen, Y. Liu, and G. Wu, "Visible and near-infrared reflectance spectroscopy-An alternative for monitoring soil contamination by heavy metals," *J. Hazard. Mater.* **265**, 166–176 (2014).
17. D. Chorvat and A. Chorvatova, "Multi-wavelength fluorescence lifetime spectroscopy: A new approach to the study of endogenous fluorescence in living cells and tissues," *Laser Phys. Lett.* **6**(3), 175–193 (2009).
18. W. Becker, *Advanced Time-Correlated Single Photon Counting Techniques*, Springer Series in Chemical Physics (Springer Berlin Heidelberg, n.d.).
19. E. P. Farr, J. C. Quintana, V. Reynoso, J. D. Ruberry, W. R. Shin, and K. R. Swartz, "Introduction to Time-Resolved Spectroscopy: Nanosecond Transient Absorption and Time-Resolved Fluorescence of Eosin B," *J. Chem. Educ.* **95**(5), 864–871 (2018).
20. G. Garipey, J. Leach, R. Warburton, S. Chan, R. Henderson, and D. Faccio, "Picosecond time-resolved imaging using SPAD cameras," *Emerg. Imaging Sens. Technol.* **9992**, 99920N (2016).
21. S. A. Abdullah Albakri, M. N. A. Hussien, and H. Herdan, "Measurement of the distance to the central stars of Nebulae by using Expansion methods with Alladin Sky Atlas," *IOP Conf. Ser. Mater. Sci. Eng.* **757**(1), (2020).
22. X. Xu, Z. Zhang, H. Zhang, H. Zhao, W. Xia, M. He, J. Li, J. Zhai, and H. Wu, "Long distance measurement by dynamic optical frequency comb," *Opt. Express* **28**(4), 4398 (2020).
23. M. Mayor, C. Lovis, and N. C. Santos, "Doppler spectroscopy as a path to the detection of Earth-like planets," *Nature* **513**(7518), 328–335 (2014).
24. P. Gaulme, F. X. Schmider, and I. Gonçalves, "Measuring planetary atmospheric dynamics with Doppler spectroscopy," *Astron. Astrophys.* **617**, 1–14 (2018).
25. L. M. Narlagiri, M. S. S. Bharati, R. Beeram, D. Banerjee, and V. R. Soma, "Recent trends in laser-based standoff detection of hazardous molecules," *TrAC - Trends Anal. Chem.* **153**, 116645 (2022).
26. E. L. Izake, "Forensic and homeland security applications of modern portable Raman spectroscopy," *Forensic Sci. Int.* **202**(1–3), 1–8 (2010).
27. V. Robert and J. Robert, "Miniature spectrometer designs open new applications potential," *Laser Focus world* **49**(5), 34–44 (2013).
28. J. Zhou, D. Al Hussein, J. Li, Z. Lin, S. Sukhishvili, G. L. Coté, R. Gutierrez-Osuna, and P. T. Lin, "Mid-Infrared Serial Microring Resonator Array for Real-Time Detection of Vapor-Phase Volatile Organic Compounds," *Anal. Chem.* **94**(31), 11008–11015 (2022).
29. S. N. Zheng, J. Zou, H. Cai, J. F. Song, L. K. Chin, P. Y. Liu, Z. P. Lin, D. L. Kwong, and A. Q. Liu, "Microring resonator-assisted Fourier transform spectrometer with enhanced resolution and large bandwidth in single chip solution," *Nat. Commun.* **10**(1), 1–8 (2019).
30. D. Nevejans, E. Neefs, E. Van Ransbeeck, S. Berkenbosch, R. Clairquin, L. De Vos, W. Moelans, S. Glorieux, A. Baeke, O. Korablev, I. Vinogradov, Y. Kalinnikov, B. Bach, J. P. Dubois, and E. Villard, "Compact high-resolution spaceborne echelle grating spectrometer with acousto-optical tunable filter based order sorting for the infrared domain from 2.2 to 4.3 μm ," *Appl. Opt.* **45**(21), 5191–5206 (2006).
31. M. Florjanczyk, P. Cheben, S. Janz, A. Scott, B. Solheim, and D.-X. Xu, "Multiaperture planar waveguide spectrometer formed by arrayed Mach-Zehnder interferometers," *Opt. Express* **15**(26), 18176 (2007).
32. P. Gatkine, S. Villeux, Y. Hu, J. Bland-Hawthorn, and M. Dagenais, "Arrayed waveguide grating spectrometers for astronomical applications: new results," *Opt. Express* **25**(15), 17918 (2017).
33. J. Bland-Hawthorn, J. Lawrence, G. Robertson, S. Campbell, B. Pope, C. Betters, S. Leon-Saval, T. Birks, R. Haynes, N. Cvetojevic, and N. Jovanovic, "PIMMS: photonic integrated multimode microspectrograph," *Ground-based Airborne Instrum. Astron. III* **7735**, 77350N (2010).
34. A. Shafer, B. L. Megill, R., and L. Droppleman, "Optimization of the Czerny-Turner Spectrometer *," *I(7)*, 879–887 (1964).
35. O. M. Efimov, H. Francois-Saint-Cyr, L. B. Glebov, L. N. Glebova, K. Richardson, and V. I. Smirnov, "Photo-thermo-refractive glasses for high-efficiency Bragg gratings in UV, visible, and IR regions," in *Technical Digest. Postconference Edition. TOPS Vol.39*

- (*IEEE Cat. No.00CH37088*) (IEEE, 2000), p. 185.
36. J. Lumeau, "Photosensitive Materials : Optical properties and applications," Aix Marseille Universite (2016).
 37. K. O. Hill, Y. Fujii, D. C. Johnson, and B. S. Kawasaki, "Photosensitivity in optical fiber waveguides: Application to reflection filter fabrication," *Appl. Phys. Lett.* **32**(10), 647–649 (1978).
 38. K. O. Hill, B. Malo, F. Bilodeau, D. C. Johnson, and J. Albert, "Bragg gratings fabricated in monomode photosensitive optical fiber by UV exposure through a phase mask," *Appl. Phys. Lett.* **62**(10), 1035–1037 (1993).
 39. F. J. McClung and R. W. Hellwarth, "Giant optical pulsations from ruby," *J. Appl. Phys.* **33**(3), 828–829 (1962).
 40. A. J. Demaria, D. A. Stetser, and H. A. Heynau, "Self Mode-Locking of Lasers with Saturable Absorbers," *Appl. Phys. Lett.* **8**, 174–176 (1966).
 41. I. Orfanos, I. Makos, I. Lontos, E. Skantzakis, B. Förg, D. Charalambidis, and P. Tzallas, "Attosecond pulse metrology," *APL Photonics* **4**(8), (2019).
 42. D. Strickland and G. Mourou, "Compression of amplified chirped optical pulses," *Opt. Commun.* **56**(3), 219–221 (1985).
 43. J. Thomas, C. Voigtländer, R. G. Becker, D. Richter, A. Tünnermann, and S. Nolte, "Femtosecond pulse written fiber gratings: A new avenue to integrated fiber technology," *Laser Photonics Rev.* **6**(6), 709–723 (2012).
 44. C. Voigtländer, D. Richter, J. Thomas, A. Tünnermann, and S. Nolte, "Inscription of high contrast volume Bragg gratings in fused silica with femtosecond laser pulses," *Appl. Phys. A Mater. Sci. Process.* **102**(1), 35–38 (2011).
 45. R. R. Gattass and E. Mazur, "Femtosecond laser micromachining in transparent materials," *Nat. Photonics* **2**, 219–225 (2008).
 46. T. Toma, Y. Furuya, W. Watanabe, K. Itoh, J. Nishi, and K. Hayash, "Estimation of the Refractive Index Change in Glass Induced by Femtosecond Laser Pulse," *Opt. Rev.* **7**(1), 14–17 (2000).
 47. M. Beresna, M. Gecevičius, and P. G. Kazansky, "Ultrafast laser direct writing and nanostructuring in transparent materials," *Adv. Opt. photonics* **6**(3), 293–339 (2014).
 48. K. M. Davis, K. Miura, N. Sugimoto, and K. Hirao, "Writing waveguides in glass with a femtosecond laser," *Opt. Lett.* **21**(21), 1729–1731 (1996).
 49. K. Hirao and K. Miura, "Writing waveguides and gratings in silica and related materials by a femtosecond laser," *J. Non. Cryst. Solids* **239**(1), 91–95 (1998).
 50. D. Choudhury, J. R. Macdonald, and A. K. Kar, "Ultrafast laser inscription: Perspectives on future integrated applications," *Laser Photonics Rev.* **8**(6), 827–846 (2014).
 51. G. Brown, R. R. Thomson, A. K. Kar, N. D. Psaila, and H. T. Bookey, "Ultrafast laser inscription of Bragg-grating waveguides using the multiscan technique," *Opt. Lett.* **37**(4), 491 (2012).
 52. P. S. Salter, A. Jesacher, J. B. Spring, B. J. Metcalf, N. Thomas-Peter, R. D. Simmonds, N. K. Langford, I. A. Walmsley, and M. J. Booth, "Adaptive slit beam shaping for direct laser written waveguides," *Opt. Lett.* **37**(4), 470 (2012).
 53. A. Le Camus, Y. Petit, J.-P. Bérubé, M. Bellec, L. Canioni, and R. Vallée, "Direct-laser-written integrated mid-IR directional couplers in a BGG glass," *Opt. Express* **29**(6), 8531 (2021).
 54. R. R. Thomson, R. J. Harris, T. A. Birks, G. Brown, J. Allington-Smith, and J. Bland-Hawthorn, "Ultrafast laser inscription of a 121-waveguide fan-out for astrophotonics," *Opt. Lett.* **37**(12), 2331 (2012).
 55. R. R. Thomson, T. A. Birks, S. G. Leon-Saval, A. K. Kar, and J. Bland-Hawthorn, "Ultrafast laser inscription of an integrated photonic lantern," in *Optics Express (OPTICAL SOC AMER, 2011)*, **19**(6), pp. 5698–5705.
 56. R. R. Thomson, S. Beecher, N. D. Psaila, and A. K. Kar, "Ultrafast laser inscription of a high gain Er-doped bismuthate glass waveguide amplifier," *Opt. InfoBase Conf. Pap.* **18**(12), 13212–13219 (2010).
 57. G. Della Valle, A. Festa, G. Sorbello, K. Ennser, C. Cassagnetes, D. Barbier, and S. Taccheo, "Single-mode and high power waveguide lasers fabricated by ion-exchange," *Opt. Express* **16**(16), 12334 (2008).
 58. E. N. Glezer, M. Milosavljevic, L. Huang, R. J. Finlay, T.-H. Her, J. P. Callan, and E. Mazur, "Three-dimensional optical storage inside transparent materials," *Opt. Lett.* **21**(24), 2023–2025 (1996).
 59. Y. Lei, M. Sakakura, L. Wang, Y. Yu, H. Wang, G. Shayeganrad, and P. G. Kazansky, "High speed ultrafast laser anisotropic nanostructuring by energy deposition control via near-field enhancement," *Optica* **8**(11), 1365 (2021).
 60. P. Anderson, R. Black, A. Čerkauskaitė, A. Chatzileftheriou, J. Clegg, C. Dainty, R. Diaconu, A. Donnelly, R. Drevinskas, A. L. Gaunt, A. Georgiou, A. G. Diaz, P. G. Kazansky, D. Lara, S. Legtchenko, S. Nowozin, A. Ogus, D. Phillips, A. Rowstron, M. Sakakura, I. Stefanovici, B. Thomsen, L. Wang, H. Williams, and M. Yang, "Glass: A new media for a new era?," in *10th USENIX Workshop on Hot Topics in Storage and File Systems, HotStorage 2018, Co-Located with USENIX ATC 2018* (2018).
 61. C. A. Ross, D. G. MacLachlan, D. Choudhury, and R. R. Thomson, "Optimisation of ultrafast laser assisted etching in fused silica," *Opt. Express* **26**(19), 24343–24356 (2018).
 62. S. Zhou, L. Shen, F. Wang, Y. Li, H. Zhang, S. Wang, and S. Zhou, "High-aspect-ratio ZnSe microstructure generated by spatially shaped femtosecond laser writing assisted with wet chemical etching," *Opt. Laser Technol.* **147**(August 2021), 107687 (2022).
 63. C. Hnatovsky, R. S. Taylor, E. Simova, V. R. Bhardwaj, D. M. Rayner, and P. B. Corkum, "Polarization-selective etching in femtosecond laser-assisted microfluidic channel fabrication in fused silica," *Opt. Lett.* **30**(14), 1867 (2005).
 64. Y. Liao, J. Song, E. Li, Y. Luo, Y. Shen, D. Chen, Y. Cheng, and Z. Xu, "Lab on a Chip Rapid prototyping of three-dimensional microfluidic mixers in glass by femtosecond laser direct writing †," *Lab Chip* **12**, 746–749 (2012).
 65. Z. Hu, A. Glidle, C. N. Ironside, M. Sorel, M. J. Strain, J. Cooper, and H. Yin, "Lab on a Chip Integrated microspectrometer for fluorescence based analysis in a microfluidic format," *Lab Chip* **12**, 2850–2857 (2012).
 66. N. Bellini, K. Vishnubhatla, R. Ramponi, R. Osellame, F. Bragheri, L. Ferrara, P. Minzioni, and I. Cristiani, "Trapping and stretching of single cells in an optofluidic chip fabricated by a femtosecond laser," in *Optics InfoBase Conference Papers* (2010), **18**(5), pp. 4679–4688.
 67. P. Paiè, F. Bragheri, A. Bassi, and R. Osellame, "Selective plane illumination microscopy on a chip," *Lab Chip* **16**(9), 1556–1560 (2016).
 68. S. W. Luo, T. L. Chang, and H. Y. Tsai, "Fabrication of diffractive microlens array by femtosecond laser-assisted etching process," *Microelectron. Eng.* **98**, 448–452 (2012).
 69. C. A. Ross, D. G. MacLachlan, B. J. E. Smith, R. J. Beck, J. D. Shephard, N. Weston, and R. R. Thomson, "A miniature fibre-optic raman probe fabricated by ultrafast laser-assisted etching," *Micromachines* **11**(2), 1–16 (2020).
 70. Y. Bellouard, A. A. Said, M. Dugan, and P. Bado, "High accuracy micro-displacement sensor with integrated optics-based detection means," in *Proceedings - IEEE International Conference on Robotics and Automation* (2005), **2005**(May), pp. 850–854.
 71. N. Savage, "Digital spatial light modulators," *Nat. Photonics* **3**(3), 170–172 (2009).

72. K. Lu, "Spatial Phase Modulator," *Opt. Eng.* **29**(3), 240–246 (1990).
73. G. Lazarev, A. Hermerschmidt, S. Krüger, and S. Osten, "LCOS spatial light modulators: Trends and Applications," *Opt. Imaging Metrol. Adv. Technol.* 1–29 (2012).
74. W. D. G. Improso, G. A. Tapang, and C. A. Saloma, "Suppression of zeroth-order diffraction in phase-only spatial light modulator via destructive interference with a correction beam," in *PHOTOPTICS 2017 - Proceedings of the 5th International Conference on Photonics, Optics and Laser Technology* (Scitepress, 2017), **2017-Janua**, pp. 208–214.
75. *Introduction to Fourier Optics / by Joseph W. Goodman.*, 3rd ed. (Roberts and Company, 2005).
76. T. Kurihara and Y. Takaki, "Improving viewing region of 4f optical system for holographic displays," *Opt. Express* **19**(18), 17621 (2011).
77. Y. Wu, J. Ma, Y. Yang, and P. Sun, "Improvements of measuring the width of Fraunhofer diffraction fringes using Fourier transform," *Optik (Stuttg.)* **126**(23), 4142–4145 (2015).
78. K. Kumorowska, A. Miniewicz, J. Parka, and F. Kajzar, "Self-induced nonlinear Zernike filter realized with optically addressed liquid crystal spatial light modulator," *J. Appl. Phys.* **92**(10), 5635–5641 (2002).
79. J. Durnin, J. H. Eberly, and J. J. Miceli, "Comparison of Bessel and Gaussian beams," *Opt. Lett.* **13**(2), 79 (1988).
80. P. Fischer, H. Little, R. L. Smith, C. Lopez-Mariscal, C. T. A. Brown, W. Sibbett, and K. Dholakia, "Wavelength dependent propagation and reconstruction of white light Bessel beams," *J. Opt. A Pure Appl. Opt.* **8**(5), 477–482 (2006).
81. R. Dharmavarapu, S. Bhattacharya, and S. Juodkazis, "Diffractive optics for axial intensity shaping of Bessel beams," *J. Opt. (United Kingdom)* **20**(8), 85606 (2018).
82. C. A. Ross, K. Harrington, J. M. Stone, T. A. Birks, and R. R. Thomson, "Ultrafast Laser Fabricated Fused Silica Fibre Preforms," in *Conference on Lasers and Electro-Optics* (Optica Publishing Group, 2022), p. SW5K.2.
83. N. Huot, R. Stoian, A. Mermillod-Blondin, C. Mauclair, and E. Audouard, "Analysis of the effects of spherical aberration on ultrafast laser-induced refractive index variation in glass," *Opt. Express* **15**(19), 12395 (2007).
84. I. V. Ciapurin, "Modeling of phase volume diffractive gratings, part 1: transmitting sinusoidal uniform gratings," *Opt. Eng.* **45**(1), 015802 (2006).
85. S. Y. Haffert, R. J. Harris, A. Zanutta, F. A. Pike, A. Bianco, E. Redaelli, A. Benoît, D. G. MacLachlan, C. A. Ross, I. Gris-Sánchez, M. D. Trappen, Y. Xu, M. Blaicher, P. Maier, G. Riva, B. Sinquin, C. Kulcsár, N. A. Bharmal, E. Gendron, L. Staykov, T. J. Morris, S. Barboza, N. Muench, L. Bardou, L. Prengère, H.-F. Raynaud, P. Hottinger, T. Anagnos, J. Osborn, C. Koos, R. R. Thomson, T. A. Birks, I. A. G. Snellen, and C. U. Keller, "Diffraction-limited integral-field spectroscopy for extreme adaptive optics systems with the multicore fiber-fed integral-field unit," *J. Astron. Telesc. Instruments, Syst.* **6**(04), (2020).
86. V. Stankevič, J. Karosas, G. Račiukaitis, and P. Gečys, "Investigation of the modifications properties in fused silica by the deep-focused femtosecond pulses," *Opt. Express* **31**(3), 4482 (2023).
87. M. J. Booth, M. A. A. Neil, R. Juskaitis, and T. Wilson, "Adaptive aberration correction in a confocal microscope," *Proc. Natl. Acad. Sci. U. S. A.* **99**(9), 5788 (2002).
88. S. R. McArthur, J. Siliprandi, D. G. MacLachlan, A. Benoît, R. R. Thomson, and C. A. Ross, "Ultrafast laser inscription of efficient volume Bragg gratings deep in fused silica using active wavefront shaping," *Opt. Mater. Express* **12**(9), 3589 (2022).
89. K. Fuerschbach, J. P. Rolland, and K. P. Thompson, "Theory of aberration fields for general optical systems with freeform surfaces," *Opt. Express* **22**(22), 26585 (2014).
90. A. Jesacher and M. J. Booth, "Parallel direct laser writing in three dimensions with spatially dependent aberration correction," *Opt. Express* **18**(20), 21090 (2010).
91. B. V. N. Mahajan, "Zernike Annular Polynomials and Optical Aberrations of Systems with Annular Pupils," *Appl. Opt.* **33**(34), 8125 (1994).
92. J.-M. Wang, C.-L. Liu, Y.-N. Luo, Y.-G. Liu, and B.-J. Hu, "Statistical virtual eye model based on wavefront aberration," *Int. J. Ophthalmol.* **5**(5), 620–624 (2012).
93. V. Lakshminarayanan and A. Fleck, "Zernike polynomials: a guide," *J. Mod. Opt.* **58**(7), 545–561 (2011).
94. M. Mikutis, T. Kudrius, G. Šlekys, D. Paipulas, and S. Juodkazis, "High 90% efficiency Bragg gratings formed in fused silica by femtosecond Gauss-Bessel laser beams," *Opt. Mater. Express* **3**(11), 1862–1871 (2013).
95. D. Choudhury, J. R. Macdonald, and A. K. Kar, "Ultrafast laser inscription: Perspectives on future integrated applications," *Laser Photonics Rev.* **8**(6), 827–846 (2014).
96. A. Jesacher, G. D. Marshall, T. Wilson, and M. J. Booth, "Adaptive optics for direct laser writing with plasma emission aberration sensing," *Opt. Express* **18**(2), 656 (2010).
97. S. R. McArthur, R. R. Thomson, and C. A. Ross, "Investigating focus elongation using a spatial light modulator for high-throughput ultrafast-laser-induced selective etching in fused silica," *Opt. Express* **30**(11), 18903 (2022).

8. Appendix

8.1. “Investigating focus elongation using a spatial light modulator for high-throughput ultrafast-laser-induced selective etching in fused silica”

Investigating focus elongation using a spatial light modulator for high-throughput ultrafast-laser-induced selective etching in fused silica

SAM R. MCARTHUR^{1,2}, ROBERT R. THOMSON¹ AND CALUM A. ROSS^{1,3}

¹Scottish Universities Physics Alliance (SUPA), Institute of Photonics and Quantum Sciences (IPaQS), Heriot-Watt University, Edinburgh, UK, EH14 4AS

²srm37@hw.ac.uk

³calum.ross@hw.ac.uk

Abstract: Ultrafast-laser-induced selective chemical etching is an enabling microfabrication technology compatible with optical materials such as fused silica. The technique offers unparalleled three-dimensional manufacturing freedom and feature resolution but can be limited by long laser inscription times and widely varying etching selectivity depending on the laser irradiation parameters used. In this paper, we aim to overcome these limitations by employing beam shaping via a spatial light modulator to generate a vortex laser focus with controllable depth-of-focus (DOF), from diffraction limited to several hundreds of microns. We present the results of a thorough parameter-space investigation of laser irradiation parameters, documenting the observed influence on etching selectivity and focus elongation in the polarization-insensitive writing regime, and show that etching selectivity greater than 800 is maintained irrespective of the DOF. To demonstrate high-throughput laser writing with an elongated DOF, geometric shapes are fabricated with a 12-fold reduction in writing time compared to writing with a phase-unmodulated Gaussian focus.

Published by Optica Publishing Group under the terms of the Creative Commons Attribution 4.0 License. Further distribution of this work must maintain attribution to the author(s) and the published article's title, journal citation, and DOI.

1. Introduction

Sub-bandgap ultrafast laser pulses (pulse width < 10 ps) can induce non-linear photon absorption processes when focused into wide bandgap materials such as fused silica. Depending on the irradiation parameters, various permanent material modifications can occur to material that is placed in the tightly confined laser focus, while the surrounding material is left unchanged. One of the most intriguing and applicable modifications induced by ultrafast laser inscription in fused silica is an enhanced chemical etching rate of the laser modified material [1–3]. This enhancement allows complex three-dimensional micro-components to be fabricated by first laser inscribing a structure into a substrate and subsequently subjecting the substrate to a chemical etchant to preferentially remove the inscribed material. This technique offers several advantages over other microfabrication techniques which make it highly desirable, including micrometre feature resolution, the ability to write embedded features, and maskless etching. Conversely, there are some limitations which must be considered when designing a component for fabrication, including: polarization dependent etching rates, long laser writing times and geometry dependent etching selectivity. These limitations have hindered the translation of ultrafast-laser-induced selective etching from a predominantly research-based tool towards wider adoption as an industrial microfabrication process.

To overcome these limitations, several groups have investigated optimal laser writing parameters and advanced laser writing techniques. A vast parameter space exists in terms of the laser irradiation and etching parameters that affect the resultant selectivity of the etching process. Parameter space investigations typically involve writing arrays of channels or surfaces with different parameters and measuring the subsequent etching rates [4–9]. These studies reveal interesting characteristics of the laser writing and etching process. For example, etching selectivity is found to be highly polarization dependent under certain irradiation conditions [10] due to the formation of directional *nanogratings* which facilitate etchant transport anisotropically. Nanogratings can facilitate very high etching selectivity but present a challenge of how to modulate the laser polarization while writing complex surface geometries. Recently however, longer pulses (> 2 ps) were shown to overcome the strong polarization dependence [11], achieving high selectivity even for circularly polarized light. Early work on laser-induced selective etching primarily used hydrofluoric acid as the chemical etchant, with optimal writing parameters delivering a selectivity of up to 100 [12]. In more recent years, heated potassium hydroxide has been shown to offer an etching selectivity of over 1000 [13], while maintaining similar etching rates to HF [14], and has therefore become the most commonly used etchant. Etching conditions [6,15], writing speed [6,7], pulse energy [8,16] and pulse repetition rate [4] are just some of the other parameters that have been investigated through parameter studies.

Further to using optimal irradiation and etching conditions, advanced writing techniques have also been explored for improving the fabrication process. These include cross-polarised double-pulse writing [17], multispot writing [18], pulse-train modulation [19], pulse front shaping [20,21] and spatiotemporal focusing [22,23]. Recently, beam shaping has become extremely appealing in laser machining [24], enabled by advances in adaptive optics instrumentation such as spatial light modulators (SLMs), which are now more cost effective, offer higher pixel densities and better optical power handling. SLMs allow near arbitrary phase profiles to be imparted across the laser beam pixelwise, and can mimic the role of traditional optics and compensation plates to perform aberration correction and beam shaping amongst an abundance of other applications. Of particular interest is the ability to shape the laser focus to suit a particular laser processing task more efficiently. For example, Bessel beams, which are “non-diffracting” and maintain a high-intensity central lobe over relatively long axial distances, can be generated by passing a Gaussian beam through an axicon lens (strictly speaking, forming a Gaussian-Bessel (GB) beam). The elongated focus of a GB beam permits more material to be processed in a single laser-pass while maintaining lateral resolution. Bessel beams formed using physical axicon lenses have been used for several glass microfabrication applications including low-loss waveguide writing, volume gratings [25,26], microchannels [27,28] and glass dicing [29]. Beam shaping using physical optics is limited by the discrete nature of the optic form, introduces alignment challenges, and offers less design freedom. SLMs provide a practical solution to generating Bessel beams without introducing the restrictions of incorporating physical axicon lenses into the beam path and have also been utilised for glass dicing [30], and fabricating microchannels [31] and micro-holes [32].

There are two common approaches for generating GB beams using an SLM: The first involves displaying a simple annular grating on the SLM, which transforms into a GB beam in the far field [33], i.e. 1-f after a lens positioned 1-f away from the SLM. In fact, any complex amplitude can be obtained in the far-field by generating its Fourier Transform (FT) at the SLM plane. The second method requires a conical phase profile to be imposed on the SLM, analogous to a physical axicon lens, forming a GB beam in the Fresnel plane immediately upon reflection from the SLM. The former method is inefficient as it makes use of only a small portion of the SLM display, while the second approach is efficient but typically incompatible with the 4-f imaging system used to relay image the SLM onto the back aperture of the writing objective to perform aberration correction or write with a diffraction limited Gaussian focus. For many manufacturing applications, it would be beneficial to write with both a traditional Gaussian focus and a GB focus depending on the component geometry.

Recently, zero-order vortex beams, formed by performing the FT of a GB beam [34] (by passing through a lens, for example) were demonstrated for laser-based microfabrication, exhibiting an elongated high-intensity focal region [35,36]. Here, we explore the use of a vortex beam generated by introducing a conical phase front to a Gaussian beam via an SLM, forming an optical vortex at the laser processing focal plane after propagation through a 4-f lens relay system and a flat field objective lens – the ideal optical path for several beam shaping and aberration correction applications used during microfabrication. Crucially, we find that material modification is confined to an elongated high-intensity region preceding the focal plane, with the degree of elongation determined by the magnitude of conical phase front imparted on the beam.

In this paper, we present the results of a thorough investigation into the effects of laser irradiation parameters and SLM generated conical phase front on the etching selectivity and cross-section of microchannels written in fused silica. Writing parameters investigated include the pulse duration (180 – 5900 fs), pulse energy (0.12 – 14.4 μ J), pulse repetition rate (25 – 500 kHz) and sample translation speed (1 – 128 mm/s). The axial laser depth-of-focus (DOF) was varied by applying phase fronts with conical tilt ranging between 0 to 4.27 mrad. To illustrate the benefit of controllable DOF during laser writing, the rapid fabrication of various geometric fused silica forms by laser writing and subsequent chemical etching is presented.

2. Materials and methods

2.1 Laser inscription and etching

For this work, ultrashort pulses with tuneable pulse width (180 – 5800 fs) were generated by a diode-pumped ytterbium-doped bulk laser system (*Pharos*, Light Conversion), with a central wavelength of 1030 nm. The pulse repetition rate was varied between 25 and 500 kHz and an average power of up to 10 W was available. Fig. 1 depicts the functional components of the laser inscription system.

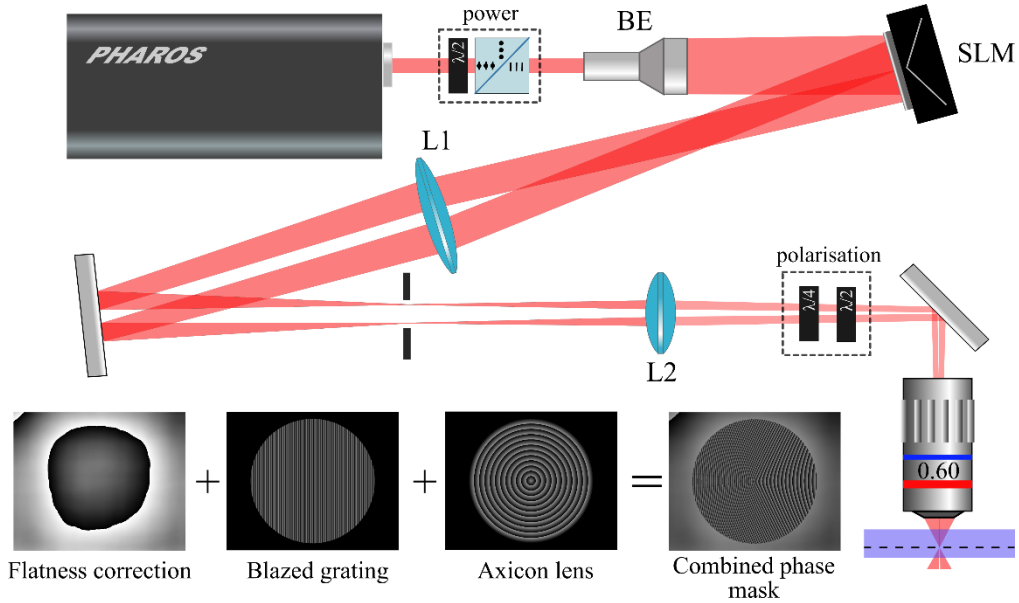


Fig. 1: A schematic of the laser inscription system. BE: $3\times$ beam expander, L1: 1000 mm biconvex lens, L2: 400 mm biconvex lens, inscription lens: 0.6 NA long-working-distance objective. Inset: Three phase masks are combined to form the desired beam: a flatness correction mask to compensate for SLM imperfections, a blazed grating to efficiently diffract light into the first order, and an axicon lens for generating the vortex beam.

The laser was first passed through a Galilean beam expander with $3\times$ magnification to increase the beam width from 4.5 to 13.2 mm (to $1/e^2$) in order to sufficiently fill the aperture of the SLM. We used a reflective liquid crystal on silicon (LCOS) SLM (X13138-08, Hamamatsu) with a 1272×1024 -pixel array measuring 16×12.8 mm. The laser was directed onto the SLM at an angle of incidence of 5.5° . The SLM was configured to diffract light into the first order, the details of which are discussed in Section 2.2. We observed a dramatic reduction in the SLM's diffraction efficiency when the average incident power was above ~ 2.4 W and therefore limited the average power to below this value. We speculate this drop in efficiency was due thermal effects, a known limitation of SLMs and particularly those relying on an aluminium reflective coating such as that used here, as opposed to a dielectric coating.

After the SLM, the beam was passed through two biconvex lenses in a 4-f configuration (L1 = 1000 mm, L2 = 400 mm), to demagnify and image the SLM display onto the entrance pupil of the writing objective. A 4-f system is required to relay not only the amplitude profile of the image but also its phase, as imaging with a single lens introduces an undesirable quadratic phase term. The 4-f system also provides a convenient intermediate image plane at which an aperture can be positioned to filter out unwanted diffraction orders. After L2, the collimated beam was passed through a zero-order quarter-waveplate followed by a zero-order half-waveplate mounted within motorized rotation mounts (DDR25/M, Thorlabs) for polarization control. Finally, the beam was passed through a long working distance (10 mm) objective with NA = 0.6 (PAL-50-NIR-HR-LC00, OptoSigma) and an effective focal length of 4 mm, and focused into the sample. Sample translation was provided by a 3-axis air-bearing direct-drive stage (ABL1000, Aerotech). A useful guide to implementing SLMs for laser processing and microscopy is offered by the *Dynamic Optics and Photonics Group*, University of Oxford [37].

The glass used in this study was 1 mm thick high purity fused silica (7980 0F, Corning). After laser inscription, samples were submerged in an etching bath containing 8 mol/L potassium hydroxide (KOH) heated to 85°C and magnetically stirred throughout the etching period. These conditions have been investigated previously and provide high etching selectivity [14]. The thinning rate of pristine material under these etching conditions was previously reported by us to be 0.38 ± 0.02 $\mu\text{m}/\text{h}$, and this value was used to determine the etching selectivities reported here.

2.2 Vortex beam generation

The SLM imposes a phase front across the laser beam by controlling the effective path-length of light passing through the liquid crystal display, pixelwise. Each pixel typically allows up to 2π of phase delay. For most applications, the phase profile required spans a larger range than $0 - 2\pi$ and this is achieved by *wrapping* the required phase value to the modulo of 2π . To apply the phase profile, an 8-bit (256 intensity levels) bitmap with phase encoded intensity values was simply projected on the SLM display via a digital video interface (DVI) cable connected to a computer.

The bitmap is a summation of various phase maps carrying out specific functions: Firstly, it is necessary to correct for any physical flatness deviation on the SLM display itself by applying a flatness correction mask which is often supplied by the SLM manufacturer, though can be determined experimentally [38]. Secondly, it is often

beneficial to apply a multilevel blazed diffraction grating via the SLM to diffract the laser light efficiently into the first diffraction order. This prevents unmodulated light in the zeroth order from degrading the desired beam profile. Here, a 16-level blazed grating was applied with an effective grating period of 6.25 lp/mm, providing a diffraction efficiency of ~82% into the first order. Finally, to mimic the function of an axicon lens, a positive (i.e., positive maximum phase shift on the optical axis) conical phase mask was generated. The magnitude of phase shift at the centre, φ (radians), is related to the conical phase base-angle, α (radians) and semi-diameter of the active area of the SLM imaged onto the pupil plane of the objective, R , for a given wavelength, λ , by Eq. 1:

$$\alpha = \frac{\varphi\lambda}{2\pi R} \quad (1)$$

Note that the base-angle of a physical axicon lens producing a phase shift, φ , is equal to $\alpha/\Delta n$, where Δn is the refractive index difference between the lens and the surrounding medium. The base-angle is a common axicon parameter and is useful for comparing systems utilizing SLM-generated and physical lenses. In our investigation, we generated phase masks with peak phase shifts of 0, 37.5, 75, 112.5 and 150 radians, corresponding to conical phase base-angles of 0, 1.07, 2.13, 3.20 and 4.27 mrad for a semi-diameter, R , of 5.76 mm. The combined phase mask is simply the sum of the flatness correction, diffraction grating and conical front, wrapped at 2π , as depicted in Fig. 1. When the laser reflects off the SLM, the conical phase mask produces a GB beam in the near-field, which is reimaged to the back aperture of the objective lens and transformed into a vortex beam at the laser-writing focal plane. A mathematical description of a vortex beam generated by the FT of a GB beam is provided in Ref. [34].

2.3 Parameter investigation

A parameter-space investigation was carried out to explore the effects of laser irradiation on both the laser-induced etching selectivity and the elongation of the modified region, for a range of conical phase fronts. Three parameter space subsets were investigated: firstly, a preliminary scan of pulse duration, pulse energy and axicon gradient; secondly, a finer scan of pulse duration, pulse energy and writing speed, and thirdly, a comprehensive study of pulse energy, writing speed, conical phase front and pulse repetition rate. As noted, previous studies have demonstrated that high etching selectivity can be achieved with circularly polarised pulses under certain conditions, overcoming the need for polarization alignment during fabrication. This benefits the fabrication technique greatly, and therefore we used circularly polarized light at the substrate throughout the work presented here.

For each parameter combination, a single transverse channel was written into the substrate, with the focal plane positioned 500 μm nominally beneath the surface, i.e., a stage movement of 500 μm into the glass. To account for beam clipping at the substrate edge, the samples were mechanically diced 2 mm in from the edge to expose the channel facets prior to etching. The channels were then etched for 3 hours before micrographs were taken of the channels' cross-section and the etched lengths.

3. Results

3.1 Parameter space investigation

The first parameter investigation was carried out to determine the influence of pulse energy, pulse duration and conical phase angle on the etching selectivity and channel cross-section. For this parameter set, the repetition rate was fixed at 50 kHz, the beam was circularly polarised and the sample was translated at 4 mm/s. For these parameters, the number of spatially overlapped pulses irradiating the material was approximately 19 (see Supplement 1 for calculation). In order to reduce the occurrence of self-focusing and consequent filamentation due to nonlinear Kerr lensing, the pulse energy was limited to 350 nJ for the Gaussian focused beam (conical phase angle = 0 mrad), compared to 2200 nJ for the vortex beams. Light emitted from the partial free-electron plasma, formed within the laser focus, was imaged from the side to indicate the modification threshold and focus elongation. Micrographs of the plasma emission with and without a conical phase font are presented in Fig. 2 (a) and (b) respectively. Selected channel cross-sections written with both Gaussian and vortex beams for different pulse energies are presented in Fig. 2 (c). Although the vortex beam is expected to form a ring at the focal plane, it is evident that ionisation is dominant within a central high-intensity region just prior to the focal plane, resulting in the elongated modification channel observed. We observed no significant difference in the channel widths for channels formed with Gaussian and vortex beams, and rather the width was determined predominantly by the pulse energy.

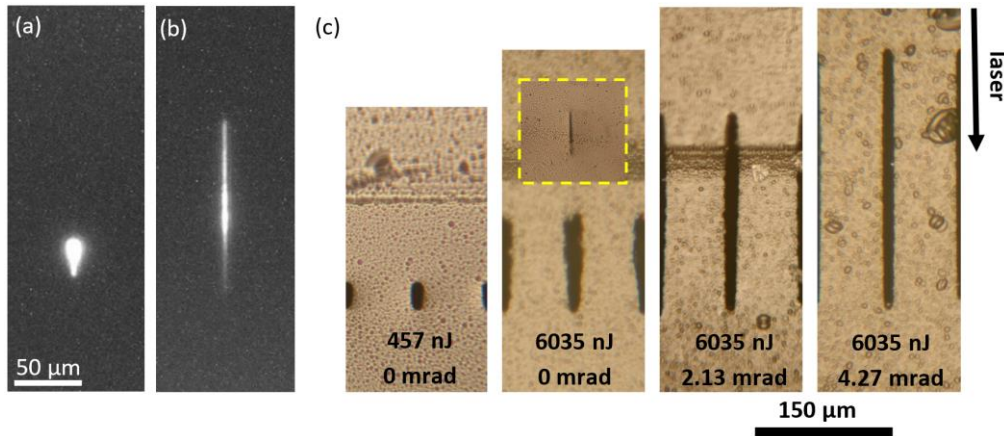


Fig. 2: (a) and (b) are micrographs of partial free-electron plasma emission from the focal region inside fused silica under irradiation with a Gaussian and vortex focus (generated by imparting a 3.20 mrad conical phase front) respectively. (c) is a series of micrographs showing etched channel facets written with a range of pulse energies and conical phase masks to highlight the DOF elongation. The repetition rate was 50 kHz, polarisation was circular, translation speed was 4 mm/s and the pulse duration was 1440 fs when writing the channels shown. Inset: A corresponding channel cross-section prior to etching (at same scale).

Graphs displaying the selectivity and elongation of the etched channels from the first parameter investigation are presented in Fig. 3. The most significant uncertainty in the selectivity originates from the variation in temperature of the etching bath which dramatically affects the etching rate of the pristine material. Therefore, the uncertainty in the selectivity is approximately equal to the percentage uncertainty in the pristine etching rate of silica at 85 ± 2 °C, i.e. 0.38 ± 0.02 μm/h or $\pm 5.3\%$. Note that some degree of variance in the laser writing and etching process is expected beyond this, but repeated measurements for each parameter set was impractical given the size of the parameter-space investigated. Several clear trends were observed, and others more subtle: As expected, a minimum pulse energy threshold was required to induce selective etching; this threshold increased for longer pulses and steeper conical front. The selectivity generally plateaued at higher pulse energies for the range investigated. The selectivity was generally higher for longer pulses and particularly, noticeably lower for 180 and 360 fs pulse durations (note, polarisation was circular). This observation is in agreement with previous research suggesting that for longer pulse durations, the nanogratings that enable high selectivity lose their directionality and become randomly orientated, facilitating highly selective etching even for circularly polarised light [11]. The height of the channels after etching, i.e., the DOF, denoted as the *elongation* here, was found to increase with pulse energy gradually to a broad peak before falling again slightly in most cases. Most significantly, introducing conical phase profiles via the SLM resulted in channel elongation proportional to the conical phase front base-angle. This observation was true up to a conical angle of 3.20 mrad, beyond which the elongation began to decrease. Prior research has demonstrated that the focal volume intensity distribution of a vortex beam is a complex combination of writing depth, conical base-angle and direction and pulse energy, and that the elongation increases with base-angle only up to a point, at which the focus becomes less well-defined and the elongation reduces [35]. We also note that for steeper conical phase fronts, the diameter of the propagated annular beam increased and became susceptible to aperturing. It is also apparent that simply increasing the pulse energy increases the DOF even when no conical phase is applied. For the pulse energy range investigated here, this elongation can be attributed simply to an increase in the extent of the focal volume above the modification threshold. At higher pulse energies, filamentation is also expected to contribute to the elongation of the modified region and this was explored further in the third set of parameters investigated.

The elongation of the preferentially etched material was also less for longer pulses with comparable pulse energy, particularly for pulse durations of 2880 and 5900 fs. We suspect that this is due to the reduction in peak intensity within the focus, leading to a smaller laser-affected volume. An optimum pulse duration exists, then, in which both selectivity is high for circularly polarized light (≥ 720 fs) and the modification volume is efficiently elongated (≤ 2880 fs).

The substrate translation speed is another important factor when considering efficient microfabrication. To investigate the influence of translation speed on the etching selectivity and focus elongation, it too was investigated as a function of pulse energy and pulse duration. The results of this investigation are presented as line plots in Fig. 4. Channels were again written at a nominal depth of 500 μm, with translation speeds ranging from 1 to 8 mm/s (corresponding to 75 to 10 overlapped pulses) and pulse energies from 500 to 2250 nJ. Since the first parameter investigation determined that a minimum pulse duration between 720 and 1440 fs is required for optimum etching performance, pulse durations from 1080 to 5900 fs were investigated here. A fixed conical phase angle of 3.20 mrad was used, as this resulted in longest elongation after the first investigation.

We observed that the substrate translation speed was only significant for pulse durations of 1080 and 1440 fs, for which slower writing speeds resulted in significantly lower etching rates. We also observed that the modification elongation decreased slightly as the pulse duration increased. The results suggest that to achieve longest modification elongation along with highly selective etching, pulses with durations from 1080 to 1440 fs with translation speeds > 3 mm/s are optimum. For scenarios in which the translation speed is limited, longer pulses may give better results.

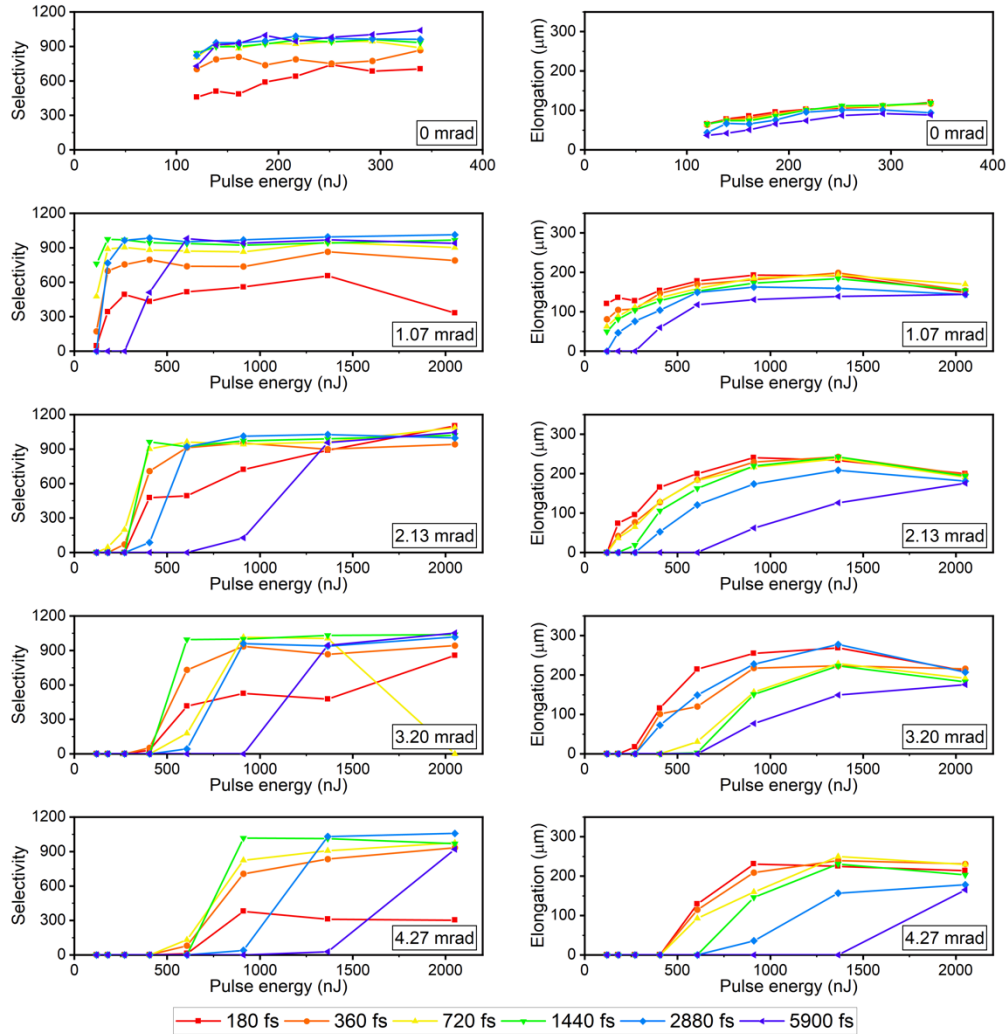


Fig. 3: Line graphs displaying etching selectivity (left) and DOF (right) for several SLM generated conical phase masks for varying pulse energy and pulse duration. In each case, the laser polarisation was circular and the translation speed was 4 mm/s. The uncertainty in the selectivity is approximately 5.2%.

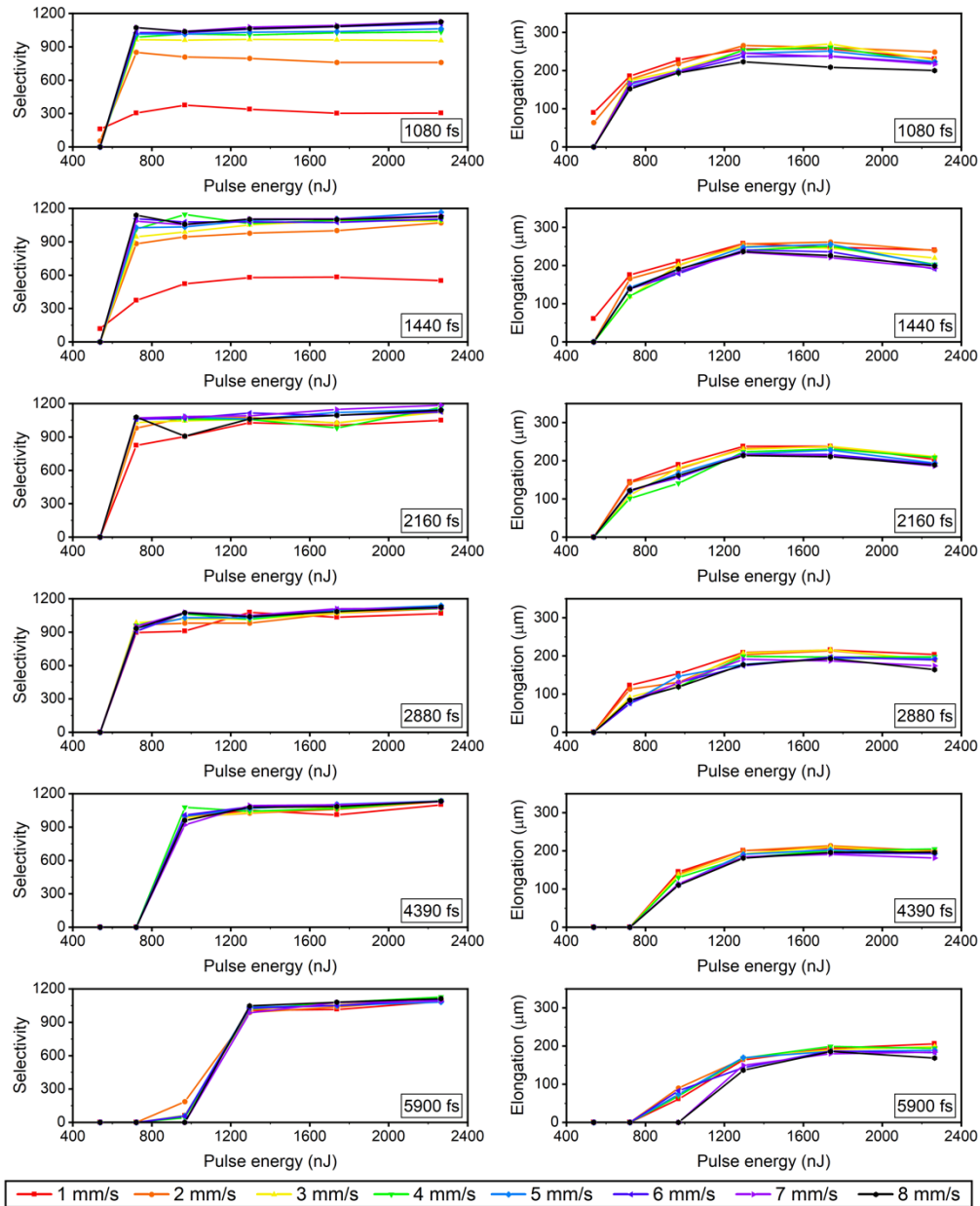


Fig. 4: Line graphs displaying etching selectivity (left) and DOF (right) for several pulse durations with varying pulse energy and writing speed. In this case, the laser polarisation was circular and the axicon base-angle was fixed at 3.20 mrad. The uncertainty in the selectivity is approximately 5.2%.

With the optimum parameters narrowed down, a third and final parameter set was investigated, exploring a wide range of pulse repetition rates, pulse energies and writing speeds for several conical phase angles starting at 0 mrad. Again, single-pass channels were inscribed in fused silica at a nominal depth of 500 μm and chemically etched for 3 hours. The achieved selectivities and DOFs are presented as heat maps in Fig. 5. For this investigation, the pulse duration was kept constant at 1440 fs, because this produced highest selectivity and elongation for the broadest set of irradiation parameters in the initial studies. The dark blue regions represent parameters in which no material modification was observed, and the grey regions represent inaccessible parameters due to the average power surpassing the maximum efficiently handled by the SLM as discussed earlier. Each pulse energy increment along the x-axis of the heat map is subdivided into eight increments which represent eight translations speeds use: 1, 2, 4, 8, 16, 32, 64 and 128 mm/s.

The results highlight that the pulse energy threshold for modification increases with larger conical base-angle, as expected. An interesting behaviour was observed when varying the translation speed parameter: For lower pulse energies, faster writing speeds resulted in a lower etching rate, suggesting that the optimum fluence was not reached at those speeds. However, we also observed etching rates were sub-optimal when slowest writing speeds were used in many cases, suggesting that pulse overlap also has an optimum value. This behaviour was not observed for the elongation however, where an inverse relationship between writing speed and elongation was

observed. Further, we observed that the optimum translation speed for high etching selectivity increased with higher repetition rates for similar pulse energies, suggesting the total fluence determines the morphological change rather than the individual pulse energy, in agreement with previous studies [16]. This observation is significant for industrial manufacturing applications as it implies that fabrication time can be reduced simply by increasing the writing speed and repetition rate proportionally. Challenges remain however in overcoming the average power limits handled efficiently by modern LCOS-SLM's. Indeed, we observed that only the lowest repetition rate, corresponding to lowest average power, resulted in fully elongated channels.

Again, channel elongation was proportional to the conical base-angle where sufficient pulse energy was available. For this parameter set, channels were also written at high pulse energies for a base-angle of 0 mrad. In this regime, filamentation due to Kerr self-focusing is likely, and indeed we recorded DOF elongation up to 147 μm for 14.4 μJ pulses. However, this is still substantially less than the DOF observed when writing with a vortex beam.

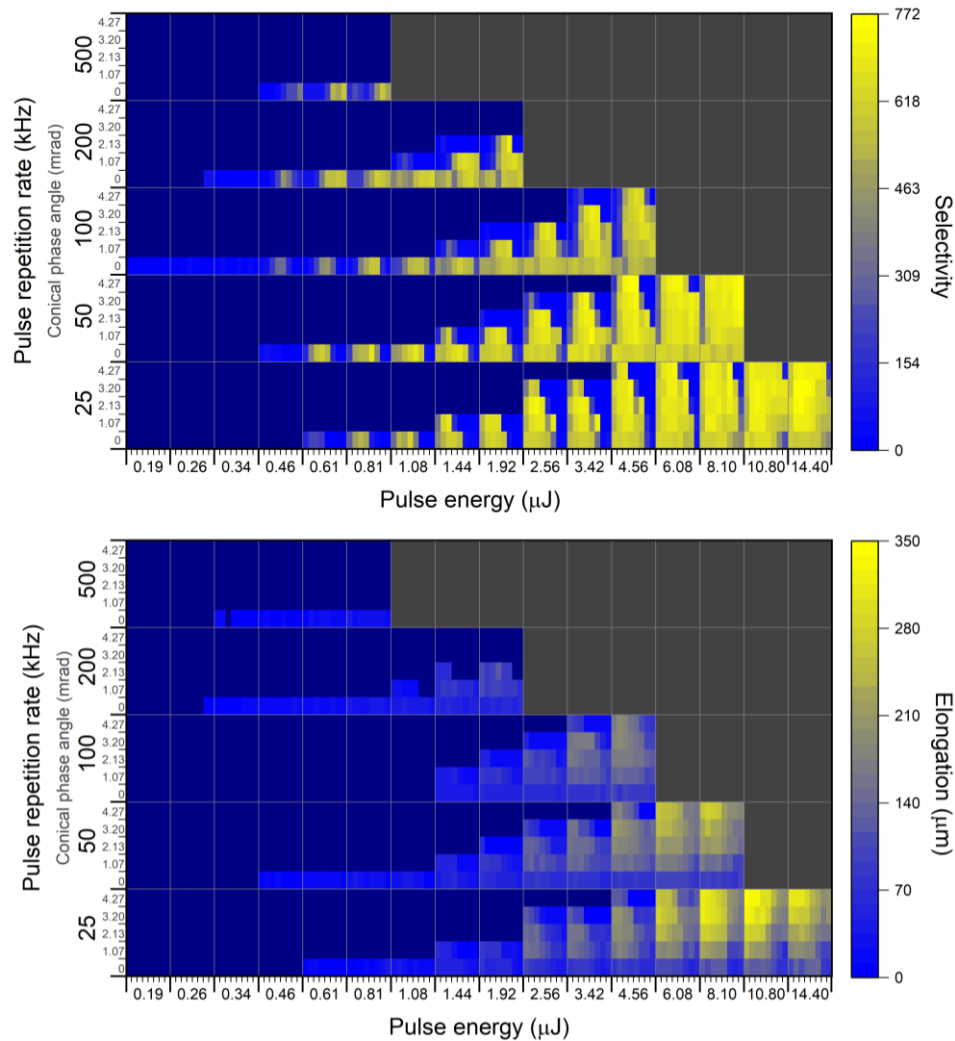


Fig. 5: Heat maps displaying the results of the final parameter space investigation. The selectivity (top) and DOF (bottom) were measured for channels written with several pulse energies, writing speeds, conical phase base-angles and pulse repetition rates. The minor tick marks along the pulse energy axis represent doubling sample translation speeds from 1 to 128 mm/s, while the minor tick marks along the repetition rate axis denote base-angles from 0 to 4.27 mrad. Circularly polarised light was used throughout. The uncertainty in the selectivity is approximately 5.2%.

An alternative representation of the data provided by the heatmap in Fig. 5 can be found in Supplement 1. Here, the data is offered in terms of the number of overlapped pulses and the net fluence for each pulse energy investigated. It is common to consider pulse repetition rates below 1 MHz to be thermally non-cumulative; therefore, one may expect the repetition rate and translation speed to be inherently correlated, with the material modification influenced by the pulse overlap alone. We observed this to be the case in general, however, we note a trend for the modification threshold to be more readily reached with higher repetition rates for a given pulse energy and pulse overlap. We also observe a stark reduction in selectivity when writing with many overlapped pulses (approximately >50). We suggest that this may in fact be due to thermal accumulation leading to the

spontaneous annealing of the material defects that drive selective etching. The observation of thermal accumulation at repetition rates $< 1\text{MHz}$ [39], and even as low as 1kHz [40], supports this. As expected, the threshold for modification in terms of net fluence increases with applied conical phase. Generally, once the threshold is reached, the selectivity achieved is consistently around 700, regardless of the degree of elongation.

In terms of the focus elongation, we observed the DOF to increase with conical phase as expected. We further observed the degree of elongation to increase with the number of overlapped pulses for a given pulse energy. At lower pulse energies, the elongation achieved by applying steeper conical phase decreased, and was eventually surpassed by that achieved with shallower conical phase applied. This is likely due to the pulse energy distributed at the extremities of the focal region dropping below the modification threshold.

3.2 Demonstration of glass dicing

To demonstrate the benefit of controllable DOF during inscription, we compared the time taken to inscribe simple geometric shapes, namely an ellipse, star, circle and triangle, into fused silica, both with and without beam elongation. The components were chosen as they demonstrate highly selective polarisation insensitive etching, rapid laser inscription via beam elongation, and are not manufacturable using traditional methods. Firstly, we determined the maximum raster scan layer spacing that resulted in sufficient overlap of the modified regions to facilitate highly selective chemical etching across layers. Surfaces were written through 2 mm thick fused silica substrates with a length of 2 mm and a variable raster spacing. Both Gaussian and vortex (generated with a 4.27mrad conical phase front) foci were used for comparison. For both beam types, the pulse duration was 1440fs and the repetition rate was 50kHz . The pulse energy was 1620 nJ for the Gaussian focus, and 8100 nJ for vortex focus. For the Gaussian focus, the raster spacing was initially set to $2\text{ }\mu\text{m}$ and gradually increased to $20\text{ }\mu\text{m}$ in steps of $2\text{ }\mu\text{m}$ and for the vortex focus, the raster spacing was varied between 100 and $450\text{ }\mu\text{m}$ in steps of $50\text{ }\mu\text{m}$.

The substrates were then etched in 8M KOH at 85°C for 2 hours to allow the etchant to penetrate through the inscribed material. Afterwards, brightfield micrographs were taken of the etched surfaces to clearly identify the surfaces with overlapped modification regions through the substrate, as shown in Fig. 6 (a) and (b). We found that a spacing greater than $16\text{ }\mu\text{m}$ resulted in disconnected channels that prevented etching through the sample when writing with a regular diffraction limited Gaussian focus. Conversely, by using a vortex focus, we observed continuous modification of the glass and subsequent highly selective etching at a layer spacing of up to $200\text{ }\mu\text{m}$. We note that the theoretical confocal parameter of the Gaussian beam waist when focused with an NA of 0.6 in fused silica is $4.4\text{ }\mu\text{m}$ (for a beam quality, M , of 1.2), less than the $16\text{ }\mu\text{m}$ scan spacing that resulted in continuous modification. This observation may be attributed to spherical aberration-induced focus elongation within the substrate [41], self-focusing, or simply because the modification threshold energy extended beyond the confocal parameter in this case.

With the maximum beam elongation established, geometric shapes were laser written in fused silica substrates, measuring $10 \times 10 \times 1\text{ mm}$, and etched in KOH for 2 hours. The full thickness of the substrate was modified layer by layer, with each layer separated by 16 and $200\text{ }\mu\text{m}$ when using a Gaussian and vortex beam respectively. The inscribed substrates and post-etch shapes are presented in Fig. 6 (c) and (d) respectively. With a writing speed of 4 mm/s , the total inscription time was approximately 15 minutes when using the Gaussian focus, and just 72 seconds when using the vortex focus.

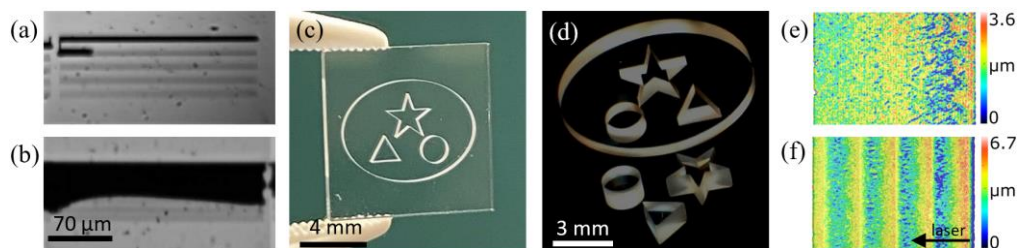


Fig. 6: (a) and (b) show chemically etched tracks written with a vortex beam to determine the maximum z-spacing for continuous modification through silica glass. The surfaces were formed by raster scanning 2 mm long tracks in 2 mm thick glass. Note the micrographs were taken with the surfaces tilted. (c) shows a star, triangle and circle within an ellipse, each inscribed into a 1 mm thick fused silica substrate. The separated components, written with a vortex beam in 72 s , and subsequently etched for two hours, are shown in (d). (e) and (f) are surface profiles of the 1 mm thick etched surfaces inscribed with a Gaussian and vortex focus respectively.

The 12-fold reduction in inscription time highlights the potential for ultrafast-laser-induced selective etching to be used for industry level manufacturing tasks. The two-hour etching time is compatible with rapid prototyping and, as a serial process, does not present a barrier for large scale manufacturing.

The surface quality of laser fabricated components may also be of interest for certain applications, such as when manufacturing micro-optics and microfluidic devices. The form of etched surfaces written with a Gaussian focus and a vortex focus (with the irradiation parameters stated above) through 1 mm thick fused silica was measured by focal-variation microscopy (S neox, Sensofar), and the corresponding surface plots are presented in

Fig. 6 (e) and (f). The roughness measured was significant in both cases: the arithmetic mean roughness (ISO 25178) was 336 nm and 460 nm for Gaussian- and vortex-written surfaces respectively. It is evident from the depth dependence of the surface texturing when writing with a Gaussian beam (Fig. 6 (e)) that laser damage was at least partly responsible for the roughness; unsurprisingly, given the relatively high pulse energy (1620 nJ) used. Perhaps more significant is the clear appearance of laser-scan layers when writing with the vortex beam (Fig. 6 (f)). The layers are formed with the same period as the layer spacing, 200 μm in this case, and are indicative of a non-uniform energy distribution over the DOF. In this instance, the peak-valley variation on the surface between adjacent layers was approximately 6 μm .

It is worth noting that lower roughness has been achieved by writing with a diffraction limited focus and lower pulse energy, particularly in the nanograting regime [5, 42]. For surfaces requiring a smooth finish, writing with less energy and a smaller layer separation, at the expense of longer writing times, may be beneficial.

4. Discussion

Over the past two decades, ultrafast-laser-induced selective etching has been refined to the point where it may now be seriously considered for industry-level manufacturing; aided by the development of robust and less-expensive femtosecond laser systems. Advanced techniques, such as beam shaping, continue to improve the efficiency of laser energy deposition during writing, leading to significant reductions in laser processing times. Adaptive optics offers unparalleled control of the beam intensity profile; facilitating near arbitrary spatial control of the focal volume in real-time, generally without the need to alter the position or alignment of physical optics in the beam delivery path. A significant exception to this occurs when generating a Bessel beam using a diffractive axicon via an SLM, since the Bessel beam forms in the near-field of the axicon rather than in the laser processing plane.

In this work, we have used SLM-generated conical phase fronts, analogous to small-angle diffractive axicon lenses, to generate a high aspect-ratio laser focus extending to the focal plane and demonstrated that the degree of elongation can be controlled simply by increasing the base-angle of the conical phase front. We applied this technique to ultrafast-laser-induced selective etching of fused silica and found irradiation parameters for which the etching-rate enhanced region formed by a single-pass of the laser focus can be elongated by 12.5 times that inscribed with a Gaussian focus. Crucially, the etching selectivity remains high (approximately 800 - 1000) and polarization insensitive for the optimum parameters found. These findings are beneficial in both research and industrial settings: the significant reduction in laser writing time resulting from the elongated modification volume further enhances the rapid-prototyping appeal of laser-assisted etching and enables the fabrication of larger components and quantities which would otherwise be impractical. Further, circumventing the need for strict feature-dependent polarisation alignment while writing greatly reduces the complexity of the laser inscription and hardware control systems.

Interesting trends were observed from the parameter investigation: For a given pulse energy, the elongation of the DOF increased with the number of overlapped pulses, particularly when a conical phase was applied, as long as the pulse energy threshold requirement was met. A consistently high selectivity was achieved for the full range of conical phase amplitudes investigated when sufficient pulse energy was used. However, the selectivity also displayed a characteristic drop-off for each pulse energy investigated when the number of overlapped pulses was high. This suggests that there is a point at which additional laser pulses undo the modification that facilitates increased etching rates. Since circular polarisation was used throughout this study, we expect that the enhanced etching rate was not driven by the formation of directional nanogratings, but rather the formation of molecular defects, nanopores and nanocracks within the laser affected zone. Therefore, we propose that when sufficient pulse overlap is reached, thermal accumulation locally anneals the laser affected zone leading to the drop in etching rate.

One may expect the spatial resolution when writing with a vortex beam to decrease compared to writing with a Gaussian beam. However, we found that this is not generally the case, and that high aspect-ratio channels can be formed irrespective of the conical phase applied. Writing with a vortex beam does affect the surface quality, however, and therefore, this approach is best suited to fabricating large structural surfaces in dramatically reduced laser inscription times, and less suited to forming surfaces in which high surface quality is needed, for example forming optical flats.

The vortex focus offers a key advantage compared to a more typical GB focus, in that the optical path is compatible with several adaptive-optics-enabled beam-shaping applications without any necessary mechanical changes during laser writing, for example, aberration correction [43], adaptive slit shaping [44], multispot writing [44] and accelerating beam writing [46,47]. This implementation facilitates the fabrication of complex components consisting of a variety of surface types and features such as intricate elements requiring high resolution, deep surfaces, and large planes. The reduction in inscription time by 12-fold highlights the potential for industrial level glass cutting, drilling and shaping.

Challenges remain in terms of the power handling capabilities of LCOS-SLM's, however, recent progress in thermal management promises significant improvement in SLM performance at high powers [48].

5. Conclusions

In this paper, we have demonstrated a method of varying laser focus DOF using an SLM for applications in direct laser writing and selective chemical etching. By introducing a conical phase delay to the laser beam via an SLM, a vortex beam was formed at the focal plane after propagation through a 4-f lens relay and objective lens, forming an elongated high-intensity focal region permitting high-aspect ratio glass modification of up to 350 μm along the optical axis. Meanwhile, the chemical etching selectivity of the laser irradiated material remained high, above 1000 in some cases, as confirmed by comprehensive parameter-space investigations. Further, laser inscription was performed with circularly polarized light, demonstrating that the need for maintaining strict polarization alignment to achieve highly selective etching can be overcome. To demonstrate the benefit of elongating the DOF for glass microfabrication applications, a selection of fused silica geometric shapes were fabricated by ultrafast laser induced selective chemical etching with writing time reduced by 12-fold when compared to writing with a more typical Gaussian focus.

Funding. Engineering and Physical Sciences Research Council (EP/P027415/1, EP/S000410/1, EP/T020903/1) and the European Commission (Grant No. 820365). Renishaw for co-funding SRM's EPSRC iCASE PhD studentship.

Acknowledgments. We thank Light Conversion for their support.

Disclosures. The authors declare no conflicts of interest.

Data availability. Data underlying the results presented in this paper are available in Ref. [49].

Supplemental document. See Supplement 1 for supporting content.

References

1. D. Choudhury, J. R. Macdonald, and A. K. Kar, "Ultrafast laser inscription: Perspectives on future integrated applications," *Laser Photonics Rev.* **8**, 827–846 (2014).
2. K. Sugioka and Y. Cheng, "Femtosecond laser three-dimensional micro-and nanofabrication," *Appl. Phys. Rev. J. Laser Appl.* **1**, 41303–42006 (2014).
3. M. Malinauskas, A. Žukauskas, S. Hasegawa, Y. Hayasaki, V. Mizeikis, R. Buividas, and S. Juodkakis, "Ultrafast laser processing of materials: From science to industry," *Light Sci. Appl.* **5**, e16133 (2016).
4. J. Qi, Z. Wang, J. Xu, Z. Lin, X. Li, W. Chu, and Y. Cheng, "Femtosecond laser induced selective etching in fused silica: optimization of the inscription conditions with a high-repetition-rate laser source," *Opt. Express* **26**, 29669 (2018).
5. A. Butkutė, T. Baravykas, J. Stančikas, T. Tičkūnas, R. Vargalis, D. Paipulas, V. Sirutkaitis, and L. Jonušauskas, "Optimization of selective laser etching (SLE) for glass micromechanical structure fabrication," *Opt. Express* **29**, 23487 (2021).
6. Y. Dogan and C. K. Madsen, "Optimization of ultrafast laser parameters for 3D micromachining of fused silica," *Opt. Laser Technol.* **123**, 105933 (2020).
7. M. Hermans, J. Gottmann, and F. Riedel, "Selective, laser-induced etching of fused silica at high scan-speeds using KOH," *J. Laser Micro Nanoeng.* **9**, 126–131 (2014).
8. S. Kim, J. Kim, Y. H. Joung, S. Ahn, J. Choi, and C. Koo, "Optimization of selective laser-induced etching (SLE) for fabrication of 3D glass microfluidic device with multi-layer micro channels," *Micro Nano Syst. Lett.* **7**, 15 (2019).
9. E. Casamenti, S. Pollonghini, and Y. Bellouard, "Few pulses femtosecond laser exposure for high efficiency 3D glass micromachining," *Opt. Express* **29**, 35054 (2021).
10. C. Hnatovsky, R. S. Taylor, E. Simova, V. R. Bhardwaj, D. M. Rayner, and P. B. Corkum, "Polarization-selective etching in femtosecond laser-assisted microfluidic channel fabrication in fused silica," *Opt. Lett.* **30**, 1867 (2005).
11. X. Li, J. Xu, Z. Lin, J. Qi, P. Wang, W. Chu, Z. Fang, Z. Wang, Z. Chai, and Y. Cheng, "Polarization-insensitive space-selective etching in fused silica induced by picosecond laser irradiation," *Appl. Surf. Sci.* **485**, 188–193 (2019).
12. Y. Bellouard, A. Said, M. Dugan, and P. Bado, "Fabrication of high-aspect ratio, micro-fluidic channels and tunnels using femtosecond laser pulses and chemical etching," *Opt. Express* **12**, 2120–2129 (2004).
13. J. Gottmann, M. Hermans, N. Repiev, and J. Ortmann, "Selective laser-induced etching of 3D precision quartz glass components for microfluidic applications-up-scaling of complexity and speed," *Micromachines* **8**, 110 (2017).
14. C. A. Ross, D. G. Maclachlan, D. Choudhury, and R. R. Thomson, "Optimisation of ultrafast laser assisted etching in fused silica," *Opt. Express* **26**, 24343 (2018).
15. S. Kiyama, S. Matsuo, S. Hashimoto, and Y. Morihira, "Examination of etching agent and etching mechanism on femtosecond laser microfabrication of channels inside vitreous silica substrates," *J. Phys. Chem. C* **113**, 11560–11566 (2009).

16. S. Rajesh and Y. Bellouard, "Towards fast femtosecond laser micromachining of fused silica: The effect of deposited energy," *Opt. Express* **18**, 21490 (2010).
17. V. Stankevič, J. Karosas, G. Račiukaitis, and P. Gečys, "Improvement of etching anisotropy in fused silica by double-pulse fabrication," *Micromachines* **11**, 483 (2020).
18. P. S. Salter and M. J. Booth, "Addressable microlens array for parallel laser microfabrication," *Opt. Lett.* **36**, 2302 (2011).
19. M. Zhao, J. Hu, L. Jiang, K. Zhang, P. Liu, and Y. Lu, "Controllable high-throughput high-quality femtosecond laser-enhanced chemical etching by temporal pulse shaping based on electron density control," *Sci. Rep.* **5**, 13202 (2015).
20. B. Sun, P. S. Salter, and M. J. Booth, "Pulse front adaptive optics: a new method for control of ultrashort laser pulses," *Opt. Express* **23**, 19348 (2015).
21. A. Patel, Y. Svirko, C. Durfee, and P. G. Kazansky, "Direct Writing with Tilted-Front Femtosecond Pulses," *Sci. Rep.* **7**, 12928 (2017).
22. B. Sun, P. S. Salter, C. Roider, A. Jesacher, J. Strauss, J. Heberle, M. Schmidt, and M. J. Booth, "Four-dimensional light shaping: Manipulating ultrafast spatiotemporal foci in space and time," *Light Sci. Appl.* **7**, 17117 (2018).
23. R. Kammel, R. Ackermann, J. Thomas, J. Götte, S. Skupin, A. Tunnermann, and S. Nolte, "Enhancing precision in fs-laser material processing by simultaneous spatial and temporal focusing," *Light Sci. Appl.* **3**, e169 (2014).
24. P. S. Salter and M. J. Booth, "Adaptive optics in laser processing," *Light Sci. Appl.* **8**, 2047–7538 (2019).
25. Q. Sun, T. Lee, M. Beresna, and G. Brambilla, "Control of Laser Induced Cumulative Stress for Efficient Processing of Fused Silica," *Sci. Rep.* **10**, 1–8 (2020).
26. M. Mikutis, T. Kudrius, G. Šlekys, D. Paipulas, and S. Juodkazis, "High 90% efficiency Bragg gratings formed in fused silica by femtosecond Gauss-Bessel laser beams," *Opt. Mater. Express* **3**, 1862 (2013).
27. D. A. Yashunin, Y. A. Malkov, L. A. Mochalov, and A. N. Stepanov, "Fabrication of microchannels in fused silica using femtosecond Bessel beams," *J. Appl. Phys.* **118**, 093106 (2015).
28. Z. Wang, L. Jiang, X. Li, A. Wang, Z. Yao, K. Zhang, and Y. Lu, "High-throughput microchannel fabrication in fused silica by temporally shaped femtosecond laser Bessel-beam-assisted chemical etching," *Opt. Lett.* **43**, 98 (2018).
29. R. Meyer, L. Froehly, R. Giust, J. Del Hoyo, L. Furfaro, C. Billet, and F. Courvoisier, "Extremely high-aspect-ratio ultrafast Bessel beam generation and stealth dicing of multi-millimeter thick glass," *Appl. Phys. Lett.* **114**, 201105 (2019).
30. M. Jenne, D. Flamm, K. Chen, M. Schäfer, M. Kumkar, and S. Nolte, "Facilitated glass separation by asymmetric Bessel-like beams," *Opt. Express* **28**, 6552 (2020).
31. M. K. Bhuyan, F. Courvoisier, P.-A. Lacourt, M. Jacquot, L. Furfaro, M. J. Withford, and J. M. Dudley, "High aspect ratio taper-free microchannel fabrication using femtosecond Bessel beams," *Opt. Express* **18**, 566 (2010).
32. Z. Yao, L. Jiang, X. Li, A. Wang, Z. Wang, M. Li, and Y. Lu, "Non-diffraction-length, tunable, Bessel-like beams generation by spatially shaping a femtosecond laser beam for high-aspect-ratio micro-hole drilling," *Opt. Express* **26**, 21960 (2018).
33. R. Bowman, N. Muller, X. Zambrana-Puyalto, O. Jedrkiewicz, P. Di Trapani, and M. J. Padgett, "Efficient generation of Bessel beam arrays by means of an SLM," *Eur. Phys. J. Spec. Top.* **199**, 159–166 (2011).
34. P. Vaity and L. Rusch, "Perfect vortex beam: Fourier transformation of a Bessel beam," *Opt. Lett.* **40**, 597 (2015).
35. E. Alimohammadian, E. Ertorer, E. Mejia Uzeda, J. Li, and P. R. Herman, "Inhibition and enhancement of linear and nonlinear optical effects by conical phase front shaping for femtosecond laser material processing," *Sci. Rep.* **10**, 1–13 (2020).
36. E. Alimohammadian, E. Ertorer, and P. R. Herman, "Conical phase front and aberration beam shaping for manipulating femtosecond laser chemical etching," *Opt. Mater. Express* **11**, 2432 (2021).
37. P. S. Salter and M. J. Booth, "Designing and aligning optical systems incorporating Liquid crystal spatial light modulators (SLMs)," <https://aomicroscopy.org/slm-alignment>.
38. Y. Dai, J. Antonello, and M. J. Booth, "Calibration of a phase-only spatial light modulator for both phase and retardance modulation," *Opt. Express* **27**, 17912 (2019).
39. S. M. Eaton, H. Zhang, M. Li Ng, J. Li, W.-J. Chen, S. Ho, and P. R. Herman, "Transition from thermal diffusion to heat accumulation in high repetition rate femtosecond laser writing of buried optical waveguides," *Opt. Express*, **16**, 9443–9458 (2008).
40. X. Jia and X. Zhao, "Thermal accumulation at kilohertz repetition rates inside fused silica under ultrafast laser irradiation," *Opt. Lett.*, **45**, 3390–3393 (2020).

41. N. Huot, R. Stoian, A. Mermillod-Blondin, C. Mauclair, and E. Audouard, "Analysis of the effects of spherical aberration on ultrafast laser-induced refractive index variation in glass," *Opt. Express* **15**, 12395 (2007).
42. C. Ross, D. G. Maclachlan, D. Choudhury, and R. R. Thomson, "Towards optical quality micro-optic fabrication by direct laser writing and chemical etching," in *Proceedings of SPIE*, 10094, p. 100940V (2017)
43. L. Huang, P. S. Salter, F. Payne, and M. J. Booth, "Aberration correction for direct laser written waveguides in a transverse geometry," *Opt. Express* **24**, 10565 (2016).
44. P. S. Salter, A. Jesacher, J. B. Spring, B. J. Metcalf, N. Thomas-Peter, R. D. Simmonds, N. K. Langford, I. A. Walmsley, and M. J. Booth, "Adaptive slit beam shaping for direct laser written waveguides," *Opt. Lett.* **37**, 470–472 (2012).
45. A. Jesacher and M. J. Booth, "Parallel direct laser writing in three dimensions with spatially dependent aberration correction," *Opt. Express* **18**, 21090 (2010).
46. A. Mathis, F. Courvoisier, L. Froehly, L. Furfaro, M. Jacquot, P. A. Lacourt, and J. M. Dudley, "Micromachining along a curve: Femtosecond laser micromachining of curved profiles in diamond and silicon using accelerating beams," *Appl. Phys. Lett.* **101**, 071110 (2012).
47. D. Sohr, J. U. Thomas, and S. Skupin, "Shaping convex edges in borosilicate glass by single pass perforation with an Airy beam," *Opt. Lett.* **46**, 2529 (2021).
48. G. Zhu, D. Whitehead, W. Perrie, O. J. Allegre, V. Olle, Q. Li, Y. Tang, K. Dawson, Y. Jin, S. P. Edwardson, L. Li, and G. Dearden, "Investigation of the thermal and optical performance of a spatial light modulator with high average power picosecond laser exposure for materials processing applications," *J. Phys. D: Appl. Phys.* **51**, 095603 (2018).
49. S. R. McArthur, R. R. Thomson, and C. A. Ross, "Investigating focus elongation using a spatial light modulator for high-throughput ultrafast-laser-induced selective etching in fused silica: data," Heriot-Watt University, 2022, doi.org/10.17861/60562b62-7fb5-462a-aa9e-90a998135e23

8.2. “Volume Bragg gratings written in fused silica at depth via spatial-light-modulator assisted aberration compensation”

Ultrafast laser inscription of efficient volume Bragg gratings deep in fused silica using active wavefront shaping

S. R. McARTHUR^{1,2}, J. SILIPRANDI¹, D. G. MACLACHLAN¹, A. BENOÎT¹, R. R. THOMSON¹, AND C. A. ROSS^{1,3}

¹Scottish Universities Physics Alliance (SUPA), Institute of Photonics and Quantum Sciences, School of Engineering and Physical Sciences, Heriot-Watt University, Edinburgh, EH14 4AS, UK

²srm37@hw.ac.uk

³calum.ross@hw.ac.uk

Abstract: The maximum depth that photonic structures such as volume Bragg gratings (VBGs) can be precisely fabricated inside dielectric materials using ultrafast laser inscription (ULI) is limited by the aberration imparted on the laser beam by the air-substrate interface as it is focused into the substrate. Here, we use a computer-controlled spatial light modulator (SLM) to shape the wavefront of the ULI laser before it is focused into the substrate, such that the impact of this aberration on the manufacture of VBGs is minimized. We show that this technique allows us to inscribe efficient VBGs at depths in fused silica that would otherwise result in low efficiency VBGs. We find that an optimized “reference” grating fabricated at a mean depth of 200 μm without wavefront shaping exhibited a maximum relative first-order diffraction efficiency of 48%, whereas a grating fabricated at a mean depth of 900 μm using identical parameters exhibited an efficiency of 6.2% – both measured with 633 nm light polarized perpendicularly to the grating lines. Using the SLM to control the wavefront of the ULI laser beam, we were able to pre-compensate for the effect of the substrate surface aberration and fabricate gratings at a mean depth of 900 μm that increased the first-order relative diffraction efficiency to ~42%. A further plasma study provided significant evidence to the effectiveness of Zernike polynomials for spherical aberration correction. Combining both plasma imaging and laser writing approaches, a set of polynomials for aberration correction at a range of depths was produced with scope for arbitrary depth correction.

© 2022 Optica Publishing Group under the terms of the [Optica Publishing Group Open Access Publishing Agreement](#)

1. Introduction

Ultrafast laser inscription (ULI) is an emerging advanced laser manufacturing technique that exploits focused ultrafast laser pulses of sub-bandgap laser radiation to induce localized structural changes inside dielectric materials [17]. Depending on the ULI parameters, the laser induced modification can manifest itself in a variety of ways, examples of which include variation to the refractive index and/or chemical etch rate [18–20]. Using these modifications, three-dimensional (3D) optical components, such as mode-multiplexer, integrated photonic lanterns and volume Bragg gratings (VBGs) can be fabricated [4,15,21–23].

One issue that is commonly encountered when performing ULI is that the maximum depth at which structures can be fabricated inside a substrate is limited by the effect of spherical aberration imparted on the ULI laser beam by the air-substrate interface [1] (we will refer to this aberration as the “substrate aberration”). The substrate aberration distorts the laser focus and resultant material modification. Since the amount of substrate aberration imparted on the laser beam increases as the depth of the focus inside the substrate increases, the laser modification itself becomes a function of depth, even if all other ULI parameters are held constant. This is particularly significant for high-numerical aperture (NA) focusing, where substrate aberration becomes severe even at shallow depths. High-NA inscription is desirable because the resolution of resolvable features increases with NA, according to the Sparrow criterion. Therefore, the substrate aberration limits the fidelity of structures fabricated at depths where aberrations become significant, and in the context of VBG fabrication, potentially limits the VBG thickness and depth at which high quality VBGs can be fabricated. The latter of these could be particularly important for fabricating advanced VBG structures, such as the stacked VBGs that have recently been used for astronomical spectrograph applications [24]. Previously, femtosecond laser written VBGs spanning a depth of 600 μm in fused silica has been demonstrated [5]. We note though that performance variation over the grating depth was not reported.

One solution to address the impact of the substrate aberration is to use a spatial-light-modulator (SLM) to shape the incident laser wavefront via the application of a “phase mask”. SLMs have been used previously to tune the periodicity when writing Bragg gratings with a traditional mask and cylindrical lens [25], and for correcting

for aberrations when writing Bragg gratings in fibers [26]. Here we propose that with an appropriately designed phase mask, the writing beam wavefront can be shaped such that the substrate aberration effects are pre-compensated for [16,27,28] in order to write VGBs deep within a substrate. In this work, we investigated how the surface aberration affects the performance of VGBs fabricated in fused silica and demonstrate the use of a liquid crystal SLM for writing high quality VGBs at depths where substrate aberration would otherwise prevent this. We find that by using the SLM for aberration compensation, we can fabricate optimal gratings at a mean depth of 900 μm that exhibit a first-order relative diffraction efficiency of 42% for linearly polarized 633 nm light, close to the range of the 48% measured for optimal VGBs fabricated near the substrate surface without aberration correction.

2. Experimental methods

2.1 The ultrafast laser inscription system

Figure 1 is a schematic of the ULI system used in this work, which incorporates an SLM for surface aberration compensation. The fabrication laser used was a diode-pumped ytterbium-doped bulk laser system (*Pharos*, Light Conversion) with a 1030 nm central wavelength, allowing tuneable pulse duration and repetition rate. The components following the laser include a power control system directly at the output of the laser consisting of a half-wave plate (HWP) and polarizing beam splitter (PBS). The linearly polarized laser beam was expanded using lenses L1 (plano-concave, $f = -25$ mm, LC1054-B Thorlabs) and L2 (plano-convex, $f = 75$ mm, LA1608-B Thorlabs) to overfill the active area of the SLM, increasing the beam diameter from 4.5 mm to 13.2 mm ($1/e^2$). The phase-only reflective liquid-crystal-on-silicon (LCOS) SLM (X13138, Hamamatsu) had an active area consisting of 1272×1024 pixels with a pixel pitch of 12.5 μm , each providing a $0 - 2\pi$ phase modulation at 1030 nm by applying an 8-bit value from 0 - 150, giving a pixel phase resolution of ~ 0.042 radians. To enable shaping of the laser beams amplitude profile, a blazed grating was applied to the SLM to direct $\sim 80\%$ of the incident power into the positive first diffraction order. A 4f imaging system was used to image the SLM onto the back aperture of the objective lens (OBJ1) which then focused the laser beam into the substrate. The first Fourier transform lens (F_{T1}) had a focal length of 1000 mm (bi-convex, LB1859-B Thorlabs) whereas the second (F_{T2}) had a focal length of 400 mm (bi-convex, LB1391-B Thorlabs). An iris (LCP50S, Thorlabs) placed at the focus of F_{T1} was used to block all but the positive first diffraction order. The polarization of the laser reaching the substrate was controlled using a quarter-wave plate (QWP) and second HWP placed before OBJ1. The choice of writing objective (OBJ1) has a significant effect on the available dimensions of the modified volume and depth achievable within the selected sample. The selected objective lens had an effective focal length of 4 mm, an NA of 0.67, and a 10 mm working distance (PAL-50-NIR-HR-LC00, OptoSigma). For this work, we underfilled the objective to achieve an effective writing NA of 0.6, producing a focal volume with theoretical diffraction limited dimensions of 1.0 μm in the transverse plane and 8.3 μm in the axial plane. The substrate was mounted on computer controlled 3-axis air-bearing translation stages (ABL1000, Aerotech) that allowed the sample to be translated through the ULI laser focus with sub-micron precision and with a maximum travel of 100 mm by 100 mm by 25 mm along the x-, y-, and z-axis respectively. Two imaging systems, labeled C1 and C2 (both DCC2545M-GL, Thorlabs), were used for on-axis imaging of the substrate and side-view imaging of the free-electron plasma respectively.

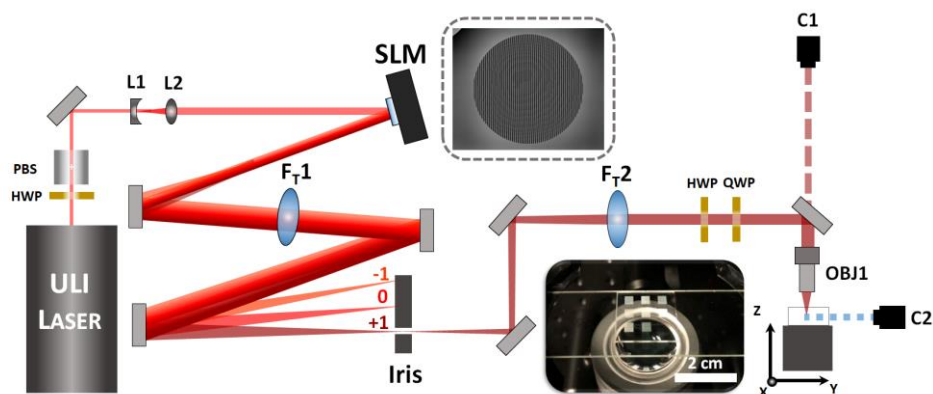


Fig. 1. Schematic diagram of the ULI system. An ultrafast laser system (*Pharos*, Light Conversion) delivered pulses with a 1030 nm wavelength, 200 kHz pulse repetition frequency and 185 fs pulse duration. The laser power reaching the substrate was controlled using a half-waveplate (HWP) and polarizing beam splitter (PBS) placed directly after the laser aperture. Lenses L1 and L2 form a telescope that expands the laser beam to fill the active area of the SLM. The SLM, pictured with an example Zernike polynomial phase mask (inset next to the SLM), was followed by a 4f spatial filtering image relay system, constructed from F_{T1} , F_{T2} , and an iris to block all but one of the orders. The polarization of the laser beam on the substrate was controlled by a second HWP and a quarter-wave plate (QWP) placed before the final writing objective (OBJ1, $\times 50$, 0.67 NA, OptoSigma). The substrate was mounted on a 3-axis air bearing translation stage (Aerotech). C1 and

C2 are digital cameras used to monitor the positioning of the sample (C1) and to image the emission from the free electron plasma (C2). The inset below F_{T2} shows the substrate mounted in front of OBJ1, with a two-dimensional array of VBGs inscribed.

2.2 VBG Characterization system

VBGs are periodic refractive index structures which reflect or diffract light with a highly wavelength and angle dependent efficiency. The behavior of VBGs can be described by coupled wave theory as set out in Refs. [2] and [7]. The performance of our laser fabricated gratings was characterized using the characterization system presented in Figure 2(a). The diffraction efficiency of the VBG under test was determined using both a linearly polarized 633 nm HeNe laser (1125P, Uniphase), and across a broader range of wavelengths using an NKT Photonics SuperK supercontinuum (SC) broadband light source. In combination with a set of bandpass filters (10 nm bandwidth at the full-width half-maximum), the SC was used to study central wavelengths from 500 to 1100 nm in steps of 100 nm. A HWP was used to control the HeNe polarization, while the SC polarization was adjusted using a linear polarizer. The substrates containing the VBGs were mounted on a linear translation stage which enabled transitioning the VBGs between the HeNe (red arrows) and SC (white arrows) beams, Fig. 2(a). The VBGs were also held in a rotation mount that allowed the gratings to be orientated through a range of incident angles (α in Fig. 2(b)) to find the maximum diffraction efficiency of each grating for a given wavelength - in effect applying a blaze to the VBG. This is because the efficiency for a given wavelength is highly angle dependent [29]. The average optical power contained within the positive first-order was measured using an integrating sphere (S142C, Thorlabs), which reduced the possibility of an alignment error on the detector end. Once the diffraction power was maximized by varying the angle, the transmission through pristine (unmodified) material was measured for the same angle as a “zero-diffraction reference”. For our purposes, the diffraction efficiency of any VBG was defined as the optical power measured in the positive first-order relative to the zero-diffraction reference, referred to herein as the “relative diffraction efficiency”. The diffraction efficiencies were measured for two linear polarization states: perpendicular to the modified tracks of the grating, designated p-polarization, and parallel to the modified grating lines, designated s-polarization, as depicted in Figure 2(b). These designations were chosen to adhere to convention, where s- and p-polarization are defined relative to the plane of incidence; which in our case, lay orthogonally to the grating lines.

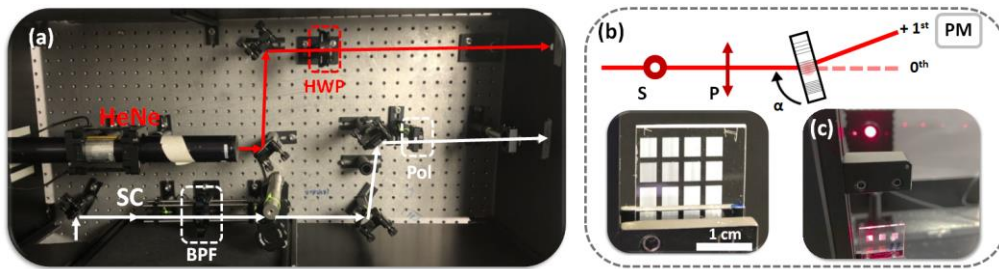


Fig. 2. (a) Annotated digital photograph of the set-up used for characterizing the VBGs, showing the HeNe beam path with the red arrows, and the SC beam path with the white arrows. A half-wave plate (HWP) and polarizer (Pol) were used to control the linear polarization orientation of the HeNe and SC respectively, and a set of bandpass filters (BPF) (FKB-VIS-10, Thorlabs) within a rotating wheel mount was used to filter the SC wavelength. (b) Schematic of the grating showing the grating rotation axis, the positive first and the zeroth orders and the position of the power meter used to measure the positive first-order. Also detailed are the two polarization orientations relative to the sample, labelled P (p-polarization) and S (s-polarization). This is pictured with a scaled photo of a VBG array in the mount. (c) Digital photograph of the mounted sample in the foreground, and the integrating sphere with a 633 nm diffraction pattern in the background. The grating under test was written with a pulse energy of 225 nJ at a depth of 200 μm with the Z(0) phase mask on the SLM. We note the cloudiness of the VBG suggests some degree of glass modification beyond Type I [14].

3. Results

3.1 Developing efficient shallow-depth VBGs

The starting point for the depth correction study was to find ULI parameters that produced an efficient VBG at a mean depth of 200 μm in the substrate, a depth where substrate aberrations are not expected to be significant. While highly efficient VBGs have been produced using ULI, it is important to highlight that this was not the primary aim of this work [15]. Here, we required a grating with sufficiently high relative diffraction efficiency to investigate the evolution of the laser writing capabilities as a function of depth. For all ULI fabrication, the laser pulse repetition rate was set to 200 kHz, the pulse duration to 185 fs, the polarisation was circular, and the substrate translation speed was 4 $\text{mm}\cdot\text{s}^{-1}$. The substrate used for this study was 1 mm thick fused silica (7980 0F grade, Corning). Each VBG layer was fabricated by translating the substrate through the ULI laser focus to inscribe a series of parallel lines of index modification separated by 6 μm . Each line was written along the same direction to ensure consistent modification of the material. The thickness of the VBG was determined by stacking multiple layers spaced by 2.26 μm . It was previously demonstrated that VBGs with a thickness of around 100 μm exhibit high absolute diffraction efficiency for 633 nm light [12]. Therefore, this was chosen as the target thickness,

composed of 45 individual layers of index modification. The transverse dimensions of the VBG were 3 mm by 3.5 mm, chosen such that the interrogation source underfilled the grating area.

VBGs were fabricated using a range of pulse energies from 150 nJ to 250 nJ in steps of 25 nJ. Figure 3(a) depicts the diffraction efficiencies measured for the 45-layer VBGs as a function of the writing pulse energy. The VBG fabricated using 225 nJ pulses exhibited the optimum diffraction efficiency of 48% for p-polarized, and 44% for the s-polarized 633 nm light. Figure 3(b) presents the diffraction efficiency of this VBG as a function of wavelength, indicating that efficiencies of > 40% across the 600 nm to 900 nm spectral band were obtained. This set of ULI parameters, (225 nJ pulses and 45 layers) written at a mean depth of 200 μm below the sample surface, produced a grating with sufficiently high diffraction efficiency to serve as a “reference”. The reference was used to assess the success of the aberration compensation for gratings written deeper within the substrates.

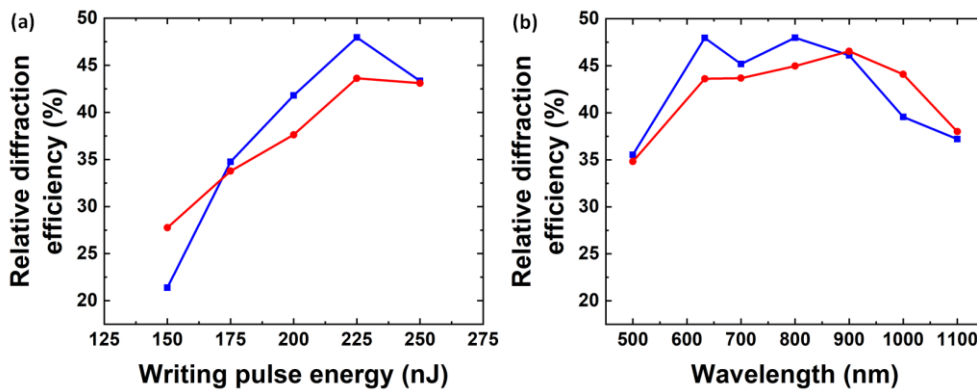


Fig. 3. Measured diffraction efficiencies for p- (square markers, blue line) and s- (circle markers, red line) polarized light. (a) First-order diffraction efficiencies for VBGs fabricated using a range of pulse energies. It is observed that diffraction efficiencies >40% are realized using a pulse energy of 225 nJ. Here, the diffraction efficiency was measured using a HeNe laser at 633 nm. (b) Measured diffraction efficiency vs wavelength for the VBG fabricated with 225 nJ pulses, showing that diffraction efficiencies above 40% relative diffraction efficiency could be obtained for wavelengths between ~600 nm and ~1000 nm.

3.2 Developing efficient VBGs deep in fused silica

With appropriate laser writing parameters established to fabricate efficient VBGs at a depth of 200 μm , the capacity to write efficient VBGs at significantly larger depths in fused silica was investigated. The predominant substrate aberration is expected to be spherical aberration, originating from the air-glass interface as the laser is focused into the sample. A commonly used model for representing optical aberrations is the Zernike polynomials – a set of orthogonal polynomials which can describe any surface deviation on a unit disk [10]. Zernike polynomial, ZP_4^0 , specifically represents primary spherical aberration, and was therefore used to compensate for surface aberration in this work. This phase mask was modulated by the Zernike expansion coefficient, or aberration coefficient, X , which is equal to the peak wavefront error in radians [12]. In the following, we represent an SLM phase profile that consists of a ZP_4^0 polynomial with an aberration coefficient, X , as $Z(X)$. A phase profile denoted $Z(0)$ therefore represents no spherical aberration compensation, and the challenge is to find the value of $Z(X)$ for a given depth which compensates for the effect of the substrate aberration on the laser focus.

VBGs were fabricated using the ULI parameters identified in Section 3.1, at a mean depth of 900 μm . Each grating was written with a different aberration coefficient applied to the phase mask displayed on the SLM, with the magnitude ranging from $Z(-3)$ to $Z(-5)$ in steps of 0.5, and also with a mask of magnitude $Z(0)$ representing a non-aberration compensated grating. The negative sign of the Zernike aberration coefficients simply derives from the phase *delay* introduced to the beam by the SLM when applying positive mask values. The relative diffraction efficiencies were measured with 633 nm light for both s and p polarization states. The relative diffraction efficiencies gave an indication of the extent of aberration compensation provided by the phase mask. The mask which produced a grating with an efficiency close to the reference seen in Fig. 3(a) was presumed to fully compensate for spherical aberration at the associated depth. Figure 4(a) presents VBG diffraction efficiency as a function of the magnitude of $Z(X)$.

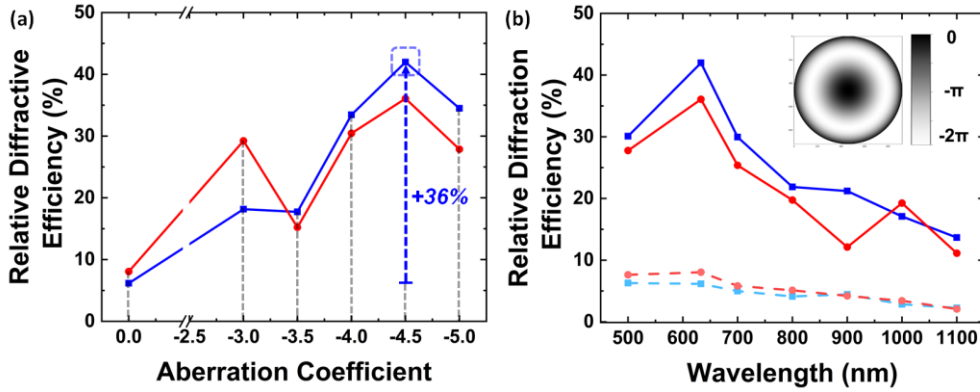


Fig. 4. (a) Relative diffraction efficiency versus aberration coefficient for a set of VBGs written at mean depth of $900\ \mu\text{m}$ for a range of SLM profiles ranging from $Z(0)$ to $Z(-5)$, measured with both p - (square markers, blue line) and s - (circle markers, red line) interrogation beam polarizations. A blue dashed arrow highlights the best performance improvement when using the $Z(-4.5)$ aberration coefficient mask. (b) Relative diffraction efficiency versus wavelength for a VBG written at a mean depth of $900\ \mu\text{m}$, for corrected (solid curves) and uncorrected (dashed dot curves), for both p - (square blue) and s - (circle red) polarizations. Inset: the Zernike polynomial component of the mask projected onto the SLM, for $Z(-4.5)$ in grey scale from 0 to 2π .

This peak efficiency is represented by the dashed blue arrow at $Z(-4.5)$, highlighting an improvement from 6% to 42%, and 8% to 36% for p -polarized and s -polarized 633 nm light respectively. We note that the diffraction efficiency for the $Z(-3.5)$ phase mask deviated from the expected efficiency trend, as affirmed by a repeated fabrication run. Although peculiar, this anomaly was not deemed significant to warrant further exploration within the scope of this work. Figure 4(b) presents first order diffraction efficiency results obtained as a function of wavelength for the best performing grating in Fig. 4(a). The diffraction efficiency for the $Z(0)$ grating is represented by the dash-dot curve, while the $Z(-4.5)$ grating is represented by the solid curve and the light polarizations are colored as before. The aberration correction resulted in a higher relative diffraction efficiency across all wavelengths tested, however they are found to be below the efficiencies detailed in Fig. 3(b). It is clear though that the diffraction efficiency at 633 nm is significantly improved from 6% to 42% by implementing the SLM-based aberration compensation. The inset in Fig. 4(b) shows the Zernike polynomial component of mask $Z(-4.5)$ which was applied to the SLM.

The bandwidth of VBGs, for a given angle of incidence, is predicted by coupled wave theory [2]. To compare the performance of the laser inscribed VBGs to that predicted by theory, the bandwidths of two VBGs were measured: the reference grating at $200\ \mu\text{m}$ and the best performing grating written at $900\ \mu\text{m}$, written with the -4.5 Zernike coefficient. The gratings were interrogated with the SC broadband source and colored filters, at a fixed angle (the optimum found for 633 nm light).

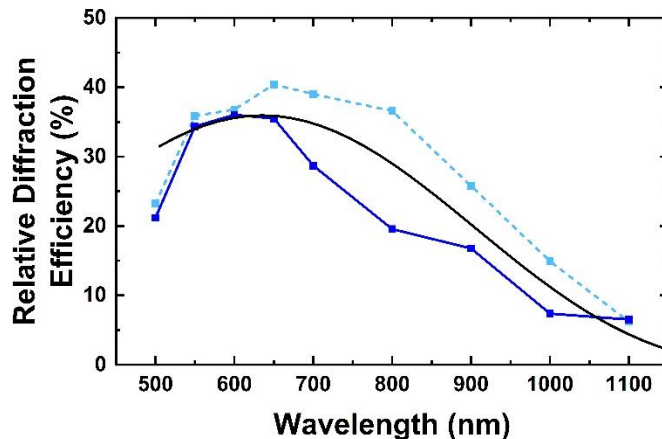


Fig. 5. Plot of relative diffraction efficiency versus wavelength for the reference grating (dashed line, light blue), and corrected VBG written at a mean depth of $900\ \mu\text{m}$ (Solid line, dark blue). The theoretical efficiency predicted by coupled wave theory [2] is also included (black line).

The resultant bandwidths are presented in Figure 5. This study showed that for both VBGs, the efficiency peaks at 633 nm wavelength, in agreement with theory. The spectral profile of the individual gratings differ slightly. The model predicts grating performance for an ideal sinusoidal index profile. In practice, the index profile induced by laser writing is more step like. Further, we expect the index morphology to vary over each grating thickness, such that the effective period of the grating is less well-defined. We also expect scattering to affect the

performance of each grating with a wavelength and angle dependence. It is possible that the specific modification at shallow and deep depths in the material, even with aberration correction, would differ, resulting in variability in the scattering behavior. Considering these limitations, it is still possible to estimate the induced refractive index change from the theoretical model. Doing so, we estimate an index contrast of 1.25×10^{-3} and 1.15×10^{-3} for the shallow and deep gratings respectively.

3.3 Free-electron plasma imaging

To provide further insight into the effect that aberration compensation has on the laser fabrication, we performed free-electron plasma emission imaging experiments, with the aim of correlating the plasma emission properties with VBG diffraction efficiency trends depicted in Fig. 4(a). As proposed by Jesacher et al., the emission of the free electron plasma can provide a useful metric to determine the optimum SLM profile for aberration compensation [16]. As shown in Fig. 1, a camera (DCC2545M-GL, Thorlabs) with a $6.5\times$ magnification zoom lens (MV6X12Z, Thorlabs) and a $0.67\times$ extension lens (MVL067A, Thorlabs) (C2, Fig. 1) was used to record images of the emission from the free electron plasma. A shortpass filter with a cut-off wavelength at $1\ \mu\text{m}$ (FESH1000, Thorlabs) was used to block the $1030\ \text{nm}$ laser light scattered from the focus, ensuring only light originating from the broadband plasma was measured. The laser parameters were consistent with the VBG writing experiment excluding the pulse energy which was increased from $225\ \text{nJ}$ to $300\ \text{nJ}$ to improve the signal to noise ratio on recorded plasma images.

The study was performed at depths of $200\ \mu\text{m}$ and $900\ \mu\text{m}$, corresponding to the inscription depths of the VBGs. As before, plasma emission at a depth of $200\ \mu\text{m}$ without aberration compensation was used as a reference to compare to writing at depth with compensation. Since the $100\ \mu\text{m}$ thick gratings spanned a depth of 850 to $950\ \mu\text{m}$, plasma emission was investigated at $850\ \mu\text{m}$, $900\ \mu\text{m}$, and $950\ \mu\text{m}$, corresponding to the top, middle, and bottom positions of the grating respectively. The phase masks applied for each of the three depths included $Z(0)$, and the range from $Z(-3)$ to $Z(-7)$ in steps of 1 coefficient magnitude. We observed that the plasma intensity diminished over time when the laser was focused into static material, which we assume is related to the laser induced material modification. Therefore, images were taken immediately upon laser exposure in a pristine region of material to capture the plasma intensity consistently. A 0.5 OD neutral density filter (NE05A, Thorlabs) was used to avoid camera pixel saturation for the brightest plasma generation, namely at $200\ \mu\text{m}$ and at $900\ \mu\text{m}$, with $Z(-3)$ to $Z(-6)$ applied. Five plasma images were recorded for each mask and depth. The five peak pixel values from each plasma image were averaged, and then the average value normalized to the average peak pixel intensity of the reference value measured at $200\ \mu\text{m}$. Fig. 6 is a plot of the normalized average peak pixel intensity observed for the range of phase masks, measured when writing at $850 - 950\ \mu\text{m}$ depths (green lines). The measured plasma emission observed at $200\ \mu\text{m}$ without aberration compensation is included for comparison (black datapoint). The error bars represent the minimum and maximum recorded values from the five repeat measurements. The p-polarized diffraction efficiencies (blue square) measured in Fig. 4(a) are also represented for comparison.

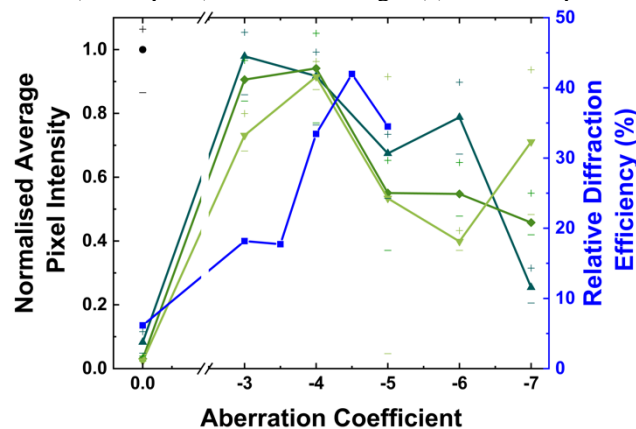


Fig. 6. The normalized average peak pixel intensity recorded when imaging plasma produced with a range of aberration coefficients at shallow and deep depths, namely: $200\ \mu\text{m}$ (shallow reference, black point), $850\ \mu\text{m}$ (dark-green upward triangle), $900\ \mu\text{m}$ (green diamond), and $950\ \mu\text{m}$ (light-green downward triangle). Each point is the normalized average of five measurements and the error bars represent the minimum and maximum measured values. The blue line represents the relative diffraction efficiency of a VBG written at $900\ \mu\text{m}$ (interrogated with horizontally polarized $633\ \text{nm}$ light).

Figure 6 shows that optimally selected Zernike expansion coefficients had a considerable effect on the plasma intensity at a specific depth. For the three depths centered at $900\ \mu\text{m}$ (green shades), the $Z(-4)$ phase mask produced similar and consistent plasma emission, all within the range of the reference point at $200\ \mu\text{m}$ (black point) with an average value of ~ 0.9 . We observed a high peak intensity for $Z(-3)$ for top layers (0.98 at $850\ \mu\text{m}$) but a significant drop in intensity for the deepest grating layer (0.73 at $950\ \mu\text{m}$). The global trend of the plasma

imaging corroborates the previous results with peaks of plasma intensity and relative efficiency between $Z(-4)$ and $Z(-4.5)$. With a long manufacturing time of ~12 hours for each 3 mm by 3.5 mm by 100 μm VBG presented in this work, obtaining aberration compensation parameters by trial and error is impractical. The plasma imaging study is therefore very useful, as it allows approximately optimal aberration correction parameters to be obtained immediately at any depth.

The plasma imaging results provide further insight into depth dependent surface aberration. For gratings spanning greater than 100 μm thickness, it may be beneficial to tune the aberration coefficient dynamically to correct for aberration precisely over the range of depths. The significant writing time per grating attracts system stability issues arising from, for example, fluctuations in the environmental temperature. Fortunately, methods of reducing fabrication times have been reported, including using beam shaping, which are compatible with the aberration correction approach described here [30]. It may also be possible to combine traditional VBG fabrication techniques, such as using physical phase-masks, with SLM controlled aberration correction, or indeed, generate the intensity modulation via the SLM directly. It has been predicted that depth dependent spherical aberration can be compensated for up to a depth of ~6 mm for a 0.6 NA in fused silica using an SLM [28]. These results show that by shaping the wavefront across the beam using an SLM, the quality of the laser spot and plasma intensity at 900 μm depth, and hence the fidelity of laser written VGBs, can be restored close to that seen at a mean depth of 200 μm .

4. Conclusions

The range of substrate depths that ULI can be applied to is conventionally limited by the spherical aberration imparted on the laser beam by the substrate surface – the substrate aberration. This aberration degrades the focal spot as the depth of the focus increases and also limits the resolution of the manufacturing process. To overcome this, an SLM can be used to pre-compensate the phase profile across the laser beam before it enters the lens used to focus the laser light inside the substrate [16,27,28]. In this work, a preliminary investigation was performed to acquire optimal ULI parameters to produce a “reference” VBG at a depth of 200 μm without aberration correction. This reference grating exhibited a relative diffraction efficiency of 48% for p-polarization at 633 nm. A set of VBGs were then fabricated at a depth of 900 μm using SLM profiles with different Zernike expansion coefficients. The relative diffraction efficiencies of VBGs fabricated at a mean depth of 900 μm were found to increase from 6% and 8% for p- and s- polarizations respectively when no aberration compensation is used, to 42% and 36% for p- and s- polarizations respectively when a $Z(-4.5)$ Zernike expansion coefficient was used. These values are close to the diffraction efficiencies measured for the reference grating written at 200 μm without aberration compensation, strongly indicating that the SLM has successfully compensated for the majority of the substrate aberration. A further VBG characterization study using light across a wide spectral region showed that although the aberration corrected VBG maintained the diffraction efficiency at the designed working wavelength of 633 nm, the diffraction efficiency at other wavelengths did not match the values exhibited by the reference grating. This clearly indicates that the VBG fabricated at a depth of 900 μm with optimized aberration compensation does not fully replicate the optical properties of the reference grating, and further studies are required to ascertain why this is the case. A plasma imaging study was also performed that revealed that the intensity of the emission from the free electron plasma at a depth of 900 μm was maximized using an SLM phase profile similar to the phase profile that resulted in optimal VBGs. This suggests that the emission intensity from the free-electron plasma can potentially be used to optimize the VBG fabrication process in other materials, without the requirement for time-consuming parameter scans based on VBG characterization. In summary, this work has demonstrated that with suitable optimization, ULI has the potential to enable the manufacture of complex, high efficiency and extremely robust glass VBGs in dielectric materials for applications ranging from astronomical instrumentation to ultrafast optics.

Funding: This work was funded by the UKRI Engineering and Physical Sciences Research Council (EPSRC) (EP/P027415/1, EP/S000410/1, and EP/T020903/1), the UKRI Science and Technology Facilities Council (STFC) (ST/V000403/1), the European Commission (Grant No. 820365). RRT and SRM thank Renishaw for co-funding SRM’s EPSRC iCASE PhD studentship.

Acknowledgments: We thank Light Conversion for their support.

Disclosure: The authors declare no conflicts of interest.

Data availability. Data underlying the results presented in this paper are available in Ref. [24].

References

1. N. Huot, R. Stoian, A. Mermillod-Blondin, C. Mauclair, and E. Audouard, "Analysis of the effects of spherical aberration on ultrafast laser-induced refractive index variation in glass," *Opt. Express* **15**(19), 12395 (2007).
2. I. V. Ciapurin, "Modeling of phase volume diffractive gratings, part 1: transmitting sinusoidal uniform gratings," *Opt. Eng.* **45**(1), 015802 (2006).
3. S. Y. Haffert, R. J. Harris, A. Zanutta, F. A. Pike, A. Bianco, E. Redaelli, A. Benoît, D. G. MacLachlan, C. A. Ross, I. Gris-Sánchez, M. D. Trappen, Y. Xu, M. Blaicher, P. Maier, G. Riva, B. Sinquin, C. Kulcsár, N. A. Bharmal, E. Gendron, L. Staykov,

- T. J. Morris, S. Barboza, N. Muench, L. Bardou, L. Prengère, H.-F. Raynaud, P. Hottinger, T. Anagnos, J. Osborn, C. Koos, R. R. Thomson, T. A. Birks, I. A. G. Snellen, and C. U. Keller, "Diffraction-limited integral-field spectroscopy for extreme adaptive optics systems with the multicore fiber-fed integral-field unit," *J. Astron. Telesc. Instruments, Syst.* **6**(04), (2020).
4. J. Thomas, C. Voigtländer, R. G. Becker, D. Richter, A. Tünnermann, and S. Nolte, "Femtosecond pulse written fiber gratings: A new avenue to integrated fiber technology," *Laser Photonics Rev.* **6**(6), 709–723 (2012).
 5. C. Voigtländer, D. Richter, J. Thomas, A. Tünnermann, and S. Nolte, "Inscription of high contrast volume Bragg gratings in fused silica with femtosecond laser pulses," *Appl. Phys. A Mater. Sci. Process.* **102**(1), 35–38 (2011).
 6. M. J. Booth, M. A. A. Neil, R. Juskaitis, and T. Wilson, "Adaptive aberration correction in a confocal microscope," *Proc. Natl. Acad. Sci. U. S. A.* **99**(9), 5788 (2002).
 7. S. R. McArthur, J. Siliprandi, D. G. MacLachlan, A. Benoît, R. R. Thomson, and C. A. Ross, "Ultrafast laser inscription of efficient volume Bragg gratings deep in fused silica using active wavefront shaping," *Opt. Mater. Express* **12**(9), 3589 (2022).
 8. K. Fuerschbach, J. P. Rolland, and K. P. Thompson, "Theory of aberration fields for general optical systems with freeform surfaces," *Opt. Express* **22**(22), 26585 (2014).
 9. A. Jesacher and M. J. Booth, "Parallel direct laser writing in three dimensions with spatially dependent aberration correction," *Opt. Express* **18**(20), 21090 (2010).
 10. B. V. N. Mahajan, "Zernike Annular Polynomials and Optical Aberrations of Systems with Annular Pupils," *Appl. Opt.* **33**(34), 8125 (1994).
 11. J.-M. Wang, C.-L. Liu, Y.-N. Luo, Y.-G. Liu, and B.-J. Hu, "Statistical virtual eye model based on wavefront aberration," *Int. J. Ophthalmol.* **5**(5), 620–624 (2012).
 12. V. Lakshminarayanan and A. Flece, "Erratum: Zernike polynomials: A guide (*Journal of Modern Optics* (2011) 58:7 (545-561))," *J. Mod. Opt.* **58**(18), 1678 (2011).
 13. M. Mikutis, T. Kudrius, G. Šlekys, D. Paipulas, and S. Juodkazis, "High 90% efficiency Bragg gratings formed in fused silica by femtosecond Gauss-Bessel laser beams," *Opt. Mater. Express* **3**(11), 1862–1871 (2013).
 14. D. Choudhury, J. R. Macdonald, and A. K. Kar, "Ultrafast laser inscription: Perspectives on future integrated applications," *Laser Photonics Rev.* **8**(6), 827–846 (2014).
 15. M. Mikutis, T. Kudrius, G. Šlekys, D. Paipulas, and S. Juodkazis, "High 90% efficiency Bragg gratings formed in fused silica by femtosecond Gauss-Bessel laser beams," *Opt. Mater. Express* **3**(11), 1862 (2013).
 16. A. Jesacher, G. D. Marshall, T. Wilson, and M. J. Booth, "Adaptive optics for direct laser writing with plasma emission aberration sensing," *Opt. Express* **18**(2), 656 (2010).
 17. K. M. Davis, K. Miura, N. Sugimoto, and K. Hirao, "Writing waveguides in glass with a femtosecond laser," *Opt. Lett.* **21**(21), 1729–1731 (1996).
 18. K. Miura, J. Qiu, H. Inouye, T. Mitsuyu, and K. Hirao, "Photowritten optical waveguides in various glasses with ultrashort pulse laser," *Appl. Phys. Lett.* **71**(23), 3329–3331 (1997).
 19. Y. Bellouard, A. Champion, B. Lenssen, M. Matteucci, A. Schaap, M. Beresna, C. Corbari, M. Gecevičius, P. Kazansky, O. Chappuis, M. Kral, R. Clavel, F. Barrot, J. M. Breguet, Y. Mabilard, S. Bottinelli, M. Hopper, C. Hoenninger, E. Mottay, and J. Lopez, "The femtoprint project," *J. Laser Micro Nanoeng.* **7**(1), 1–10 (2012).
 20. T. Toma, Y. Furuya, W. Watanabe, K. Itoh, J. Nishi, and K. Hayash, "Estimation of the Refractive Index Change in Glass Induced by Femtosecond Laser Pulse," *Opt. Rev.* **7**(1), 14–17 (2000).
 21. S. Gross and M. J. Withford, "Ultrafast-laser-inscribed 3D integrated photonics: Challenges and emerging applications," *Nanophotonics* **4**(1), 332–352 (2015).
 22. R. R. Thomson, T. A. Birks, S. G. Leon-Saval, A. K. Kar, and J. Bland-Hawthorn, "Ultrafast laser inscription of an integrated photonic lantern," *Opt. Express* **19**(6), 5698–5705 (2011).
 23. D. G. MacLachlan, R. R. Thomson, C. R. Cunningham, and D. Lee, "Mid-Infrared Volume Phase Gratings Manufactured using Ultrafast Laser Inscription," *Opt. Mater. Express* **3**(10), 1616 (2013).
 24. S. Y. Haffert, R. J. Harris, A. Zanutta, F. A. Pike, A. Bianco, E. Redaelli, A. Benoît, D. G. MacLachlan, C. A. Ross, I. Gris-Sánchez, M. D. Trappen, Y. Xu, M. Blaicher, P. Maier, G. Riva, B. Sinquin, C. Kulcsár, N. A. Bharmal, E. Gendron, L. Staykov, T. J. Morris, S. Barboza, N. Muench, L. Bardou, L. Prengère, H.-F. Raynaud, P. Hottinger, T. Anagnos, J. Osborn, C. Koos, R. R. Thomson, T. A. Birks, I. A. G. Snellen, and C. U. Keller, "Diffraction-limited integral-field spectroscopy for extreme adaptive optics systems with the Multi-Core fiber-fed Integral-Field Unit," *J. Astron. Telesc. Instruments, Syst.* **6**(04), (2020).
 25. C. Voigtländer, R. G. Krämer, T. A. Goebel, D. Richter, and S. Nolte, "Variable wavefront tuning with a SLM for tailored femtosecond fiber Bragg grating inscription," *Opt. Lett.* **41**(1), 17 (2016).
 26. P. S. Salter, M. J. Woolley, S. M. Morris, M. J. Booth, and J. A. J. Fells, "Femtosecond fiber Bragg grating fabrication with adaptive optics aberration compensation," *Opt. Lett.* **43**(24), 5993 (2018).
 27. R. D. Simmonds, P. S. Salter, A. Jesacher, and M. J. Booth, "Three dimensional laser microfabrication in diamond using a dual adaptive optics system," *Opt. Express* **19**(24), 24122 (2011).
 28. P. S. Salter, M. Baum, I. Alexeev, M. Schmidt, and M. J. Booth, "Exploring the depth range for three-dimensional laser machining with aberration correction," *Opt. Express* **22**(15), 17644 (2014).
 29. S. C. Barden, J. A. Arns, W. S. Colburn, and J. B. Williams, "Volume-Phase Holographic Gratings and the Efficiency of Three Simple Volume-Phase Holographic Gratings," *Publ. Astron. Soc. Pacific* **112**(772), 809–820 (2000).
 30. S. R. McArthur, R. R. Thomson, and C. A. Ross, "Investigating focus elongation using a spatial light modulator for high-throughput ultrafast-laser-induced selective etching in fused silica," *Opt. Express* **30**(11), 18903 (2022).

Internal Examiners Declaration Form
 (This form must be typed and all sections completed)

| | | | |
|---|---------------------|------------------------|-----------|
| Candidate's Name: | Sam Robert McArthur | Heriot-Watt Person ID: | H00129732 |
| School: | EPS | Degree Sought: | PhD |
| Campus: <i>(If off-campus please state location)</i> | Edinburgh | | |

Declaration

- I confirm that the corrections to the thesis of the above named have been carried out to the satisfaction of the examiners Yes No N/A
- I confirm that the Joint Examiners Report Form states recommendation (c) - 'Award degree following satisfactory completion of significant corrections to the satisfaction of the Internal Examiner' Yes No

If yes,


- Please provide details below to demonstrate that the particular corrections are satisfactory.
- Confirm that the corrections have been completed within the period of time given, if not please give an explanation.

I can confirm that Sam has addressed every correction provided to him by the examiners, and has completed these within 3 months of the viva date.

- I confirm that the Joint Examiners Recommendation was originally: Re-submit (decision (d or e) on the previous Joint Examiners Form) Yes No
- I confirm that thesis title has changed since the temporary thesis was submitted. **If yes,** please provide details of amended title here: Yes No

- I confirm that I have seen the final version of this thesis and it has been presented in accordance with University regulations. Yes

Internal Examiner

| | | | |
|-------------|---|---------|-------------------|
| Print Name: | Richard McCracken | Date: | 18 September 2023 |
| Signature: |  | School: | EPS |

Notes

- The Internal Examiner's Declaration Form should be submitted along with the final electronic copy of the thesis through the [Postgraduate Research Thesis Submission site](#)